OKINAWA INSTITUTE OF SCIENCE AND TECHNOLOGY GRADUATE UNIVERSITY
沖縄科学技術大学院大学

Spectral theory of turbulent flows

Author	Dongrong Zhang
Degree Conferral Date	2018-06-30
Degree	Doctor of Philosophy
Degree Referral Number	38005甲第16号
Copyright Information	(C) 2018 The Author
URL	http://doi.org/10.15102/1394.00000368

Okinawa Institute of Science and Technology
Graduate University

Thesis submitted for the degree

Doctor of Philosophy

Spectral theory of turbulent flows

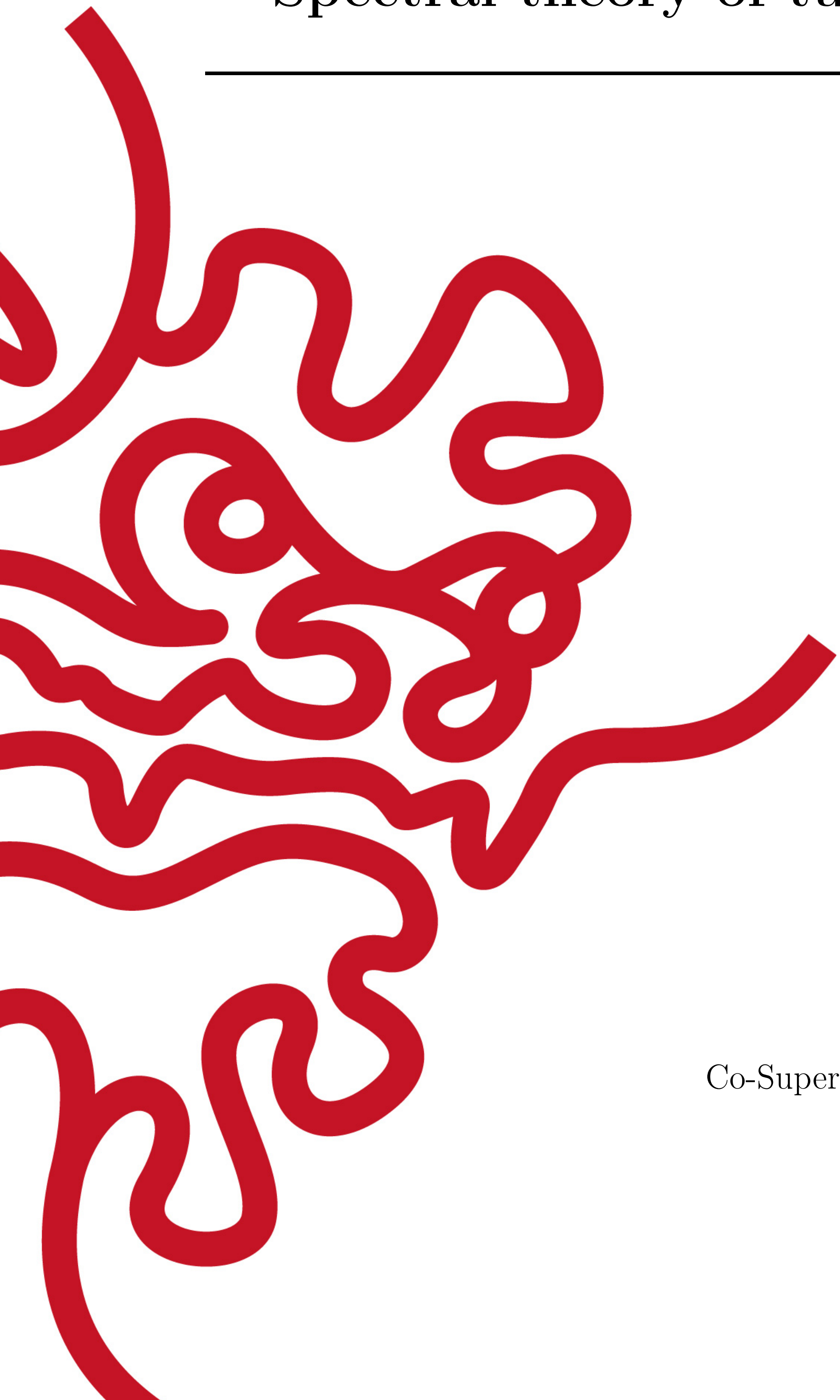

by

Dongrong Zhang

Supervisor: **Gustavo Gioia**
Co-Supervisor: **Pinaki Chakraborty**

June, 2018

Declaration of Original and Sole Authorship

I, Dongrong Zhang, declare that this thesis entitled *Spectral theory of turbulent flows* and the data presented in it are original and my own work.

I confirm that:

- No part of this work has previously been submitted for a degree at this or any other university.
- References to the work of others have been clearly acknowledged. Quotations from the work of others have been clearly indicated, and attributed to them.
- In cases where others have contributed to part of this work, such contribution has been clearly acknowledged and distinguished from my own work.
- None of this work has been previously published elsewhere, with the exception of the following presentations:
    1. Dongrong Zhang, Gustavo Gioia, and Pinaki Chakraborty. Spectral theory of the mean velocity profile in thermally stratified plane-Couette flows. International Conference on Mechanical and Aerospace Systems, Chengdu, China, March 2018.
    2. Dongrong Zhang, Gustavo Gioia, and Pinaki Chakraborty. Spectral theory of the mean velocity profile in thermally stratified plane-Couette flows. 2nd International Conference in Aerospace for Young Scientists, Beijing, China, September 2017.
    3. Dongrong Zhang, Gustavo Gioia, and Pinaki Chakraborty. Spectral theory of the mean-velocity profile in thermally stratified plane-Couette flows. RIMS Workshop on Applied Mathematical and Physical Aspects of Inhomogeneous Turbulence, Kyoto, Japan, July 2017.
    4. Dongrong Zhang, Gustavo Gioia, and Pinaki Chakraborty. Spectral link for the mean velocity profile in the atmospheric boundary layer. Bulletin of the American Physical Society, 69th Annual Meeting of the APS Division of Fluid Dynamics, Volume 61, Number 20, Portland, Oregon, November 2016.
    5. Dongrong Zhang, Gustavo Gioia, and Pinaki Chakraborty. Spectral link for the mean velocity profile in the atmospheric boundary layer. VIIIth

International Symposium on Stratified Flows, San Diego, California, August 2016.

6. Dongrong Zhang, Gustavo Gioia, and Pinaki Chakraborty. Macroscopic non-universality in turbulent plane Couette flows. International Symposium on Near-Wall Flows: Transition and Turbulence, Kyoto, Japan, June 2016.
7. Dongrong Zhang, Gustavo Gioia, and Pinaki Chakraborty. Non-unique frictional drag in turbulent plane Couette flows. Bulletin of the American Physical Society, 68th Annual Meeting of the APS Division of Fluid Dynamics, Volume 60, Number 21, Boston, Massachusetts, November 2015.
8. Dongrong Zhang, Gustavo Gioia, and Pinaki Chakraborty. The spectral link in mean-velocity profile of turbulent plane-Couette flows. Bulletin of the American Physical Society, APS March Meeting 2015, Volume 60, Number 1, San Antonio, Texas, March 2015.

Date: June, 2018
Signature: Dongrong Zhang

Abstract

Spectral theory of turbulent flows

In this doctoral thesis we formulate a spectral theory of the mean-velocity profiles (MVPs) of wall-bounded turbulent flows and use the spectral theory along with dimensional analysis and similarity methods to shed some new theoretical light on several outstanding problems in the interpretation of the extensive empirical data available on such flows. The spectral theory applies to turbulent flows of both constant-density and stratified fluids, and is predicated on the derivation, which we accomplish via a control-volume analysis, of a "spectral link" between the MVPs and the eddy velocity distribution (or, alternatively, the spectrum of turbulent kinetic energy) of the phenomenological theory of turbulence. This spectral link is bijective in that it relates each successive layer of a MVP to, and only to, the corresponding range of the eddy velocity distribution (the buffer layer to the dissipative range, the log layer to the inertial range, and the wake to the energetic range), with the implication that it is possible to infer the internal structure of a turbulent state, as one would by parsing through the successive ranges of the eddy velocity distribution, by parsing instead through the successive layers of the attendant MVP. We use the spectral theory to argue that a number of well-known, and as yet unresolved, disparities in the classical experimental data on friction factor in turbulent plane Couette flows stem from the existence of multiple states of turbulence that differ only at the largest lengthscales in the flow, corresponding to the energetic range, and are therefore consistent with small-scale universality. We also apply the spectral theory to thermally-stratified plane Couette flows of a type relevant to the atmosphere, and conclude that the spectral link remains bijective in the presence of thermal stratification, but the layers of the MVPs are altered by buoyancy. For the intermediate region, which is the only to have been previously theoretically studied, the spectral theory makes predictions in accord with the classical scaling of the Monin-Obukhov similarity theory (MOST); for the other regions (that which is near the wall and that which is far from the wall and extends beyond the intermediate region), the predictions of the spectral theory are in accord with a new set of scaling laws, which we are able to derive on the basis of dimensional analysis and similarity assumptions. We hope that our findings will foster the formulation of better spectral models which might help opening up new prospects of gaining further theoretical insight into turbulence, "the most important unsolved problem of classical physics".

Acknowledgment

My great thanks first go to my supervisors, Prof. Gustavo Gioia and Prof. Pinaki Chakraborty, not only for that they have effectively guided my research in all respects with their constructive advice, but also because I have learned much from them about how to better enjoy life.

I would also like to express my gratitude to all group members for creating a pleasant work environment, especially to Dr. Rory Cerbus, for providing me his simulation data, teaching me to do experiments, and always being patient with my questions; to Dr. Tinihau Meuel, for being patient to show me his interesting experimental data and his calculations; to Dr. Tapan Sabuwala, for kindly reading my manuscript and making useful comments; to Dr. Chien-chia Liu, for all kinds of pleasant discussions we had in some designated area; to Dr. Julio Manuel Barros, for his suggestive and critical comments on the thesis; to Lin Li, for sharing his numerical and theoretical results to me; to Yuna-san, for showing her experiments to me; to Christian Butcher, for helping me set up softwares; to William Powell, for the helpful questions he raised on the thesis when I was practising the thesis presentation; and to Kaori-san, for arranging all my business trips nicely. Besides, more special thanks go to Tapan and Rory, for being enthusiastic about organizing group get-together, which enriched my life.

My sincere gratitude also goes to my academic mentor, Prof. Sile Nic Chormaic, for her advice about courses selecting and research plan. I thank all the other professors I have studied with at OIST, such as Prof. Yabing Qi, Prof. Thomas Busch, Prof. Jonathan Miller, and Prof. Satoshi Mitarai. I am thankful to Prof. Mahesh Bandi and Prof. Jun Sakakibara for examining my thesis proposal and giving useful comments. I am also thankful to Prof. Bruce Sutherland and Prof. Soshi Kawai for carefully reading and examining my thesis, and giving helpful suggestions.

I am grateful for the financial support from graduate school and I am grateful to all of the staff at graduate school for all kinds of help they have provided during the last five and a half years, especially to Prof. Jeff Wickens, Prof. Ulf Skoglund, Dr. Harry Wilson, Kozue Higashionna-san, Midori Morinaga-san, Yoko Iha-san, and Kanae Oshiro-san. I am also grateful to all the fellow students of class 2012 for the fun we had together, especially to Cong Liu, Kenneth Baughman, Kalale Chola, and of course my brother, Dongxin Zhang.

I celebrate my friendship and brotherliness with Junmin Xia, and Haijun Ma. They and their families have helped me out in many ways since high school.

I thank all my families and my wife's families for supporting me without reservations.

The person I must thank most is definitely my brother, Dongxin. Nobody understands me better than he does.

The biggest thanks go to my beautiful wife, Xiaomin. Nobody tolerates me more than she does.

I also want to thank my daughter Xiaoxiao (Liuxi), my son Yiyi (Liuquan), and my niece Juanjuan (Lechen). They are the greatest delights.

Abbreviations

CV	control volume
DNS	direct numerical simulations
MOST	Monin-Obukhov similarity theory
MVP	mean-velocity profile

Nomenclature

Upper-case	
A	a dimensionless function
B	dimensionless constant of the “log law"
E	spectrum of turbulent kinetic energy
F	force
G	unspecified function
G_1	unspecified function
G_2	unspecified function
H_0	heat flux
H_s	turbulent heat flux
I	integration of the spectrum
I_s	integration of the spectrum at the flow centerline
I_0	dimensionless function for the integration of ϕ_1
I_1	dimensionless function for the integration of ϕ_{u3}
I_2	an equivalent form of I_1
I_3	dimensionless function for the integration of ϕ_{u2}
I_4	an asymptotic limit form of I_3
K	turbulent kinetic energy
K_s	turbulent kinetic energy of an eddy of size s
L	largest length scale in the flow
L_0	Obukhov length
M	momentum
Nu	Nusselt number
O	dimensionless function for the integration of ϕ_2
O_1	dimensionless function for the integration of ϕ_{u5}
O_2	an equivalent form of O_1
P	shear production
$\tilde{P}$	shear production normalized by ν/u_τ^4
Pr	Prandtl number
R	pipe radius
Ra	Rayleigh number
Ri_b	bulk Richardson number
Ri_τ	friction Richardson number
R_s	velocity slope at the flow centerline of plane Couette flow
Re	Reynolds number
Re_{L_0}	Reynolds number based on Obukhov length

Re_s	Reynolds number of an eddy of size s
Re_τ	friction Reynolds number
S	surface area
S_0	alternative velocity slope at the flow centerline of plane Couette flow
T	temperature
$\overline{T}$	time averaged local mean temperature
T'	fluctuating temperature component
δT	temperature variation
ΔT	temperature difference between the two walls of plane Couette flow or channel flow
U	mean velocity
V	turbulent velocity fluctuation (twice the turbulent kinetic energy)
$\tilde{V}$	turbulent velocity fluctuation normalized by u_τ^2
W	wetted surface
W_y	wetted surface at a distance y from the wall
X	length of control volume

Lower-case

a_i	a dimensionless variable
b	half width between the two plates of plane Couette flow
$\vec{e_i}$	unit vector
f	friction factor
g	gravitational acceleration
h	half width between the two plates of channel flow or plane Couette flow
k	wave number
k_d	thermal diffusivity
p	pressure
$\overline{p}$	time averaged local mean pressure
p_0	mean pressure at the wall
p'	fluctuating pressure component
r	sand grains size
s	eddy size
t	time
t_s	timespan that an eddy of size s lasts
u	time averaged local mean velocity
u_b	bulk velocity
u_c	centerline velocity
$\tilde{u}$	time averaged local mean velocity normalized by u_τ
$\tilde{u}_c$	centerline velocity normalized by u_τ
u_τ	friction velocity ($\sqrt{\tau_0/\rho}$)
$\vec{u}$	velocity field ($u_i\vec{e_i}$)
$\boldsymbol{u}$	same as $\vec{u}$
u_i	velocity in $\vec{e_i}$ direction
u_1	streamwise velocity
u_2	wall-normal velocity
u_3	spanwise velocity

$\overline{u_i}$	time averaged local mean velocity in $\vec{e_i}$ direction
$\overline{\boldsymbol{u}}$	time averaged local mean velocity
u_i'	fluctuating velocity component in $\vec{e_i}$ direction
$\boldsymbol{u'}$	fluctuating velocity component
u'	fluctuating velocity in streamwise direction
v'	fluctuating velocity in wall-normal direction
v_k	the characteristic velocity of an eddy of wavenumber k
v_{rms}	root mean square of wall-normal velocity fluctuation
$\tilde{v}_{rms}$	root mean square of wall-normal velocity fluctuation normalized by u_τ
v_s	the characteristic velocity of an eddy of size s
v_y	the characteristic velocity of an eddy of size y
x	Cartesian coordinate along streamwise direction
$\vec{x}$	position $(x_i\vec{e_i})$
x_1	streamwise position
x_2	wall-normal position
x_3	spanwise position
y	distance from the wall
y_1	arbitrary distance from the wall
$\tilde{y}$	distance from wall normalized by u_τ/ν
$\tilde{y}_v$	thickness of the viscous layer normalized by u_τ/ν
z	Cartesian coordinate along spanwise direction

Greek

α	thermal expansion coefficient
β_d	non-negative dimensionless parameter of the dissipative-range correction
β_e	non-negative dimensionless parameter of the energetic-range correction
Δ_o	constant $\Delta_o \gg 1$
ϵ_i	constant, $0 < \epsilon_i \ll 1$
$\tilde{\epsilon_i}$	constant, $0 < \tilde{\epsilon_i} \ll 1$
ε	turbulent power per unit mass or dissipation of turbulent kinetic energy
η	viscous length scale $(\nu^{3/4}\varepsilon^{-1/4})$
κ	“Kármán constant"$(0.4 \sim 0.41)$
κ_ε	dimensionless constant of the spectrum of turbulent kinetic energy
κ_τ	dimensionless parameter
ν	kinematic viscosity
ν_t	turbulent viscosity
ξ	dimensionless variable of integration
ρ	fluid density
$\overline{\rho}$	time averaged local mean density
ρ'	fluctuating density component
ρ_0	reference density
$\delta\rho$	density variation with respect to the reference density ρ_0
σ	dimensionless function of total shear stress
τ	total shear stress
τ_0	total shear stress at the wall

τ_t	turbulent shear stress
τ_{t12}	turbulent shear stress
τ_{v12}	viscous shear stress
$\vec{\tau}_t$	turbulent shear stress tensor
$\vec{\tau}_v$	viscous shear stress tensor
ϕ	dimensionless function for gradient of mean-velocity profile
ϕ_1	ϕ-like function
ϕ_2	ϕ-like function
$\tilde{\phi}$	an equivalent form of ϕ
$\tilde{\tilde{\phi}}$	an equivalent form of ϕ
ϕ_u	dimensionless function for gradient of mean-velocity profile
ϕ_{u1}	ϕ_u-like function
ϕ_{u2}	ϕ_u-like function
ϕ_{u3}	ϕ_u-like function
ϕ_{u4}	ϕ_u-like function
ϕ_{u5}	ϕ_u-like function
ϕ_{u6}	ϕ_u-like function

To my daughter Liuxi (流溪), my son Liuquan (流泉) and my niece
Juanjuan (涓涓), whose names are partly inspired from this thesis.

Contents

Declaration of Original and Sole Authorship **iii**

Abstract **v**

Acknowledgment **vii**

Abbreviations **ix**

Nomenclature **xi**

Contents **xvii**

List of Figures **xix**

1 Introduction **1**
- 1.1 A synopsis of the phenomenological theory 5
- 1.2 An example of application of the spectral link 8
- 1.3 Outline of the thesis 11

2 Spectral theory of wall-bounded turbulent flows **13**
- 2.1 Turbulent mean-velocity profiles 13
- 2.2 The spectrum of turbulent kinetic energy 15
- 2.3 Turbulent shear stress and spectral link 16
- 2.4 Equations of the MVPs 19
- 2.5 A note on the application of the spectral theory in this thesis 21
- 2.6 Comparison between pipe flow and channel flow 22
  - 2.6.1 Disparities of MVP 22
  - 2.6.2 Disparities of friction factor 25
  - 2.6.3 Disparities of shear production 26
- 2.7 Discussion and summary 28

3 Spectral theory of plane Couette flow **33**
- 3.1 Introduction 33
- 3.2 Spectral theory 36
  - 3.2.1 Attendant disparities in macroscopic properties other than the MVPs 37

3.3 A note on the asymptotic value of the velocity slope at the flow centerline 39
3.4 Discussion and summary 42

4 Spectral theory of thermally-stratified plane Couette flow 45
4.1 Introduction 45
4.2 The Monin-Obukhov similarity theory 46
4.3 Mean-velocity profile: empirical data 47
4.4 Mean-velocity profile: spectral theory 49
4.4.1 Mean-flow equations 49
4.4.2 Spectral link 51
4.4.3 The effect of the energetic-range correction 55
4.5 Generalized Monin-Obukhov similarity theory 55
4.5.1 Classic scaling laws for MVP 57
4.5.2 Scaling laws for ϕ_u 59
4.5.3 Scaling laws for MVP 62
4.6 Discussion and summary 70

5 Conclusion 73

Appendix A Total shear stress 77

Appendix B Turbulent power per unit mass 81

Bibliography 83

List of Figures

1.1 Leonardo da Vinci's sketch of a turbulent flow (chalked on paper, dated A.D. 1494). This turbulent flow consists of what might be termed as a "turbulent cauldron" that forms where a water jet, discharged from an orifice in the vertical wall on the right side of the sketch, plunges into a large pool of still water. The turbulent cauldron contains myriad eddies in a broad range of sizes; the largest eddy encompasses the entire domain of the turbulent cauldron whereas the smallest ones, which are quite numerous, have a characteristic size that is but a minute fraction of the size of the turbulent cauldron. The presence of eddies in a broad range of sizes is a cardinal property of turbulent flows (Sreenivasan, 1999; Davidson, 2004). 2

1.2 Schematic of the energy cascade, the crucial conception of the phenomenological theory of turbulence (Kolmogórov, 1941*a*,*b*). The largest eddy, of size commensurate with the size of the turbulent domain, R, appears at the top. The smallest eddies, of size set by the viscous lengthscale η, appear at the bottom. The turbulent kinetic energy, which is extracted by the largest eddies from the mean flow, is transferred from one generation of eddies to the next generation of eddies (of smaller size). Thus the turbulent kinetic energy "cascades" down through successive generations of increasingly smaller eddies, all of which are free of viscous effects, until it reaches the smallest eddies, where viscosity takes over and the turbulent kinetic energy is dissipated. According to Kolmogórov's analysis, discussed in the main text, the fundamental quantity which remains invariant over the entire range of lengthscales is the turbulent power per unit mass (Pope, 2000), ε, which represents the rate at which turbulent kinetic energy is transferred between any given generation of eddies and its immediate successor. 6

2.1 Log-linear plots of the MVPs of pipe flow in the wall variables $\tilde{u}$ and $\tilde{y}$ for four values of Re (Re_τ). The green symbols denote the data from direct numerical simulations (DNS) (El Khoury *et al.*, 2013) with $\mathrm{Re}_\tau = 999$ and the blue, black, and red symbols denote the data from experiments (Hultmark *et al.*, 2012, 2013) with $\mathrm{Re}_\tau = 3334, 10480$, and 98190, respectively. The grey line denotes the log law, $\tilde{u}(\tilde{y}) = \frac{1}{\kappa}\ln\tilde{y} + B$, with $\kappa = 0.4$ and $B = 5$. The dashed grey line denotes the laminar solution of the viscous layer, $\tilde{u}(\tilde{y}) = \tilde{y}$. Each MVP extends from the wall (which corresponds always to $\tilde{y} = 0$) to the centerline of the pipe (which corresponds to $\tilde{y} = \mathrm{Re}_\tau$); the MVPs collapse onto a single curve close to the wall. 14

2.2 Red line: model spectrum for $\beta_d = 7$, $\beta_e = 8$, and $L/\eta = 10^5$. Blue line: Kolmogórov spectrum without corrections. 17

2.3 Schematic used to derive an expression for the turbulent shear stress on the wetted surface W_y. For the coordinate axes, we choose the x axis to be along the streamwise direction and the y axis to be along the wall-normal direction. Note that $y = 0$ corresponds to the wall, so that W_y is at a distance y from the wall. 17

2.4 Plot of $\tilde{y}$ vs. η/y as per Equation 2.17, for $\kappa = 0.4$ and $\beta_d = 7$. The thick red dot indicates the point where $\tilde{y}$ is minimized; the minimum is denoted by $\tilde{y}_v$ and represents the thickness of the viscous layer. 20

2.5 Log-linear plots of typical MVPs of pipe flow (blue), channel flow (red) and plane Couette flow (black) in the "wall variables" $\tilde{u}$ and $\tilde{y}$ and for $\mathrm{Re}_\tau \simeq 1000$. The thin grey line denotes the log law, $\tilde{u}(\tilde{y}) = \frac{1}{\kappa}\ln\tilde{y} + B$ with $\kappa = 0.4$ and $B = 5$. The dashed grey line denotes the laminar solution of the viscous layer, $\tilde{u}(\tilde{y}) = \tilde{y}$. Each MVP extends to $\tilde{y} = \mathrm{Re}_\tau$, which corresponds to the centerline (or centerplane) of the flow. The data are from high fidelity direct numerical simulations (DNS): El Khoury *et al.* (2013) (pipe flow), Bernardini *et al.* (2014) (channel flow), Pirozzoli *et al.* (2014) (plane Couette flow). 23

2.6 Log-linear plots of the MVPs of pipe flow (blue) and channel flow (red) at the same value of $\mathrm{Re}_\tau = 1000$. The data are from DNS: El Khoury *et al.* (2013) (pipe flow), Bernardini *et al.* (2014) (channel flow). . . . 24

2.7 Log-linear plots of the MVPs of pipe flow (blue) and channel flow (red) at the same value of $\mathrm{Re}_\tau = 3000, 30000, 300000$ computed from the spectral theory with $\kappa = 0.4, \beta_d = 7$; and $\beta_e = 9$ for pipe flow, $\beta_e = 7$ for channel flow. 25

2.8 Log-linear plots of the friction factor of pipe flow (blue) and channel flow (red) as a function of Re. The data are from DNS: El Khoury *et al.* (2013) (pipe flow), Bernardini *et al.* (2014) (channel flow). 26

2.9 Log-linear plots of the friction factor of pipe flow (blue) and channel flow (red) as a function of Re computed from the spectral theory with $\kappa = 0.4$, $\beta_d = 7$; and $\beta_e = 9$ for pipe flow, $\beta_e = 7$ for channel flow. . . . 27

2.10 Log-linear plots of the friction factor of pipe flow (blue) and channel flow as a function of Re computed from the spectral theory with $\kappa = 0.4$, $\beta_d = 7$; and $\beta_e = 9$ for pipe flow, $\beta_e = 7$ (red) and $\beta_e = 2$ (black) for channel flow. For $\beta_e = 2$, the values of the friction factor of channel flow exceed those of pipe flow. 28

2.11 Log-linear plots of the shear production of pipe flow (blue) and channel flow (red) at the same value of $\mathrm{Re}_\tau = 1000$. The data are from DNS: El Khoury *et al.* (2013) (pipe flow), Bernardini *et al.* (2014) (channel flow). 29

2.12 Log-linear plots of the shear production of pipe flow (blue) and channel flow (red) at the same value of $\mathrm{Re}_\tau = 3000$ computed from the spectral theory with $\kappa = 0.4, \beta_d = 7$; and $\beta_e = 9$ for pipe flow, $\beta_e = 7$ for channel flow. Note that the blue line for pipe flow is covered by the red line for channel flow. 29

2.13 Log-linear plots of the premultiplied shear production of pipe flow (blue) and channel flow (red) at the same value of $\mathrm{Re}_\tau = 1000$. The data are from DNS: El Khoury *et al.* (2013) (pipe flow), Bernardini *et al.* (2014) (channel flow). 30

2.14 Log-linear plots of the premultiplied shear production of pipe flow (blue) and channel flow (red) at the same value of $\mathrm{Re}_\tau = 3000$ computed from the spectral theory with $\kappa = 0.4, \beta_d = 7$; and $\beta_e = 9$ for pipe flow, $\beta_e = 7$ for channel flow. 30

3.1 Log-linear plots of experimental and computational data on the relation between the friction factor f and the Reynolds number Re of plane Couette flow. □ Reichardt (1959). △ Telbany & Reynolds (1982). ■ Robertson (1959). ▲ Kitoh *et al.* (2005). ○ DNS from Lee & Kim (1991) (Green), Bech *et al.* (1995) (black), Tsukahara *et al.* (2006) (Purple), Avsarkisov *et al.* (2014) (Blue), and Pirozzoli *et al.* (2014) (Red), respectively. Solid lines are the empirical formulas from Telbany & Reynolds (1982): $0.0331/(\log \mathrm{Re})^2$, Robertson (1959): $0.0361/(\log \mathrm{Re})^2$, and Pirozzoli *et al.* (2014): $0.0399/(\log \mathrm{Re})^2$, respectively. 34

3.2 Log-linear plots of experimental and computational data on the MVPs of plane Couette flow. □ Reichardt (1959) at $\mathrm{Re}_\tau = 723$. △ Telbany & Reynolds (1982) at $\mathrm{Re}_\tau = 805$. ■ Robertson (1959) at $\mathrm{Re}_\tau = 700$. ▲ Kitoh *et al.* (2005) at $\mathrm{Re}_\tau = 192$. ○ DNS from Avsarkisov *et al.* (2014) (Blue) at $\mathrm{Re}_\tau = 550$, and Pirozzoli *et al.* (2014) (Red) at $\mathrm{Re}_\tau = 986$, respectively. The grey line denotes the log law, $\tilde{u}(\tilde{y}) = \frac{1}{\kappa} \ln \tilde{y} + B$ with $\kappa = 0.41$ and $B = 5$. The dashed grey line denotes the laminar solution of the viscous layer, $\tilde{u}(\tilde{y}) = \tilde{y}$. Each MVP extends from the wall to $\tilde{y} = \mathrm{Re}_\tau$.The MVPs collapse onto a single curve close to the wall in the viscous layer, the buffer layer, and the log layer while there are significant discrepancies displaying in the wakes. 35

3.3 Log-linear plots of experimental and computational data on the relation between the non-dimensional velocity slope at the flow centerline, R_s, and the Reynolds number Re of plane Couette flow. △ Telbany & Reynolds (1982). ■ Robertson (1959). ▲ Kitoh *et al.* (2005). ○ DNS from Tsukahara *et al.* (2006) (Purple), Avsarkisov *et al.* (2014) (Blue), and Pirozzoli *et al.* (2014) (Red), respectively. 36

3.4 Log-linear plots of the friction factor of plane Couette flow as a function of Re computed from the spectral theory with $\kappa = 0.41, \beta_d = 7$, and three different values of β_e: $\beta_e = 1$ (black line), $\beta_e = 2$ (red line), $\beta_e = 3$ (blue line). 37

3.5 Log-linear plots of the MVPs of plane Couette flow at the same value of $\mathrm{Re}_\tau = 1000$ computed from the spectral theory with $\kappa = 0.41, \beta_d = 7$, and three different values of β_e: $\beta_e = 1$ (black line), $\beta_e = 2$ (red line), $\beta_e = 3$ (blue line). 38

3.6 Plots of experimental and computational data on the turbulent velocity fluctuation profiles of plane Couette flow. △ Telbany & Reynolds (1982) at $\mathrm{Re}_\tau = 805$. ○ DNS from Avsarkisov *et al.* (2014) (Blue) at $\mathrm{Re}_\tau = 550$, and Pirozzoli *et al.* (2014) (Red) at $\mathrm{Re}_\tau = 986$, respectively. 39

3.7 Schematic used to derive the expression for the turbulent wall-normal velocity fluctuation $v_{rms}(y)$. 40

3.8 Plots of experimental and computational data on the turbulent wall-normal velocity fluctuation profiles of plane Couette flow. △ Telbany & Reynolds (1982) at $\mathrm{Re}_\tau = 805$. ○ DNS from Avsarkisov *et al.* (2014) (Blue) at $\mathrm{Re}_\tau = 550$, and Pirozzoli *et al.* (2014) (Red) at $\mathrm{Re}_\tau = 986$, respectively. 41

3.9 Plots of the turbulent wall-normal velocity fluctuation profiles of plane Couette flow at the same value of $\mathrm{Re}_\tau = 1000$ computed from the spectral theory with $\kappa = 0.41, \beta_d = 7$, and three different values of β_e: $\beta_e = 1$ (black line), $\beta_e = 2$ (red line), $\beta_e = 3$ (blue line). 41

3.10 Log-linear plots of the non-dimensional velocity slope at the flow centerline R_s of plane Couette flow as a function of Re computed from the spectral theory with $\kappa = 0.41, \beta_d = 7$, and three different values of β_e: $\beta_e = 1$ (black line), $\beta_e = 2$ (red line), $\beta_e = 3$ (blue line). The dashed grey lines denote that at high Reynolds numbers, the constant values of $R_s = 2.86, 3.34$, and 3.69 for $\beta_e = 1$, $\beta_e = 2$, and $\beta_e = 3$, respectively. . 42

3.11 Log-linear plots of the non-dimensional velocity slope at the flow centerline S_0 of plane Couette flow as a function of Re computed from the spectral theory with $\kappa = 0.41, \beta_d = 7$, and three different values of β_e: $\beta_e = 1$ (black line), $\beta_e = 2$ (red line), $\beta_e = 3$ (blue line). 43

4.1 Log-linear plot of the MVPs in the "wall variables", $\tilde{u}$ vs. $\tilde{y}$. Filled symbols are DNS data for unstably-stratified channel flows from Pirozzoli *et al.* (2017) with $Pr = 1$: upward-pointing triangles denote $h/L_0 = -12.04, \mathrm{Re}_\tau = 179$, diamonds denote $h/L_0 = -1.47, \mathrm{Re}_\tau = 351$, downward-pointing triangles denote $h/L_0 = -0.18, \mathrm{Re}_\tau = 864$, and squares denote $h/L_0 = 0, \mathrm{Re}_\tau = 816$. Empty symbols are DNS data for stably-stratified flows. Green data are for stably-stratified channel flows from García-Villalba & del Álamo (2011) with $Pr = 0.7, \mathrm{Re}_\tau = 550$: squares denote $h/L_0 = 0$, circles denote $h/L_0 = 0.22$, downward-pointing triangles denote $h/L_0 = 0.34$, diamonds denote $h/L_0 = 0.84$, and upward-pointing triangles denote $h/L_0 = 1.36$. Red data are for stably-stratified plane Couette flow from García-Villalba *et al.* (2011) (in this case h/L_0 can not be computed from the data provided in this paper) with $Pr = 0.7, \mathrm{Re}_\tau = 540$: circles denote $Ri_b = 0$, downward-pointing triangles denote $Ri_b = 0.03$, diamonds denote $Ri_b = 0.06$, and upward-pointing triangles denote $Ri_b = 0.1$. Black data are for stably-stratified plane Couette flow from Deusebio *et al.* (2015) with $Pr = 0.7$: upward-pointing triangles denote $h/L_0 = 1.37, \mathrm{Re}_\tau = 349$, diamonds denote $h/L_0 = 3.78, \mathrm{Re}_\tau = 520$. 49

4.2 Deviation from the log law due to unstable and stable stratification. Figure from the classic textbook Turner (1973). Note that compared with Fig. 4.1, the axes are flipped. Also note that here the distance from the wall is denoted by z. 50

4.3 Log-linear plots of theoretically-predicted MVPs in wall variables. The MVPs correspond to a fixed $\mathrm{Re}_\tau = 10^6$ and various values of h/L_0. The red line corresponds to the flow of constant-density fluids with $h/L_0 = 0$; the blue lines correspond to unstably-stratified flows with $h/L_0 = -10, -100, -1000, -10000$; and the green lines correspond to stably-stratified flows with $h/L_0 = 10, 20, 50, 100$. As the absolute value of h/L_0 increases, the MVPs deviate more from the flow of constant-density fluids. For computing the curves using the spectral theory, we set $\kappa = 0.4, \beta_e = 2$, and $\beta_d = 5.2$. 54

4.4 Log-linear plots of theoretically-predicted MVPs in wall variables. The MVPs correspond to a fixed $\mathrm{Re}_\tau = 10^6$ and various values of h/L_0. The red line corresponds to the flow of constant-density fluids with $h/L_0 = 0$; the blue lines correspond to unstably-stratified flows with $h/L_0 = -100, -1000,$; and the green lines correspond to stably-stratified flows with $h/L_0 = 10, 20$. As the absolute value of h/L_0 increases, the MVPs deviate more from the flow of constant-density fluids. For computing the curves using the spectral theory, we set $\kappa = 0.4, \beta_d = 5.2$,and $\beta_e = 1$. To see the effect of the energetic-range correction, the dashed black curves are computed with the same values of κ and β_d, but with $\beta_e = 7$. . . . 56

4.5 Log-log plots of ϕ_u vs y/L_0 for: (a) unstable stratification, and (b) stable stratification. For computing the curves using the spectral theory, we set $\kappa = 0.4, \beta_e = 2$, and $\beta_d = 5.2$. 57

4.6 Testing the generalized MOST for the inner layer. Log-log plots of ϕ_u vs. y/L_0 for: (a) unstable stratification, (b) stable stratification. Note the collapsed curves near the wall. For computing the curves using the spectral theory, we set $\kappa = 0.4, \beta_e = 2$, and $\beta_d = 5.2$. 61

4.7 Testing the generalized MOST for the outer layer. Log-log plots of ϕ_u vs. y/L_0 for: (a) unstable stratification, (b) stable stratification. Note the collapsed curves far from the wall. For computing the curves using the spectral theory, we set $\kappa = 0.4, \beta_e = 2$, and $\beta_d = 5.2$. 63

4.8 Testing the law of the wall for thermally-stratified flows. Log-linear plots of $\tilde{u}$ vs. $\tilde{y}$ for: (a) unstable stratification, (b) stable stratification. Note the collapsed curves near the wall. For computing the curves using the spectral theory, we set $\kappa = 0.4, \beta_e = 7$, and $\beta_d = 5.2$. 65

4.9 Testing the law of the wall for thermally-stratified flows using DNS data of stably-stratified plane Couette flows from García-Villalba *et al.* (2011) and Deusebio *et al.* (2015). Log-linear plots of $\tilde{u}$ vs. $\tilde{y}$. The curve denoted by red upward-pointing triangles corresponds to $\mathrm{Re}_\tau = 540, \mathrm{Re}_{L_0} = 245$, and the curve denoted by black upward-pointing triangles corresponds to $\mathrm{Re}_\tau = 349, \mathrm{Re}_{L_0} = 255$. Note that these curves collapse onto each other over the largest extent near the wall. Actually, we can not calculate the value of Re_{L_0} directly for the curve denoted by red upward-pointing triangles because not enough details are provided in García-Villalba *et al.* (2011). However, we found a very similar simulation (see also “Run 21” in Zhou *et al.* (2017)) in Deusebio *et al.* (2015), from which we estimate the value of $\mathrm{Re}_{L_0} = 245$, which is very similar to the value of $\mathrm{Re}_{L_0} = 255$ for the curve denoted by black upward-pointing triangles. 66

4.10 Testing the extent of the law of the wall, Equation 4.44. Log-linear plots of $\tilde{u}$ vs. $\tilde{y}$ for: (a) unstable stratification, (b) stable stratification. We fix h/L_0 and vary Re_{L_0}. Note the collapsed curves near the wall. For computing the curves using the spectral theory, we set $\kappa = 0.4, \beta_e = 7$, and $\beta_d = 5.2$. 68

4.11 Testing the defect law for thermally-stratified flows. Log-linear plots of $\tilde{u}_c - \tilde{u}$ vs. y/h for: (a) unstable stratification, (b) stable stratification. Note the collapsed curves far from the wall. For computing the curves using the spectral theory, we set $\kappa = 0.4, \beta_e = 7$, and $\beta_d = 5.2$. 69

Chapter 1

Introduction

Flows of high Reynolds number, wherein the ratio between inertial forces and viscous forces is much larger than 1, display turbulence, a state characterized by velocity fields that fluctuate in broad, continuous ranges of lengthscales (Sreenivasan, 1999; Davidson, 2004). Leonardo da Vinci (1452–1519) might have been the first person to put forth a picture of "*la torbolenza*" (reproduced in Fig. 1.1). In a hand-written note, Leonardo tells us that he derived that picture from careful observation:

> Observe the motion of the surface of the water, which resembles that of hair, which has two motions, of which one is caused by the weight of the hair, the other by the direction of the curls; thus the water has eddying motions, one part of which is due to the principal current, the other to random and reverse motion (Piomelli's translation in Lumley (1992)).

Leonardo's distinction between that part of a flow "which is due to the principal current" and that other part which consists of "random and reverse motion," foreshadows the Reynolds decomposition (Pope, 2000), a mainstay of modern theoretical turbulence whereby velocity fields are decomposed additively into mean and fluctuating components. Furthermore, the fluctuating component (that is, the "random and reverse motion") continues to be thought of in the way Leonardo did (as may be inferred from his hand-written note): that is, as an aggregate of ephemeral swirling currents or "turbulent eddies" (Pope, 2000). And, in fact, such eddies are still with us, prominent as the basic components of the internal structure of turbulence in Kolmogórov's phenomenological theory of turbulence (Frisch, 1995). Thus, in retrospect, the picture of Fig. 1.1 and the hand-written note that Leonardo affixed to it, taken together, might have raised sensible expectations of a speedy development in theoretical turbulence.

And yet, five hundred years after Leonardo and almost two centuries after the first derivation, in the 1840s, of the Navier-Stokes equations that govern incompressible flows (Kundu & Cohen, 2002), turbulent ones included, theoretical progress has been meagre. The Navier-Stokes equations have not been solved analytically for any turbulent flow directly relevant to an engineering application or natural phenomenon. Turbulence has been said to be "the most important unsolved problem of classical physics" (Feynman *et al.*, 1963). It is certainly the most conspicuous unsolved problem in mathematical classical physics, and as such it is likely to remain unsolved in future, for there seems

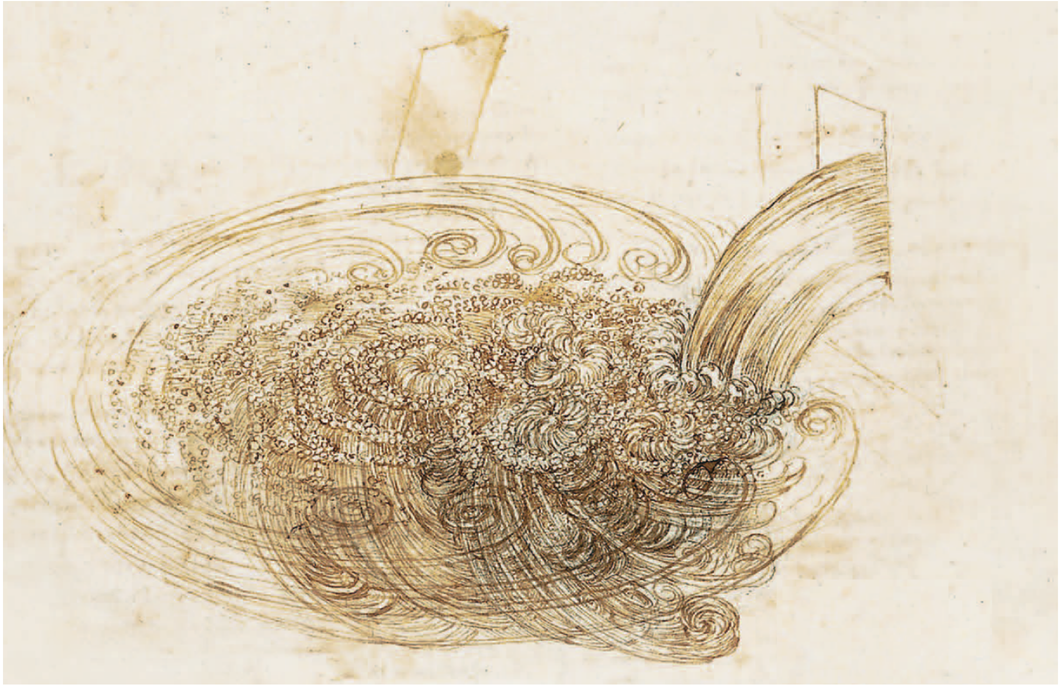

Fig. 1.1: Leonardo da Vinci's sketch of a turbulent flow (chalked on paper, dated A.D. 1494). This turbulent flow consists of what might be termed as a "turbulent cauldron" that forms where a water jet, discharged from an orifice in the vertical wall on the right side of the sketch, plunges into a large pool of still water. The turbulent cauldron contains myriad eddies in a broad range of sizes; the largest eddy encompasses the entire domain of the turbulent cauldron whereas the smallest ones, which are quite numerous, have a characteristic size that is but a minute fraction of the size of the turbulent cauldron. The presence of eddies in a broad range of sizes is a cardinal property of turbulent flows (Sreenivasan, 1999; Davidson, 2004).

to be scant prospect that the Navier-Stokes equations will ever be solved analytically for any shear flow in the turbulent regime (Moin & Mahesh, 1998; Doering, 2009).

As a general problem (and not just a narrowly mathematical one), turbulence is important on account of the myriad engineering applications that involve turbulent flows (Rodi, 1993; Menter, 1994; Davidson, 2004). In this regard, engineers and applied scientists have been chiefly interested in the macroscopic properties of the canonical wall-bounded turbulent flows (Frisch, 1995; Sreenivasan, 1999; Marusic *et al.*, 2010; Smits *et al.*, 2011; Kim, 2012), a class of flows that consists of pipe flow, channel flow, boundary layer flow, plane Couette flow, and Taylor-Couette flow (Pope, 2000; Kundu & Cohen, 2002). The most notable macroscopic properties are the turbulent friction and the turbulent mean-velocity profile (Tennekes & Lumley, 1972; Zagarola & Smits, 1998; Furuichi *et al.*, 2015). The turbulent friction quantifies the shear stress that develops between a turbulent flow and its bounding walls. It is the property of a flow that sets the cost of pumping oil through a pipeline (Kelland, 2014) and the draining capacity of a river in flood (Bridge, 2009), to cite but two examples. Closely related to the turbulent friction, the turbulent mean-velocity profile represents the spatial distribution of the local mean-velocity in a turbulent flow. It is used to compute fluxes, diffusivities and other quantities of interest in hydraulics, geomorphology, environmental science and allied disciplines (Tennekes & Lumley, 1972; Pope, 2000).

The macroscopic (or external) properties can be defined and measured without committing to any specific theoretical assumptions on the internal structure of turbulence (Robinson, 1991). Thus, for example, the turbulent friction can be readily calculated by measuring the shear stress at the wall, where the flow is invariably viscous and the Newtonian relation between shear stress and shear strain rate applies (Kundu & Cohen, 2002); there is no need to posit eddies or hairpin vortices or coherent structures or any of the variously concrete, abstract or (on occasion) fanciful entities which have been held to be the elementary components of the internal structure of turbulence (Hussain, 1983; Robinson, 1991; Smith & Walker, 1995; Adrian, 2007; Mathur *et al.*, 2007), and to which a fundamental role has been ascribed in the mechanical workings of turbulent flows. To satisfy the need for actionable knowledge on the macroscopic properties of turbulent flows, engineers and applied scientists have been able to pursue an empirical approach unencumbered by theoretical overheads.

Indeed, wall-bounded turbulent flows have been extensively researched by means of laboratory experiments and numerical simulations (Marusic *et al.*, 2010; Smits *et al.*, 2011; Kim *et al.*, 1987; Eggels *et al.*, 1994; Bernardini *et al.*, 2014; Orlandi *et al.*, 2015). Simulations make soaring computational demands as the Reynolds number increases, and they become impracticable even at modest Reynolds numbers (Moin & Mahesh, 1998; Ishihara *et al.*, 2009; Toschi & Bodenschatz, 2009). On the other hand, laboratory experiments capable of detailed probing of velocity fields have been recently carried out at Reynolds numbers as high as 10^7 (Zagarola & Smits, 1998; Mckeon *et al.*, 2004; Hultmark *et al.*, 2012, 2013; Furuichi *et al.*, 2015), motivated by engineering projects in which cost is of little concern. More complicated turbulent flows such as atmospheric and oceanic flows (Gargett, 1989; Fernando, 1991; Garratt, 1994; Wunsch & Ferrari, 2004; Wallace & Hobbs, 2006) are of significant practical importance but require field measurements which are more likely than laboratory measurements to display scatter and uncertainties. Nevertheless, there are plenty of high-quality, beautiful data on the turbulent friction and the mean-velocity profiles of both relatively simple wall-bounded turbulent flows and environmental turbulent flows, collected from laboratory experiments, numerical simulations, and field measurements. In many cases the data, dating back several decades, furnish an empirical understanding of the macroscopic properties of a turbulent flow that is as thorough as may be desired. In the absence of analytical solutions to the Navier-Stokes equations, however, the data are yet to be properly explained. To account for the empirical evidence and shed some theoretical light on the macroscopic properties of turbulent flows, we need to look beyond the Navier-Stokes equations.

Beside the Navier-Stokes equations, Kolmogórov's phenomenological theory of turbulence, which dates back to the 1940s (Kolmogórov, 1941*a*,*b*), is the most striking achievement of theoretical turbulence to date. It yields profound, quantitative, testable predictions on the internal structure of turbulence.

In the phenomenological theory, as in Leonardo's picture (Fig. 1.1), turbulence is posited to consist of a jumble of turbulent eddies in a broad range of sizes. The aim of the theory is to develop a theoretical understanding of these eddies, which are, in principle, the sole immediate concern of the phenomenological theory. Thus, the theory focuses on the internal structure of turbulence and bears no ostensible relation to the macroscopic properties of the flow.

In essence, the phenomenological theory allows us to ascribe a characteristic velocity v_s to any given turbulent eddy in the flow, depending on the size of the eddy, s. In other words, the theory yields the eddy velocity distribution $v_s(s)$. This eddy velocity distribution has been extensively verified empirically by means of suitable experimental and computational measurements which pertain only to the internal structure of the flow (Pope, 2000).

At this stage it is convenient to recapitulate the most salient points of our discussion so far. We have been dealing with two distinct aspects of turbulent flows, namely

1. The macroscopic properties, which are defined and measured experimentally without invoking turbulent eddies or any other feature of the internal structure of a flow. What is known about the macroscopic properties is essentially empirical in nature and lacking in theoretical explanation.

2. The eddy velocity distribution, which is concerned exclusively with the internal structure of the flow and has been extensively verified by means of measurements unrelated to the macroscopic properties. It can be deemed an established empirical fact firmly grounded on the phenomenological theory of turbulence.

For many decades, these two aspects of turbulent flows have remained strictly separate, the subjects of utterly unrelated research efforts and disconnected chapters in books on fluid mechanics (Frisch, 1995; Pope, 2000). This separation is strange. As distinct aspects of one and the same physical phenomenon (the turbulent flow), the macroscopic properties and the eddy velocity distribution *must* be inextricably linked to one another.

And yet this point, which may entail little beyond logic, and seems hardly apt at occasioning scandal, or even skepticism, has seldom been made. A notable exception is that of Tennekes & Lumley (1972), who in the 1970s surmised that the mean-velocity profiles of pipe flows must be closely related to the spectrum of turbulent kinetic energy (or “the spectrum”, as we shall frequently call it thereafter), which is but an alternative form of the eddy velocity distribution.

This thesis is predicated on the certainty that the macroscopic properties and the eddy velocity distribution (or, equivalently, the spectrum of turbulent kinetic energy), are indeed closely related to one another. We shall refer to this close relation as the “spectral link”, and make use of concrete forms of the spectral link (between the turbulent friction and the eddy velocity distribution, for example) to shed some theoretical light on a number of outstanding problems in turbulence. In particular, we aim to explain theoretically, solely on the basis of the phenomenological theory, and circumventing altogether the Navier-Stokes equations, some of the macroscopic properties of turbulent flows on which there exists a hitherto unexplained, extensive corpus of empirical data.

In what remains of the present introductory chapter, we review the most salient concepts, assumptions and results of the phenomenological theory. Then, we illustrate the import and implications of the spectral link by way of an example due to Gioia & Chakraborty (2006) and Tran *et al.* (2010), who devised a concrete form of the spectral link for the turbulent friction in pipes and put it to use to show that the classical empirical scalings of the turbulent friction in rough and smooth pipes are but macroscopic manifestations of the eddy velocity distribution of the phenomenological theory. Last, we outline the research that is to be be expounded in detail in the remaining chapters of the thesis.

1.1 A synopsis of the phenomenological theory

The phenomenological theory owes its name to the fact that it has not been derived mathematically from the Navier-Stokes equations. Instead, it has been predicated on dimensional analysis, a suitable set of similarity assumptions (Barenblatt, 1996), and the "energy cascade", an insightful conception of turbulence as a physical phenomenon structured around a recursive set of energetic exchanges, with precedent in the work of Richardson (1922).

The phenomenological theory posits that turbulence consists of a jumble of eddies in a broad range of sizes, as might be inferred from Leonardo's sketch of Fig. 1.1. The largest eddy (at the top of Fig. 1.2) has a size R commensurate with the size of the turbulent domain, and a characteristic velocity U; in pipe flow, for example, R might be the radius of the pipe and U might be the mean velocity of the flow (that is, the volume flux normalized by the cross-sectional area of the pipe). Thus, the Reynolds number of the largest eddy, UR/ν (that is, the characteristic velocity of the eddy times the size of the eddy normalized by the kinematic viscosity of the fluid, ν), coincides with the Reynolds number of the flow, $\mathrm{Re} \equiv UR/\nu$ (that is, the size of the turbulent domain times the mean velocity of the flow normalized by the kinematic viscosity). If the flow be turbulent, Re is large and the largest eddy is also turbulent; therefore, the dynamics of the largest eddy is dominated by inertial forces.

Consider next an eddy of generic size s and characteristic velocity v_s. For the time being, let us assume that this eddy is turbulent, so that ν is irrelevant to its dynamics. (In other words, we assume that the generic eddy of size s is inertial, or free of viscous effects.) The eddy has a turbulent kinetic energy per unit mass K_s, where K_s is of course proportional to v_s^2. Kolmogórov postulated that the eddy lasts for a timespan t_s and becomes unstable, whereupon it undergoes fission—that is, it splits into, say, two eddies of size $s/2$ (Fig. 1.2), in such a way that the turbulent kinetic energy cascades from the lengthscale s down to a smaller lengthscale $s/2$. Now, given s and v_s, we can form a single timescale, namely s/v_s (because ν is irrelevant to the dynamics of the eddy), with the implication that the lifespan t_s is proportional to s/v_s. It follows that the rate at which turbulent kinetic energy per unit mass is transferred from the lengthscale s down to the lengthscale $s/2$, a quantity customarily denoted by ε and known as the turbulent power per unit mass, must be proportional to K_s/t_s, or $\varepsilon \propto v_s^3/s$ (Pope, 2000). Note that ε has the correct units of power per unit mass; thus, as in the rest of this thesis, the symbol "$\propto$" signifies "equal to except for a dimensionless multiplicative constant". Under steady conditions, the turbulent power per unit mass should be the same for the entire energy cascade—that is, ε should be independent of s. We conclude that the eddy velocity distribution can be expressed as

$$v_s \propto (\varepsilon\, s)^{1/3}, \tag{1.1}$$

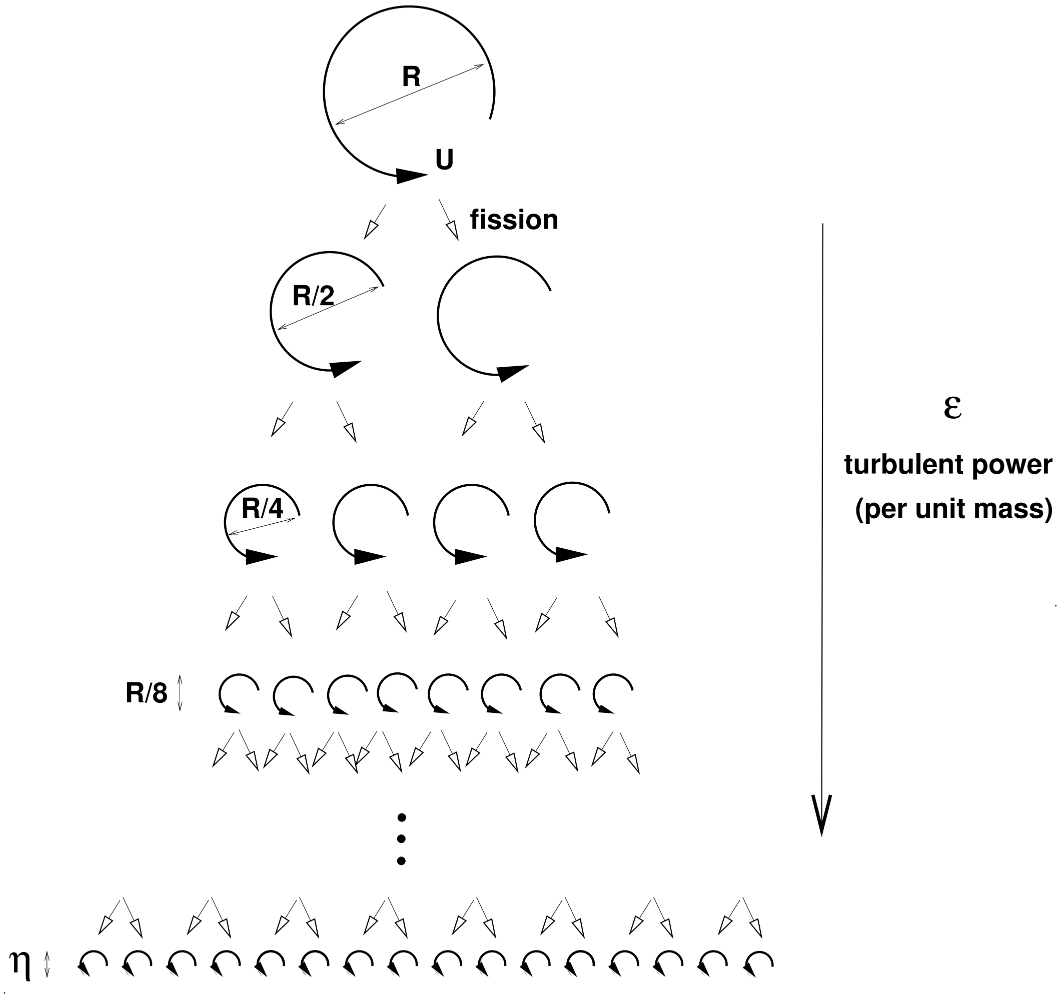

Fig. 1.2: Schematic of the energy cascade, the crucial conception of the phenomenological theory of turbulence (Kolmogórov, 1941*a*,*b*). The largest eddy, of size commensurate with the size of the turbulent domain, R, appears at the top. The smallest eddies, of size set by the viscous lengthscale η, appear at the bottom. The turbulent kinetic energy, which is extracted by the largest eddies from the mean flow, is transferred from one generation of eddies to the next generation of eddies (of smaller size). Thus the turbulent kinetic energy "cascades" down through successive generations of increasingly smaller eddies, all of which are free of viscous effects, until it reaches the smallest eddies, where viscosity takes over and the turbulent kinetic energy is dissipated. According to Kolmogórov's analysis, discussed in the main text, the fundamental quantity which remains invariant over the entire range of lengthscales is the turbulent power per unit mass (Pope, 2000), ε, which represents the rate at which turbulent kinetic energy is transferred between any given generation of eddies and its immediate successor.

where ε is independent of s (invariant), and therefore a property of the local turbulence. This is the most fundamental result of the phenomenological theory of turbulence.

Equation 1.1 allows us to ascribe a specific characteristic velocity, namely v_s, and a specific turbulent kinetic energy per unit mass, namely v_s^2 (or K_s), to any eddy of size s. Thus, Equation 1.1 expresses the way in which the turbulent kinetic energy is apportioned among eddies of different sizes in a flow, and may be said to embody in mathematical form the internal structure as well as the energetics of turbulence.

The cardinal datum in Equation 1.1 is the value of the exponent. That value, 1/3, cannot be determined solely on the basis of dimensional analysis and similarity assumptions. It hinges instead on the conceptual picture of turbulence put forth by Kolmogórov, with the turbulent eddies of various sizes, the energy cascade in which they partake, and the attendant multi-lengthscale physics.

Now, we expect Equation 1.1 to break down where the eddy of size s ceases to be dominated solely by inertial forces and becomes subject to viscous effects. Let us denote the Reynolds number of that eddy with $\mathrm{Re}_s \equiv v_s s/\nu$. From Equation 1.1, we can readily conclude that

$$\mathrm{Re}_s \propto \varepsilon^{1/3} s^{4/3} \nu^{-1}. \tag{1.2}$$

Thus, for any given value of ε (or, equivalently, for any given energy cascade), Re_s diminishes as s diminishes. The viscous lengthscale η is defined as the characteristic size of the smallest eddy that is free of viscous effects (Davidson, 2004), and can be readily computed by setting $\mathrm{Re}_s = 1$, with the result

$$\eta \propto \varepsilon^{-1/4} \nu^{3/4}, \tag{1.3}$$

which is a property of the local turbulence.

To achieve a better grasp on the implications of Equation 1.3, let us assume (as we shall do in Section 1.2) that the entire turbulent domain evinces a single value of ε—that is, that the energy cascade is one and the same everywhere in the turbulent flow. In this case, we can set $\varepsilon \propto U^3/R$ (an estimate for ε known as the Taylor scaling (Pope, 2000)); substitution in Equation 1.1, in Equation 1.2 and in Equation 1.3 gives

$$v_s \propto (s/R)^{1/3} U, \tag{1.4}$$

$$\mathrm{Re}_s \propto (s/R)^{4/3} \mathrm{Re}, \tag{1.5}$$

and

$$\eta \propto R\,\mathrm{Re}^{-3/4}, \tag{1.6}$$

respectively. The first of these equations is an alternative form of the eddy velocity distribution. The second equation is consistent with two observations made in the preceding pages: (1) that the Reynolds number of an eddy of size R coincides with the Reynolds number of the flow and (2) that the Reynolds number of an eddy diminishes as the size of the eddy diminishes. On the other hand, Equation 1.6 indicates that, other things remaining equal, the smallest eddy in the *inertial range* (the range of sizes in which Equation 1.1 applies) becomes smaller as Re increases. In other words, an increase in Reynolds number results in a broadening of the range of sizes encompassed by the turbulent eddies of the inertial range.

As we shall see later on, to account for the effect of viscosity on the energy cascade, the right-hand side of Equation 1.1 should be affected by a multiplicative correction, the *dissipative-range correction*, which is a function of η/s that equals 1 everywhere except in the range of sizes (or lengthscales) known as the *dissipative range*, namely

$s \lesssim \eta$, where the dissipative-range correction is less than 1 (Pope, 2000; Gioia *et al.*, 2010).

Just as Equation 1.1 breaks down where s becomes comparable to the viscous lengthscale, it also breaks down where s becomes comparable to the size of the turbulent domain, R. In fact, as we shall see later on, the right-hand side of Equation 1.1 should be multiplied by the *energetic-range correction*, which is a function of s/R that equals 1 everywhere except in the range of lengthscales known as the *energetic range*, namely $s \gtrsim R$, where the energetic-range correction is less than 1 (Pope, 2000; Gioia *et al.*, 2010).

The energetic-range correction owes its name to the fact that it pertains to the largest eddies (those of the energetic range), which contain most of the turbulent kinetic energy in the flow. Nevertheless, the energetic-range correction accounts for the effect of the finite turbulent domain: eddies of a size close to the size of that domain might be thought of, intuitively, as being encumbered by the presence of boundaries, with the implication that their characteristic velocities are lessened as compared with those of imaginary eddies of the same size in a flow of larger turbulent domain. Regardless of the properness of this intuitive argument (which is admittedly rather loose), it should be apparent that the energetic-range correction, unlike the dissipative-range correction, can change from flow to flow. (Because different flows have different boundaries which affect the largest eddies in the flow in different ways.) In other words, *turbulence in the energetic range is expected to depend on the type of flow whereas turbulence in both the inertial range and the dissipative range can be deemed universal,* that is to say, one and the same for all types of flow (Kolmogórov, 1941*b*; Schumacher *et al.*, 2014). This is a point worth remembering as it will recur in the remaining chapters of this thesis.

1.2 An example of application of the spectral link

It may be argued that the turbulent friction is the most important macroscopic property of wall-bounded turbulent flows. The conventional measure of fluid friction, whether the flow be viscous or turbulent, is the friction factor f, which may be defined as the dimensionless ratio $f \equiv \tau/\rho U^2$, where τ is the shear stress that develops between the flow and the wall, ρ is the density of the fluid, and U is the mean velocity of the flow. For concreteness, let us focus our discussion on pipe flow, in which case the Reynolds number Re of the flow is defined in the form $\mathrm{Re} \equiv UR/\nu$, where R is the radius of the pipe and ν is the kinematic viscosity of the fluid. Where the flow is viscous, it is possible to conclude directly from the Navier-Stokes equations that $f \propto \mathrm{Re}^{-1}$ (Massey & Ward-Smith, 1998), regardless of whether the wall of the pipe be smooth or rough. This prediction has been amply verified empirically (Reynolds, 1883; Massey & Ward-Smith, 1998; Cerbus *et al.*, 2018).

Where the flow is turbulent, the Navier-Stokes equations have proven of little help to engineers, and efforts to ascertain scaling relations for f on an empirical basis go back to the XVIII Century France, where f was the subject of large-scale experiments carried out apropos of the design of a water-supply system for the city of Paris (Chézy, 1776; Mouret, 1921). Modern experiments dating back to the early XX Century revealed that for smooth-walled flows of moderate turbulent strength (Re up to about

10^5 (McKeon *et al.*, 2005)), the experimental measurements are well described by the Blasius empirical scaling (Blasius, 1913), $f \propto \mathrm{Re}^{-1/4}$. On the other hand, for flows over rough walls of a single lengthscale, in which sand grains of size r (where $r \ll R$) are glued as a lining on the wall of the pipe, f becomes independent of Re at high Re ($\mathrm{Re} \gtrsim 10^6$ (Massey & Ward-Smith, 1998)) and the experimental measurements are well described by the Strickler empirical scaling (Manning, 1890; Strickler, 1923), $f \propto (r/R)^{1/3}$, where r/R is the dimensionless roughness. It bears emphasis that the exponent of Strickler, 1/3, as well as the exponent of Blasius, $-1/4$, was determined by fitting experimental data. The fact that both exponents are written as fractions is a matter of convenience and should not be construed as denoting theoretical certainty.

To provide a theoretical explanation of the empirical scalings of Blasius and Strickler, we seek to establish a link between f and the eddy velocity distribution of the phenomenological theory (Gioia & Chakraborty, 2006). To that end, consider a wetted cylindrical surface tangent to the sand grains that jut out from the wall and into the turbulent flow. Let us denote that wetted surface by W. Note that the shear stress τ that appears in the definition of f is but the shear stress that acts on W.

On one side of W there is the bulk of the flow, where the fluid moves along the axis of the pipe with mean velocity U. On the other side of W there are the sand grains and the set of fluid-filled cavities left between adjacent sand grains. The size of these cavities scales with r, the size of the sand grains, and the fluid that fills the cavities is at rest—that is, the mean velocity of the flow within each cavity is naught. (Note that this is a binary model: the velocity is assumed to be uniform and equal to U on one side of W, naught on the other side.) In the turbulent regime, τ arises from the exchange of momentum between the bulk of the flow on one side of W and the fluid-filled cavities of the other side of W. This exchange of momentum is effected by turbulent eddies which straddle W.

Consider one such eddy of generic size s, where $s \leq r$. (The need for this restriction will become apparent shortly.) W bisects the eddy into two equal halves. (That is, the eddy straddles W.) One half sweeps through the bulk of the flow. The other half sweeps through one of the cavities of size r (which necessitates the restriction above). Thus the eddy picks up fluid from the bulk of the flow on one side of W (where the momentum per unit volume of fluid is ρU) and deposits it inside the cavity on the other side of W (where the momentum per unit volume of fluid is naught), and at the same time it picks up fluid from inside the cavity and deposits it in the bulk of the flow. The shear stress created by the eddy on W can be computed as the momentum contrast across W (which equals ρU, or $\rho U - 0$) times the rate at which the eddy transports fluid across W (which rate is proportional to the characteristic velocity of the eddy, v_s). We conclude that the shear stress created by the eddy of size s is proportional to $\rho U v_s$, or $\tau \propto \rho U v_s$. *This scaling expression for the shear stress is the sought "spectral link" between τ and the turbulent eddy velocity distribution of the phenomenological theory* (Equation 1.4). By substituting Equation 1.4, we obtain $\tau \propto \rho U^2 (s/R)^{1/3}$, which indicates that the shear stress created by a straddling eddy of size s increases if s increases. Thus the eddy that dominates the creation of shear stress on W is the largest eddy that straddles W, which is an eddy of the same size as the fluid-filled cavities (recall that $s \leq r$); this reasoning gives the final expression for the shear stress that develops on the rough wall, namely $\tau \propto \rho U^2 (r/R)^{1/3}$. From the definition of the friction factor, $f \equiv \tau/\rho U^2$, we have

$$f \propto (r/R)^{1/3}, \tag{1.7}$$

which we recognize as the Strickler empirical scaling. *The empirical exponent of Strickler,* $1/3$*, is but the exponent of the eddy velocity distribution.*

Consider now the case of a smooth wall. This corresponds formally to the limit $r/R \to 0$, which according to Equation 1.7 gives $f = 0$, a result that is at odds with the Blasius empirical scaling. To dispel this paradox, recall that r in Equation 1.7 must be construed as the size of the eddy that dominates the exchange of momentum between the turbulent flow and the fluid-filled cavities of the rough wall. But the characteristic velocity of an eddy of size zero is zero, and such an eddy, lacking in both extension and velocity, cannot effect any transfer of mass or momentum. Thus the prediction, $f = 0$.

It has been argued, however (Gioia & Bombardelli, 2001; Gioia & Chakraborty, 2006), that in the limit $r/R \to 0$ the dominant eddy should be the smallest eddy that is unaffected by viscosity—that is to say, the eddy of size η. In fact, eddies smaller than η are rapidly damped by the dissipative-range correction and are virtually impotent to act as envisioned in the derivation of Equation 1.7, with the implication that the flow must be increasingly dominated by viscosity at distances less than η from the wall. Thus, to compute f for the smooth-wall case, we must focus on the exchange of momentum across a cylindrical wetted surface at a distance η from the wall, a surface straddled by eddies of size η, the velocity of which is governed by the velocity distribution of the phenomenological theory. This we can readily accomplish by substituting η for r in Equation 1.7, with the result $f \propto (\eta/R)^{1/3}$. Taking into account the relation between η and Re, Equation 1.6, we obtain the final expression for the friction factor of smooth-walled turbulent pipe flows,

$$f \propto Re^{-1/4}, \tag{1.8}$$

which we recognize as the Blasius empirical scaling. *The empirical exponent of Blasius,* $-1/4$*, is but a recast form of the exponent of the eddy velocity distribution.*

The existence of a spectral link sheds some new theoretical light on the friction factor, with a number of practical implications. Consider, for example, the effect of polymeric additives on the friction factor of oil pipelines. These additives are known to cause a pronounced reduction in friction factor (Toms, 1948; Virk *et al.*, 1967; Lumley, 1969; Perlekar *et al.*, 2006), which is the reason why they are customarily injected in oil pipelines to lessen pumping costs (Burger *et al.*, 1980; White & Mungal, 2008).

Although there has been no lack of theories aimed at explaining the reduction of fluid friction due to polymeric additives (L'vov *et al.*, 2004; Procaccia *et al.*, 2008; White & Mungal, 2008; Yang, 2009), no theory has yet been widely accepted. What is more, none of the theories proposed so far has dwelled on the cardinal fact that polymeric additives are known to change the exponent of the eddy velocity distribution (Fouxon & Lebedev, 2003; Dubief *et al.*, 2013). Because of the spectral link, a change in that exponent will cause a change in the friction factor. Thus the spectral link may help explain the reduction of friction due to polymeric additives (Calzetta, 2010, 2012; Anbarlooei *et al.*, 2015, 2017). Rather than carrying out expensive tests to ascertain the friction factor in flows with polymeric additives (and other agents that are also known to affect both the friction factor and the eddy velocity distribution, including particulate suspensions and air bubbles (Richter, 2015; Rensen *et al.*, 2005; Prakash *et al.*, 2016)), it might be possible to predict the friction factor from simple, inexpensive measurements of the modified exponent of the eddy velocity distribution.

1.3 Outline of the thesis

We proceed chapter by chapter in the order of their appearance.

We start the next chapter (Chapter 2) with a review of the turbulent mean-velocity profile (MVP), a fundamental macroscopic property of the canonical wall-bounded turbulent flows. For the sake of concreteness, we focus at first on the MVPs of turbulent pipe flow. We review the most salient features of the MVPs of turbulent pipe flow, which are known from innumerable experiments and computational simulations, and which are basically shared in common with the MVPs of all other canonical wall-bounded turbulent flows. These most salient features including the successive “layers”—the viscous layer (adjacent to the wall), the buffer layer, the log layer, and the wake (adjacent to the centerline of the flow)—in which the domain of a MVP is conventionally partitioned. We also review the way in which, via the introduction of the classical, dimensionless “wall variables”, the MVPs corresponding to different Reynolds numbers can be made to collapse onto a single master curve in all layers except the wake.

Next in Chapter 2, we discuss the spectrum of turbulent kinetic energy, which is essentially a derivative of the eddy velocity distribution. We show that, just as was the case for the eddy velocity distribution, the spectrum consists of a power law which is valid in the inertial range and must be modified by a multiplicative dissipative-range correction, which alters the power law in the dissipative range, and a multiplicative energetic-range correction, which alters the power law in the energetic range. We also introduce the standard explicit forms of both corrections (Pope, 2000).

We then turn to a derivation of a specific form of the spectral link relating the spectrum to the local turbulent shear stress. This derivation differs from the original derivation (Gioia *et al.*, 2010) in that it is grounded on the concept of control volume, which has been deemed the quintessential development of engineering science vis-à-vis physics (Vincenti, 1982). By combining the spectral link with equations of momentum balance and energy balance, which equations are somewhat different depending on the type of wall-bounded flow, we formulate a complete spectral theory of the MVPs.

In the remaining of Chapter 2, we use the spectral theory to explain the significant disparities, evinced by the empirical data and hitherto left unexplained in the literature, between the MVPs of pipe flow and channel flow. We seek to shed theoretical light on these disparities, which are circumscribed to the wakes, and to trace their physical origin to the lack of universality of the spectrum in the energetic range.

In Chapter 3 we turn to plane Couette flow, and focus our attention on a number of well-known, and as yet unresolved, disparities in the classical experimental data on turbulent friction in plane Couette flow. We start by pointing out that those disparities are accompanied by previously unnoticed disparities in the attendant MVPs. Interestingly, the disparities in the MVPs are circumscribed to the wakes, just as was the case in Chapter 2; but the disparities of that chapter involved different types of turbulent flow (that is pipe flow and channel flow) whereas the disparities of Chapter 3 involve one and the same type of turbulent flow: plane Couette flow. By assessing the empirical data in light of the spectral theory, we argue for the existence, in plane Couette flow, of multiple states of turbulence that differ only at the largest lengthscales in the flow, corresponding to the energetic-range correction of the spectrum. Thus, the multiplicity of turbulent states, which may be a generic feature of turbulent flows with moving boundaries (and, as it has been argued by Huisman *et al.* (2014), may be at odds with the phenomenological theory), is in fact perfectly consistent with small-scale universality (Kolmogórov, 1941*b*; Schumacher *et al.*, 2014).

In Chapter 4 we turn to thermally-stratified turbulent flows in the atmospheric boundary layer, the approximately 1 km thick region enveloping the surface of the Earth, which may be modeled as a thermally-stratified plane Couette flow. The theoretical framework for the MVP in such a flow is furnished by the Monin-Obukhov similarity theory (MOST) (Obukhov, 1946; Monin & Obukhov, 1954), which focuses on an intermediate region of the MVPs—not too close to the wall, where viscosity affects the flow, and not too far from the wall, where external confinement affects the flow. By suitably extending the spectral theory to account for the thermal stratification, we show that it is possible to account for the whole extent of the MVPs. Further, by invoking tools of dimensional analysis and complete similarity, we derive a set of scaling laws for the MVPs (and their derivatives) that includes not only the intermediate region, but also the region near the wall and the region far from the wall. Our analysis leads to a generalized MOST.

Finally, in Chapter 5 we conclude the thesis with a recapitulation of our findings and a discussion of implications and prospects for future research.

Chapter 2

Spectral theory of wall-bounded turbulent flows

In this chapter, we will derive a spectral theory of the turbulent mean-velocity profiles (MVPs) applicable to three types of wall-bounded flow: pipe flow, channel flow, and plane Couette flow (Pope, 2000; Kundu & Cohen, 2002). Pipe flow and channel flow are pressure driven whilst plane Couette flow is driven by the walls. A single cylindrical wall of radius R surrounds the domain of pipe flow. In channel flow and plane Couette flow, the domain of the flow is sandwiched between two planar walls separated by a gap of constant width (customarily denoted by $2h$ in the case of channel flow, $2b$ in the case of plane Couette flow). In plane Couette flow, one of the walls moves relative to the other at a constant velocity, and we will always consider the frame of reference in which the lower wall is stationary.

We start with a discussion of the turbulent MVPs.

2.1 Turbulent mean-velocity profiles

For the sake of concreteness, we focus on pipe flow, which is, of the three types of flow of interest here, the one that appears to have been researched the most, particularly in the turbulent regime. Consider the turbulent flow in a long cylindrical pipe with a smooth internal wall. Suppose that the volume flux is kept steady and the flow is fully developed, by which we mean that the statistics of the fluid velocities may be considered invariant in the streamwise direction. In that case, at a distance y from the wall of the pipe, a local mean velocity u can be obtained by averaging the instantaneous velocity of the flow over a long period of time. The function $u(y)$ is known as the mean-velocity profile (MVP) of the flow. For each value of the Reynolds number Re, there is a MVP. The Reynolds number quantifies the relative importance of inertia and viscosity in the flow. For pipe flow, $\mathrm{Re} \equiv RU/\nu$, where U is the mean velocity of the flow (that is, the volume flux divided by the cross-sectional area of the pipe) and ν is the kinematic viscosity of the fluid.

MVPs in pipe flows were first measured experimentally more than 80 years ago (Nikuradse, 1950) and have recently been the subject of numerous experiments (Zagarola & Smits, 1998; Mckeon *et al.*, 2004; Hultmark *et al.*, 2012, 2013; Furuichi *et al.*,

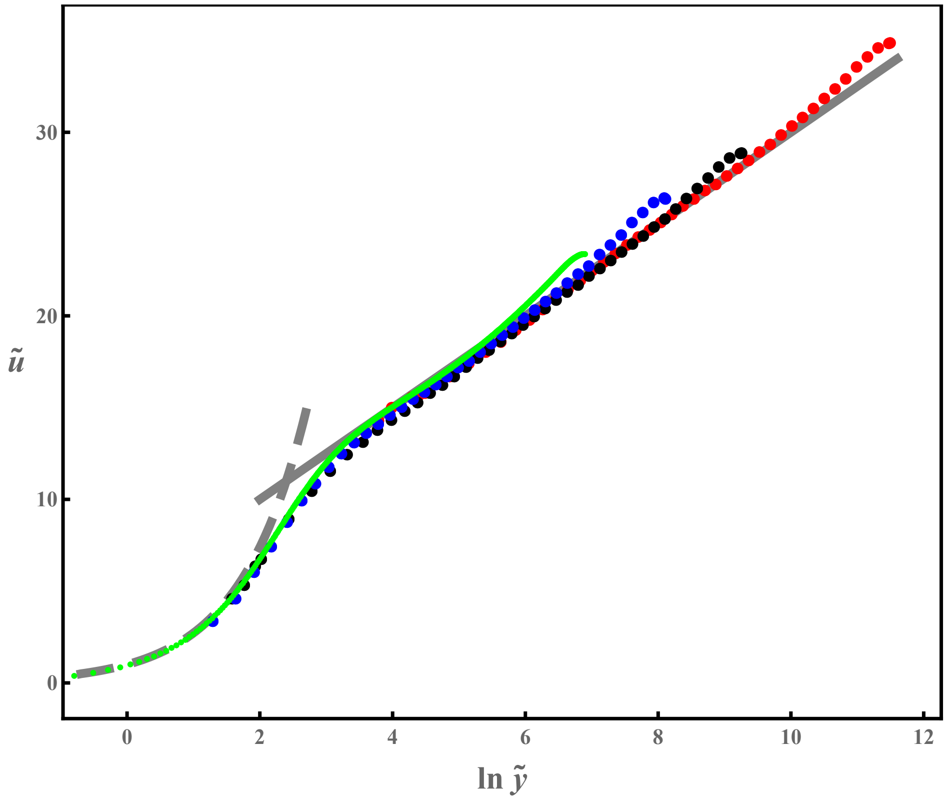

Fig. 2.1: Log-linear plots of the MVPs of pipe flow in the wall variables $\tilde{u}$ and $\tilde{y}$ for four values of Re (Re_τ). The green symbols denote the data from direct numerical simulations (DNS) (El Khoury *et al.*, 2013) with $\mathrm{Re}_\tau = 999$ and the blue, black, and red symbols denote the data from experiments (Hultmark *et al.*, 2012, 2013) with $\mathrm{Re}_\tau = 3334, 10480$, and 98190, respectively. The grey line denotes the log law, $\tilde{u}(\tilde{y}) = \frac{1}{\kappa}\ln\tilde{y} + B$, with $\kappa = 0.4$ and $B = 5$. The dashed grey line denotes the laminar solution of the viscous layer, $\tilde{u}(\tilde{y}) = \tilde{y}$. Each MVP extends from the wall (which corresponds always to $\tilde{y} = 0$) to the centerline of the pipe (which corresponds to $\tilde{y} = \mathrm{Re}_\tau$); the MVPs collapse onto a single curve close to the wall.

2015) and numerical simulations (Eggels *et al.*, 1994; Wu & Moin, 2008; El Khoury *et al.*, 2013). Ludwig Prandtl argued that the MVPs should be plotted in terms of the dimensionless "wall variables" $\tilde{u}$ and $\tilde{y}$, in which case the MVPs for different values of Re would collapse onto a single curve close to the wall (Prandtl, 1953), as can be verified in Fig. 2.1, in which we have plotted a few typical MVPs of turbulent pipe flows from various experiments and numerical simulations. The wall variables are defined as $\tilde{u} \equiv u/u_\tau$ and $\tilde{y} \equiv yu_\tau/\nu$, where $u_\tau \equiv \sqrt{\tau_0/\rho}$, ρ is the density of the fluid, and τ_0 is the total shear stress at the wall of the pipe. (The dimensionless form of τ_0, $\tau_0/\rho U^2$, is termed the friction factor, $f \equiv \tau_0/\rho U^2$, and quantifies the fluid friction at the wall.) At the centerline of the pipe $\tilde{y} = \mathrm{Re}_\tau \equiv Ru_\tau/\nu$. From Fig. 2.1, it is apparent that to each MVP there corresponds a different value of Re_τ, just as to each MVP there corresponds a different value of Re. It follows that there is a one-to-one correspondence between Re and Re_τ, and, therefore, that Re_τ, which is known as the friction Reynolds number, may be deemed an alternative form of the Reynolds number (as its name indicates).

By turning our attention on any one MVP in Fig. 2.1 and scanning that MVP from left to right, in the direction of increasing $\tilde{y}$, we can distinguish a number of conventionally named "layers": the viscous layer (where the MVP has a positive curvature), the buffer layer (where the MVP has a noticeable negative curvature), the log layer (where $\tilde{u}$ varies linearly with $\ln \tilde{y}$), and the wake (where the MVP deviates from the linear $\tilde{u}$–$\ln \tilde{y}$ relation of the log layer, close to the centerline of the pipe). These layers can be identified in the turbulent MVPs of all types of wall-bounded turbulent flow, not just pipe flow.

In the log layer, the relation between $\tilde{u}$ and $\tilde{y}$ can be written in the form

$$\tilde{u}(\tilde{y}) = \frac{1}{\kappa} \ln \tilde{y} + B, \tag{2.1}$$

which is known as the "log law". Here, κ (the "Kármán constant") and B are dimensionless constants which can be estimated by fitting experimental data (Prandtl, 1953). Although the log law was justified by Prandtl on the basis of dimensional analysis and suitable assumptions of similarity, κ and B remained empirical constants. Indeed, for many decades, theoretical research on the MVPs of pipe flows, as well as of other wall-bounded turbulent flows, evinced limited progress beyond Prandtl's work. Here, we seek to formulate a spectral theory of the MVPs, that is, a theory of the MVPs grounded on the existence of a connection between the MVPs and the spectrum of turbulent kinetic energy, to which we turn next.

2.2 The spectrum of turbulent kinetic energy

The spectrum of turbulent kinetic energy, $E(k)$, or the spectrum for short, is a function of the wavenumber k, defined by the expression $E(k) \equiv dv_k^2/dk$, where v_k is the characteristic velocity of a turbulent eddy of wavenumber k. Note that $k \propto 1/s$, where s is the size of the eddy; thus the eddy velocity distribution of the phenomenological theory, discussed in some detail in the introductory chapter (Chapter 1), is but a derivative of the spectrum. Indeed, the velocity of an eddy of size s, v_s, can be computed as

$$v_s = \sqrt{\int_{1/s}^{\infty} E(k)dk}, \tag{2.2}$$

where

$$E(k) = \frac{2}{3}(\kappa_\varepsilon \varepsilon)^{2/3} k^{-5/3} \exp(-\beta_d \eta k)(1 + (\beta_e/Lk)^2)^{-17/6}. \tag{2.3}$$

This expression for $E(k)$ corresponds to the standard model of the spectrum (Pope, 2000). It consists of (see Fig. 2.2)

1. the power-law spectrum of Kolmogórov, $\frac{2}{3}(\kappa_\varepsilon \varepsilon)^{2/3} k^{-5/3}$, valid in the inertial range, where κ_ε is a dimensionless, non-negative constant which can be theoretically estimated as $\frac{4}{5}$ (Gioia *et al.*, 2010; Gioia & Chakraborty, 2006), ε is the turbulent power per unit mass (that is, the characteristic invariant of the energy cascade), and $-5/3$ is the spectral exponent.

2. The dissipative-range correction that accounts for the effect of viscosity at high wavenumber (small eddies), $\exp(-\beta_d \eta k)$, where β_d is a dimensionless, non-negative constant known as the dissipative-range parameter, and η is the viscous length-scale, $\eta = \nu^{3/4}\varepsilon^{-1/4}$.

3. The energetic-range correction that accounts for effect of finite domain at low wavenumber (large eddies), $(1 + (\beta_e/Lk)^2)^{-17/6}$, due to Kármán, where β_e is a dimensionless, non-negative constant known as the energetic-range parameter, and L is the size of the largest eddy. For pipe flow, we take L to be equal to R, the pipe radius, or $L = R$. For channel flow and for plane Couette flow, we set $L = h$ and $L = b$, respectively, where h and b denote half the distance between the walls in channel flow and in plane Couette flow, respectively.

The standard model of the spectrum has been tested successfully by comparison with extensive measurements of the velocity fluctuations carried out over a wide range of Reynolds numbers, and by a variety of probing techniques, in laboratory flows, atmospheric flows, flows with shear and flows without shear, as well as by comparison with velocity fluctuations computed in numerical simulations (Pope, 2000). In spite of its relative simplicity, the standard model provides a comprehensive, quantitative and physically meaningful account of each of the features of the spectrum evinced by the empirical data.

For future reference, note that $E(k) > 0$ for all k. Thus, from $v_s = \sqrt{\int_{1/s}^{\infty} E(k)dk}$, we conclude that v_s is a monotonically increasing function of s. In other words, the larger the eddy, the larger its characteristic velocity.

By substituting the standard model of the spectrum (Equation 2.3) in Equation 2.2, we obtain (Gioia *et al.*, 2010)

$$v_s = (\kappa_\varepsilon \varepsilon s)^{1/3}\sqrt{I}, \tag{2.4}$$

where

$$I \equiv I(\eta/s, s/L) \equiv \frac{2}{3}\int_1^{\infty} \xi^{-5/3}\exp(-\xi\beta_d\eta/s)(1 + (\beta_e s/L)^2/\xi^2)^{-17/6}d\xi \tag{2.5}$$

and $\xi \equiv sk$. In general, for an eddy of size s in the inertial range ($\eta \ll s \ll L$), $I = 1$ and $v_s = (\kappa_\varepsilon \varepsilon s)^{1/3}$, which is the eddy velocity distribution in the inertial range (discussed in the introductory chapter). For an eddy size s in the dissipative range ($s \lesssim \eta$) or the energetic range ($s \gtrsim L$), $I < 1$ and $v_s < (\kappa_\varepsilon \varepsilon s)^{1/3}$, with the implication that the eddy is *slower* than an imaginary eddy of the same size in the inertial range. If we set $\beta_d = \beta_e = 0$—that is, if there were no dissipative-range correction and no energetic-range correction (an unphysical proposition)—$v_s = (\kappa_\varepsilon \varepsilon s)^{1/3}$ for all s, and all eddies would be inertial.

2.3 Turbulent shear stress and spectral link

We seek to derive an expression for the turbulent shear stress that acts on a wetted surface W_y at a distance y from the wall (Fig. 2.3). Consider a cuboidal control volume

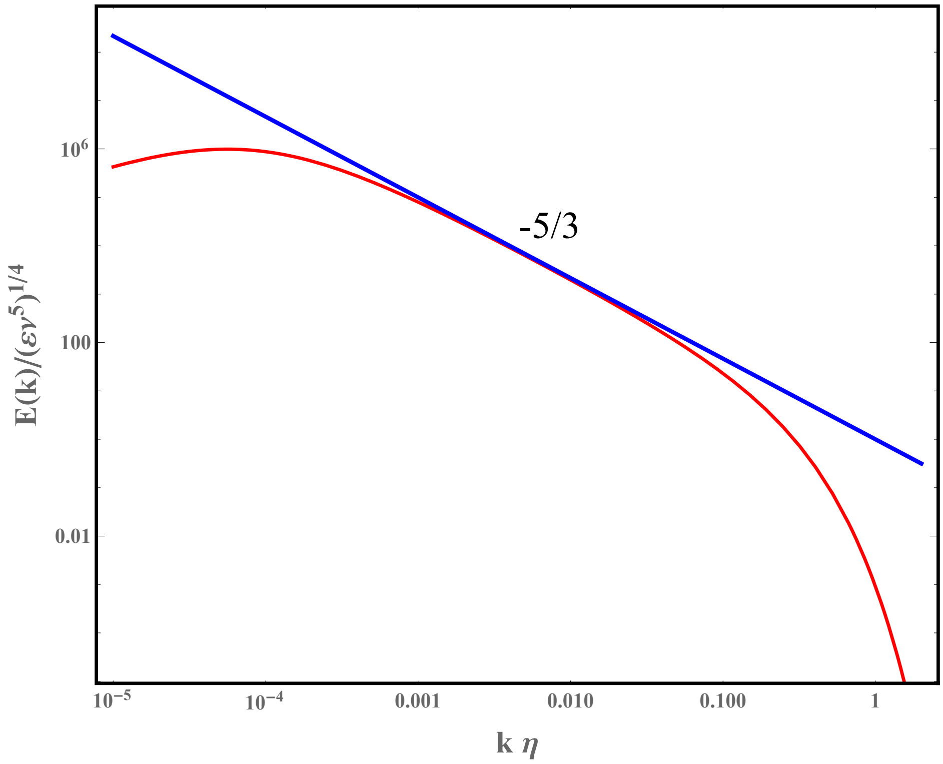

Fig. 2.2: Red line: model spectrum for $\beta_d = 7$, $\beta_e = 8$, and $L/\eta = 10^5$. Blue line: Kolmogórov spectrum without corrections.

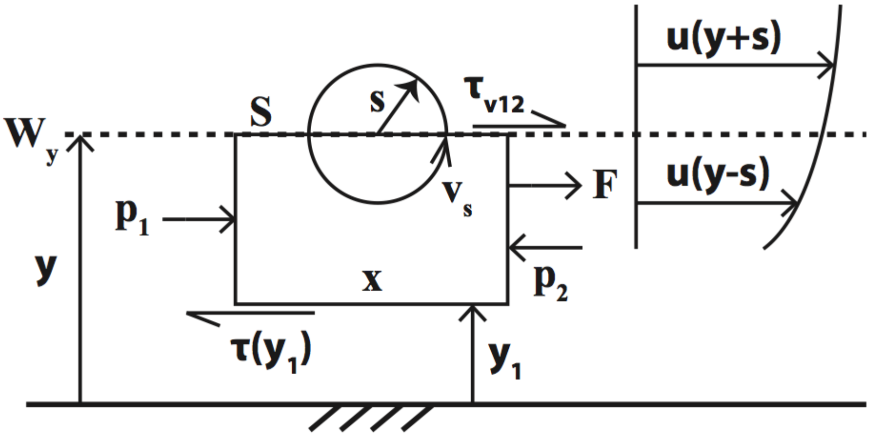

Fig. 2.3: Schematic used to derive an expression for the turbulent shear stress on the wetted surface W_y. For the coordinate axes, we choose the x axis to be along the streamwise direction and the y axis to be along the wall-normal direction. Note that $y = 0$ corresponds to the wall, so that W_y is at a distance y from the wall.

(CV) whose upper face (of surface area S) overlaps with W_y and whose lower face is at a distance y_1 from the wall. The length of the CV is X. (y_1 and X are arbitrary and $0 < y_1 < y$.) Eddies of size s (and velocity v_s) bring high-momentum fluid (momentum per unit mass $\sim \rho u(y + s)$) into the CV and take low-momentum fluid (momentum per unit mass $\sim \rho u(y - s)$) out of the CV. The net momentum exchanged in a time interval Δt is

$$\Delta M \sim S v_s \Delta t\, \rho u(y+s) - S v_s \Delta t\, \rho u(y-s) \approx 2S\rho v_s \Delta t s \frac{du(y)}{dy}, \tag{2.6}$$

Thus, there is an turbulent force F acting on the CV:

$$F = \Delta M/\Delta t \sim 2\rho S v_s s \frac{du(y)}{dy}. \tag{2.7}$$

Then the turbulent shear stress τ_{t12} must be the same as this turbulent force per unit area, i.e.,

$$\tau_{t12} = F/S \sim \rho s v_s \frac{du(y)}{dy}, \tag{2.8}$$

which generally applies to all the types of wall-bounded turbulent flow with which we shall be concerned. For fully developed turbulent pipe flow, channel flow and plane Couette flow, we show that this expression of turbulent shear stress can be obtained via force equilibrium equation. The force equilibrium equation for the CV reads

$$(p_1 - p_2)(y - y_1)S/X + F + \tau_{v12} S = \tau(y_1)S, \tag{2.9}$$

where $p_1 - p_2$ is the pressure drop over the length X of the CV and τ_{v12} is the viscous shear stress on the upper face of the CV, $\tau_{v12} = \rho\nu \frac{du(y)}{dy}$. From Equation A.10 of Appendix A we have $\tau(y) = \frac{dp_0}{dx_1}(y - y_1) + \tau(y_1)$, and with $p_1 - p_2 = -\frac{dp_0}{dx_1}X$, we obtain

$$F/S + \tau_{v12} = \tau(y), \tag{2.10}$$

Therefore, the turbulent shear stress τ_{t12} should be expressed as

$$\tau_{t12} = \tau(y) - \tau_{v12} = F/S \sim \rho s v_s \frac{du(y)}{dy}, \tag{2.11}$$

which is the same as Equation 2.8. (Thus, the turbulent viscosity ν_t scales as $\nu_t \sim s v_s$; see Appendix A.) Note that we have allowed for a non-zero pressure gradient; it follows that Equation 2.11 applies to turbulent flows with pressure gradient (such as pipe flow and channel flow) as well as turbulent flows with no pressure gradient (such as plane Couette flow).

Now, we have seen that v_s is a monotonically increasing function of s. Thus, τ_{t12} is also a monotonically increasing function of s, and the production of turbulent shear stress must be dominated by the largest eddies that straddle W_y—that is, the eddies of size $s = y$. We conclude that

$$\tau_{t12} = \kappa_\tau \rho y v_y \frac{du(y)}{dy}, \tag{2.12}$$

where κ_τ is a dimensionless parameter (a proportionality constant). Next, we set $s = y$ in Equation 2.4 to obtain, $v_y = (\kappa_\varepsilon \varepsilon y)^{1/3}\sqrt{I}$, where $\varepsilon = \tau_{t12}\frac{du(y)}{dy}/\rho$ is the energy equation (or, more precisely, the turbulent kinetic energy budget equation, for which see Appendix B); substituting in Equation 2.12:

$$\tau_{t12} = \kappa^2 \rho I^{3/4} y^2 (\frac{du(y)}{dy})^2, \tag{2.13}$$

where $\kappa \equiv (\kappa_\varepsilon \kappa_\tau^3)^{1/4}$ and $I \equiv I(\eta/y, y/L)$.

Equation 2.12 links the turbulent shear stress to v_y, the eddy velocity distribution, which is a function the spectrum. In other words, Equation 2.12 is the "spectral link". It was first derived, by a method different from that which we have employed here, by Gioia *et al.* (2010), who showed that the parameter κ in Equation 2.13 is but the Kármán constant of the log law, which according to the theory can be expressed as $\kappa \equiv (\kappa_\varepsilon \kappa_\tau^3)^{1/4}$. Thus, the Kármán constant is set by κ_τ and κ_ε, which relate to the mechanism of momentum transfer and to the spectrum, respectively. The fact that the Kármán constant depends explicitly on a spectral parameter, namely κ_ε, serves as a striking reminder of the fundamental *spectral* nature of the present theory.

2.4 Equations of the MVPs

The total shear stress of the types of flow with which we are concerned can be expressed in the form

$$\tau(y) = \tau_{v12} + \tau_{t12} = \tau_0 \sigma, \tag{2.14}$$

where $\sigma = 1 - y/R$ for pipe flow, $\sigma = 1 - y/h$ for channel flow, and $\sigma = 1$ for plane Couette flow (see Appendix A). By substituting the total shear stress in Equation 2.13 and rewriting the result in terms of the friction Reynolds number ($\mathrm{Re}_\tau \equiv L u_\tau/\nu$) and the wall variables ($\tilde{y} \equiv \mathrm{Re}_\tau y/L$ and $\tilde{u} \equiv u/u_\tau$), we obtain the momentum equation:

$$\kappa^2 I^{3/4} \tilde{y}^2 (\frac{d\tilde{u}}{d\tilde{y}})^2 + \frac{d\tilde{u}}{d\tilde{y}} = \sigma, \tag{2.15}$$

where $I \equiv I(\eta/y, \tilde{y}/\mathrm{Re}_\tau)$.

Similarly, by taking into account that $\eta = \nu^{3/4}\varepsilon^{-1/4}$ and $\varepsilon = \tau_{t12}\frac{du(y)}{dy}/\rho$ (the energy equation), we obtain a recast (and final) form of the energy equation:

$$\eta/y = (\frac{d\tilde{u}}{d\tilde{y}}\sigma - (\frac{d\tilde{u}}{d\tilde{y}})^2)^{-1/4} \tilde{y}^{-1}, \tag{2.16}$$

which is coupled to the momentum equation via the dependence of I on η/y. Equations 2.15 and 2.16 are the equations of the MVPs in the spectral theory.

When the flow is laminar, the turbulent shear stress is naught ($\tau_{t12} = 0$) and Equation 2.15 reduces to $\frac{d\tilde{u}}{d\tilde{y}} = \sigma$, which is the law of laminar flows (Kundu & Cohen, 2002). When the flow is turbulent, the no-slip boundary condition gives rise to a thin laminar viscous layer next to the wall ($y \ll L$). Now, for $y \ll L$, σ reduces to 1 regardless of the type of flow; thus, with the no-slip boundary condition (that is, $\tilde{u} = 0$ for $\tilde{y} = 0$), the viscous layer solution for all the cases discussed here reads $\tilde{u} = \tilde{y}$. We shall show next that the thickness of the viscous layer can be determined starting with Equations 2.15 and 2.16.

Consider a point where $y \ll L$, $\tau_{t12} > 0$, thus $\sigma = 1$, $I = I(\eta/y, 0) > 0$. Then $\frac{d\tilde{u}}{d\tilde{y}}$ can be eliminated from Equations 2.15 and 2.16 to obtain,

$$\tilde{y} = \left(\frac{(\eta/y)^{4/3} + \kappa^{4/3} I^{1/2}(\eta/y, 0)}{\kappa^{2/3} (\eta/y)^{8/3} I^{1/4}(\eta/y, 0)} \right)^{1/2}. \tag{2.17}$$

Now, for a given value of κ and a given value of β_d, Equation 2.17 gives $\tilde{y}$ as a function of η/y. As it turns out, this function has a minimum, denoted $\tilde{y}_v$ (Fig. 2.4), with the implication that for $\tilde{y} < \tilde{y}_v$ there is no turbulent solution (Gioia *et al.*, 2010). Thus, for $\tilde{y} < \tilde{y}_v$ the only possible solution is the viscous layer solution, $\tilde{u} = \tilde{y}$, and $\tilde{y}_v$ represents the thickness of the viscous layer. For $\kappa = 0.4$ and $\beta_d = 7$, the viscous layer thickness $\tilde{y}_v = 4.24$ (Fig. 2.4). For $\tilde{y} > \tilde{y}_v$, turbulence prevails and the turbulent MVP can be computed by integrating Equation 2.15 with boundary condition $\tilde{u} = \tilde{y}_v$ at $\tilde{y} = \tilde{y}_v$. Note that the MVP is determined by all three parameters (κ, β_d and β_e) whereas the thickness of the viscous layer depends only on κ and β_d.

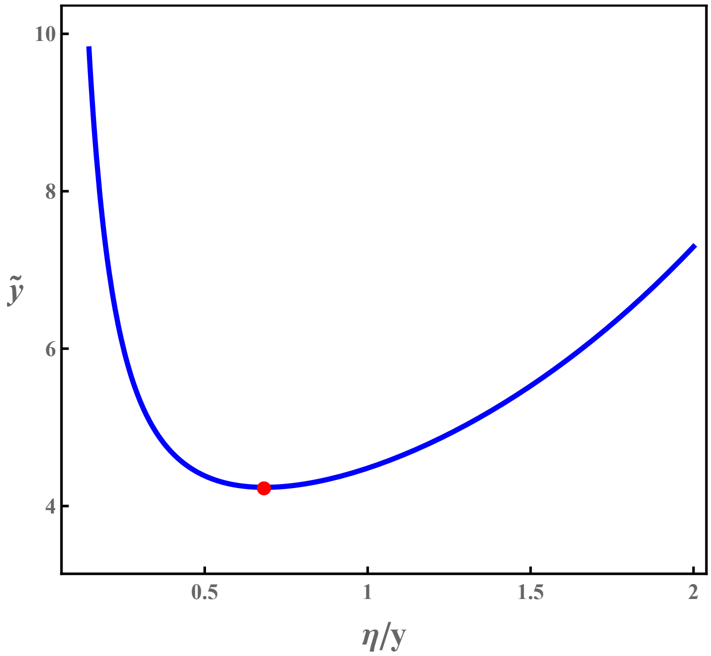

Fig. 2.4: Plot of $\tilde{y}$ vs. η/y as per Equation 2.17, for $\kappa = 0.4$ and $\beta_d = 7$. The thick red dot indicates the point where $\tilde{y}$ is minimized; the minimum is denoted by $\tilde{y}_v$ and represents the thickness of the viscous layer.

From the equations of the spectral theory, it is apparent that the standard model of the spectrum should in itself be sufficient to compute, with no additional assumptions, the turbulent MVP corresponding to any given Reynolds number, over its entire domain, regardless of the type of flow (pipe flow, channel flow, or plane Couette flow). For pipe flow, it has been shown that, indeed, the theory yields complete MVPs with viscous layer, buffer layer, log layer, and wake (Gioia *et al.*, 2010). Furthermore, *each part of the MVP relates to a specific spectral range*: the viscous layer to the dissipative range, the buffer layer to the dissipative range, the log layer to the inertial range, and the wake to the energetic range.

Regarding the viscous layer, we have seen already that it relates to the dissipative range in that its thickness is set by the dissipative-range parameter β_d. As for the log layer, we have seen that in the spectral theory the Kármán constant (that is, the characteristic constant of the log law) is independent of both β_d and the parameter of the energetic-range correction, β_e. This indicates that the eddies that dominate momentum transfer in the log layer are affected by neither β_d nor β_e—that is, they are eddies of the inertial range. Thus, the log layer relates to the inertial range.

The buffer layer and the wake are perhaps the most interesting. Regarding the buffer layer, it has been shown that the eddies that dominate momentum transfer in the buffer layer are eddies of the dissipative range (Gioia *et al.*, 2010). As such, these eddies are slowed down by the dissipative-range correction, which makes them less effective at transferring momentum and producing turbulent shear stress. Thus, the turbulent shear stress lessens and, consequently, the mean velocity increases locally in the buffer layer. This local increase in mean velocity results in a steepening of the MVP—that is, the signature characteristic of the MVP in the buffer layer. Similarly, it turns out that the eddies that dominate momentum transfer in the wake are eddies of the energetic range. As such, these eddies are slowed down by the energetic-range correction—ultimately resulting in a steepening of the MVP, which overshoots the log layer. This is the signature characteristic of the MVP in the wake.

The previous paragraph can be summarized as follows. The amplitude of the buffer layer and the amplitude of the wake are set by the spectral parameters β_d and β_e, respectively.

The one-to-one correspondence between the layers of the MVPs and the ranges of the spectrum plays a crucial role in our analysis of plane Couette flow (Chapter 3) as well as in the remaining portion of the present chapter, starting in Section 2.6. Before turning to that section, however, we discuss a few methodological issues related to the application of the spectral theory in the present thesis.

2.5 A note on the application of the spectral theory in this thesis

We intend to use the spectral theory to extract insight into the MVPs of various turbulent flows out of the spectrum, on which much has been revealed by the phenomenological theory of turbulence. Thus the emphasis will be on that which the spectrum may tell us about the structure of the MVPs rather than on how accurately the spectral theory can reproduce, on the basis of the standard model of the spectrum, plots of the empirical data on the MVPs. These considerations pertain to all of the research expounded in the present thesis, and merit some development.

We have seen that the spectral theory entails the existence of individual links, discussed in the preceding section, between each range of the spectrum and a specific layer of the MVP. In connection with these individual spectral links, we will be chiefly interested in broadly qualitative, rather than quantitative, aspects of the spectrum and the MVP. Thus regarding the spectral link between the energetic range of the spectrum and the wake of the MVP, for example, our interest will be on qualitative, or generic, aspects of the energetic-range correction and their relation to salient characteristics of the wake, notably the relation between the generic fact that the energetic-range correction decays for small k (in contrast to the specific fact that, according to the standard model of the spectrum, the decay follows the power law put forth by Kármán) and the concomitant fact that the MVP overshoots the log law in the wake. Similarly, we will dwell on the decaying nature of the dissipative-range correction at large k, a generic fact that results, via the spectral theory, in a buffer layer that with the correct (negative) curvature evinced by the empirical data.

Keeping this outlook in mind, we will not try to fit the MVPs from the spectral theory (computed using the standard model) to the empirical MVPs. Instead we will show the computed MVPs and the empirical ones in separate yet readily-comparable plots, and focus on the capacity of the spectral theory to reproduce all of the salient features of the empirical MVPs, allowing us to trace the cause of each one of those salient features to the corresponding feature of the spectrum. Note, however, that the dissipative-range and energetic-range parameters, β_d and β_e, will in all cases be set to values in the narrow range 5–7 (for β_d) and 1–9 (for β_e), consistent with both theoretical considerations (whereby both β_d and β_e are expected to be of order 1) and the available empirical data on the spectrum (Pope, 2000).

2.6 Comparison between pipe flow and channel flow

2.6.1 Disparities of MVP

In this section, we carry out an analysis of the well-known disparities, evinced by the empirical data and hitherto left unexplained in the literature, between the MVPs of pipe flow and channel flow. By putting to use the spectral theory, we seek to trace the physical origin of these disparities (and of the less well-known disparities in other macroscopic properties besides the MVPs) to the lack of universality of the spectrum in the energetic range.

Fig. 2.5 shows typical examples of the empirical data for $\mathrm{Re}_\tau \simeq 1000$. At this juncture we find it convenient to include plane Couette flow alongside pipe flow and channel flow, even though our focus here will be on the comparison between pipe flow and channel flow. (The case of plane Couette flow is more involved than Fig. 2.5 would suggest, and will be treated in detail in Chapter 3.)

Like the MVPs of pipe flow, the MVPs of channel flow and plane Couette flow consist of a viscous layer, a buffer layer, a log layer, and a wake. What is more, the MVP of pipe flow is practically indistinguishable from the MVP of channel flow and the MVP of plane Couette flow except in the wake. In other words, the MVPs for the three types of flow may be said to collapse onto a single master curve except for the wake, the amplitude of which differs depending on the type of flow.

Now, we have seen that in the spectral theory, of all the characteristic features of the MVPs, only the wake relates to the energetic range of the spectrum—and, indeed, the energetic-range parameter β_e is responsible for setting the amplitude of the wake. Furthermore, according to the phenomenological theory, the energetic range is the only part of the spectrum that is not universal and might vary from one type of flow to another (Kolmogórov, 1941*b*; Schumacher *et al.*, 2014). Thus, the fact that the MVPs of Fig. 2.5 collapse onto a single master curve in the viscous layer, the buffer layer, and the log layer can be explained, in light of the spectral theory, as a macroscopic manifestation of the universal character of the spectrum at small lengthscales, including the dissipative range and the inertial range. Conversely, the fact that there are discrepancies in the wakes depending on the type of flow can also be explained, in

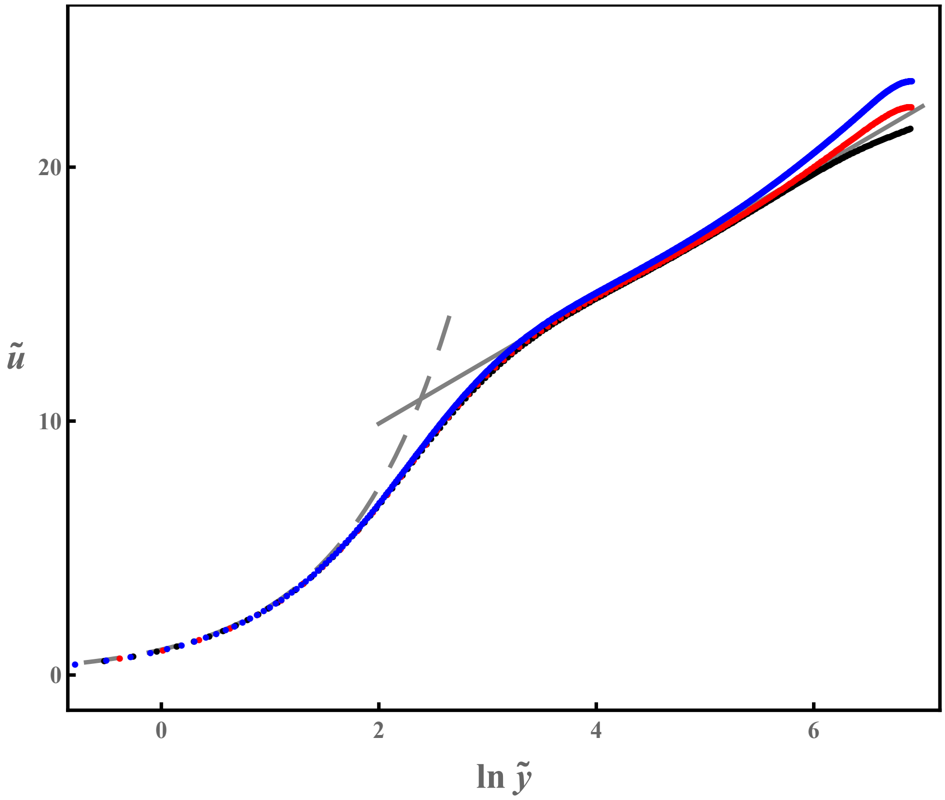

Fig. 2.5: Log-linear plots of typical MVPs of pipe flow (blue), channel flow (red) and plane Couette flow (black) in the "wall variables" $\tilde{u}$ and $\tilde{y}$ and for $\mathrm{Re}_\tau \simeq 1000$. The thin grey line denotes the log law, $\tilde{u}(\tilde{y}) = \frac{1}{\kappa} \ln \tilde{y} + B$ with $\kappa = 0.4$ and $B = 5$. The dashed grey line denotes the laminar solution of the viscous layer, $\tilde{u}(\tilde{y}) = \tilde{y}$. Each MVP extends to $\tilde{y} = \mathrm{Re}_\tau$, which corresponds to the centerline (or centerplane) of the flow. The data are from high fidelity direct numerical simulations (DNS): El Khoury *et al.* (2013) (pipe flow), Bernardini *et al.* (2014) (channel flow), Pirozzoli *et al.* (2014) (plane Couette flow).

light of the spectral theory, as a macroscopic manifestation of the lack of universality of the spectrum at lengthscales commensurate with the size of the turbulent domain (that is, in the energetic range), a lack of universality that can be readily accounted for by setting different values of β_e, depending on the type of flow.

We now turn to pipe flow and channel flow. Fig. 2.6 shows once again the corresponding MVPs. We can see that the amplitude of the wake is larger for pipe flow than for channel flow, with the implication that the value of β_e should be larger for pipe flow than for channel flow (Zuniga Zamalloa, 2012). This implication may be verified in Fig. 2.7, which shows that the MVPs computed using the spectral theory with larger value of β_e for pipe flow than for channel flow, are consistent feature-by-feature with the MVPs of Fig. 2.6.

The only obvious difference between pipe flow and channel flow is the geometry of the boundary: pipe flow is confined in a pipe of circular cross section while channel flow is confined in a channel of rectangular cross section. The eddies in the energetic range, and only them, being of size commensurate to the characteristic size of the

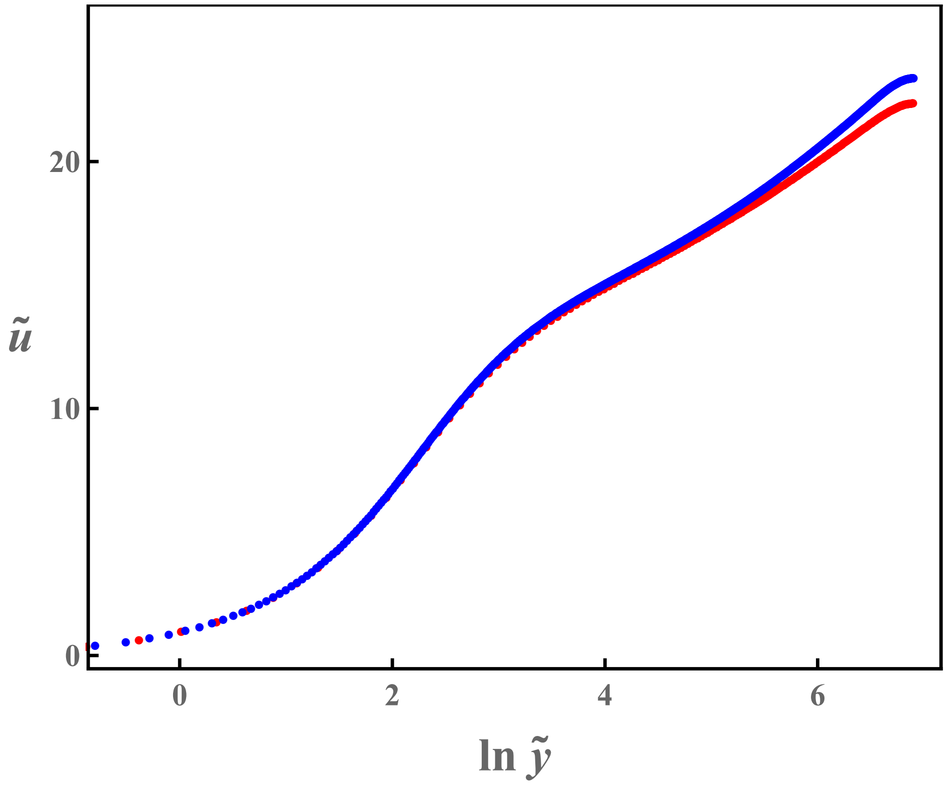

Fig. 2.6: Log-linear plots of the MVPs of pipe flow (blue) and channel flow (red) at the same value of $\text{Re}_\tau = 1000$. The data are from DNS: El Khoury *et al.* (2013) (pipe flow), Bernardini *et al.* (2014) (channel flow).

turbulent domain (R for pipe flow and h for channel flow), will be affected by the geometry of the boundaries via the energetic-range correction. Recalling an heuristic argument we discussed in the introductory chapter, those eddies might be thought of, intuitively, as being encumbered by the presence of boundaries, with the implication that their characteristic velocities are lessened, as per the energetic-range correction, as compared with those of imaginary eddies of the same size in an infinite turbulent domain. In the same line of argument, and since, given a pipe and a channel of equal characteristic size ($R = h$), the cross section of the pipe can be inscribed in the cross section of the channel, it is conceivable that the eddies of the energetic range will be encumbered to a larger degree in the pipe than in the channel, and, therefore, that β_e should be larger for pipe flow than for channel flow, with the implication that (as per the spectral theory) the amplitude of the wake should be concomitantly larger in pipe flow than in channel flow.

In a discussion of this matter, Chin *et al.* (2014) conjectured that “the discrepancy in the wake between pipe flow and channel flow would likely be due to difference in flow structures in the core region.” In light of the spectral theory, we submit that this “difference in flow structures in the core region” should be interpreted as differences in the large-lengthscale part of turbulence that corresponds to the energetic range and reflects disparities in the geometry of the boundaries. It bears emphasis that these spectral differences are circumscribed to the energetic range, with the implication

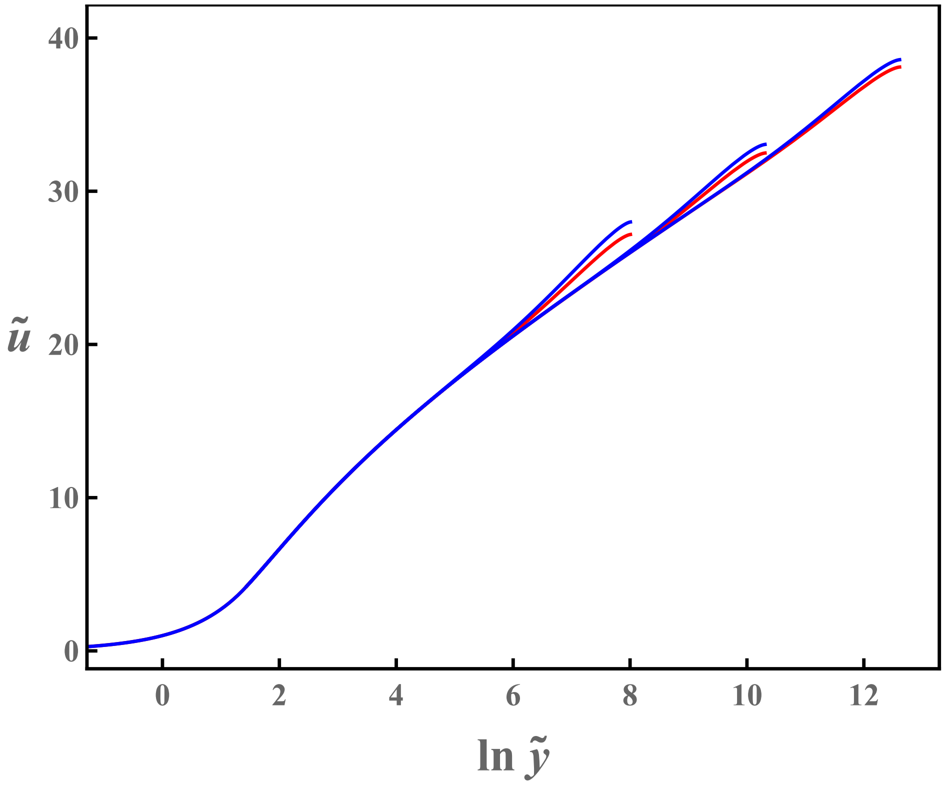

Fig. 2.7: Log-linear plots of the MVPs of pipe flow (blue) and channel flow (red) at the same value of $\mathrm{Re}_\tau = 3000, 30000, 300000$ computed from the spectral theory with $\kappa = 0.4, \beta_d = 7$; and $\beta_e = 9$ for pipe flow, $\beta_e = 7$ for channel flow.

that the attendant wake disparities remain consistent with small-scale universality as conceived in the phenomenological theory.

To find further support for our conclusions regarding the macroscopic effects of the non-universal part of the spectrum on pipe flow and channel flow, we turn our attention to macroscopic properties other than the MVPs.

2.6.2 Disparities of friction factor

The quantity most closely related to the MVP is probably the friction factor f, $f \equiv \tau_0/\rho U^2$, where U is the mean velocity of the flow. For pipe flow,

$$U = \frac{1}{\pi R^2}\int_0^R u2\pi(R-y)dy, \tag{2.18}$$

and for channel flow,

$$U = \frac{1}{h}\int_0^h udy. \tag{2.19}$$

The friction factor is usually plotted as a function of the Reynolds number, $\mathrm{Re} \equiv UR/\nu$ for pipe flow and $\mathrm{Re} \equiv Uh/\nu$ for channel flow. Fig. 2.8 shows that the friction factor of pipe flow is consistently higher than that of channel flow as the Re increases. Note that we can be express $f \equiv (\mathrm{Re}/\mathrm{Re}_\tau)^2$, which allows us to compute f directly from

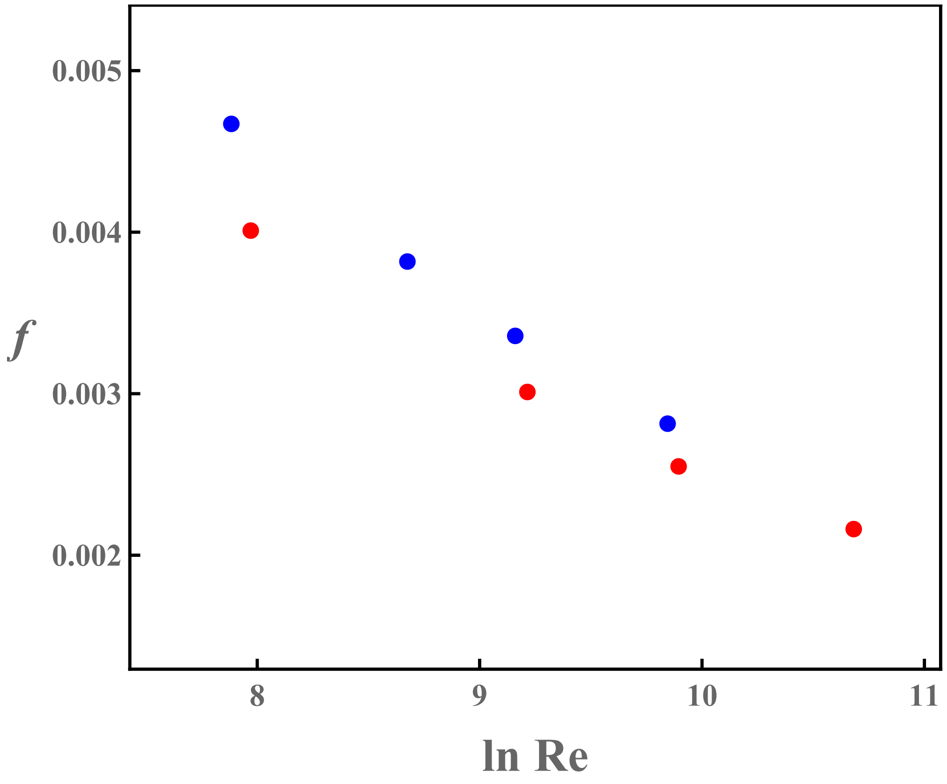

Fig. 2.8: Log-linear plots of the friction factor of pipe flow (blue) and channel flow (red) as a function of Re. The data are from DNS: El Khoury *et al.* (2013) (pipe flow), Bernardini *et al.* (2014) (channel flow).

the MVP for any given Reynolds number. By substituting $\tilde{u}$ and $\tilde{y}$ into Equations 2.18 and 2.19 and reorganizing the equations, an expression for the Reynolds number can be obtained. For pipe flow,

$$\mathrm{Re} = 2\int_0^{\mathrm{Re}_\tau} \tilde{u}(1-\tilde{y}/\mathrm{Re}_\tau)d\tilde{y}, \tag{2.20}$$

and for channel flow

$$\mathrm{Re} = \int_0^{\mathrm{Re}_\tau} \tilde{u}d\tilde{y}. \tag{2.21}$$

Therefore, given a value of Re_τ, we can use the spectral theory not only compute the MVP, but also the friction factor. The computed friction factor for both pipe flow and channel flow is plotted as a function of Re in Fig. 2.9, which displays a good qualitative agreement with the DNS data shown in Fig. 2.8: the friction factor of pipe flow is consistently higher than that of channel flow as Re increases.

2.6.3 Disparities of shear production

We have shown that the disparities of the MVPs in the wakes and of the friction factor between pipe flow and channel flow are sizable and can be accounted for in the spectral theory through changes in the parameter of the energetic-range correction, β_e.

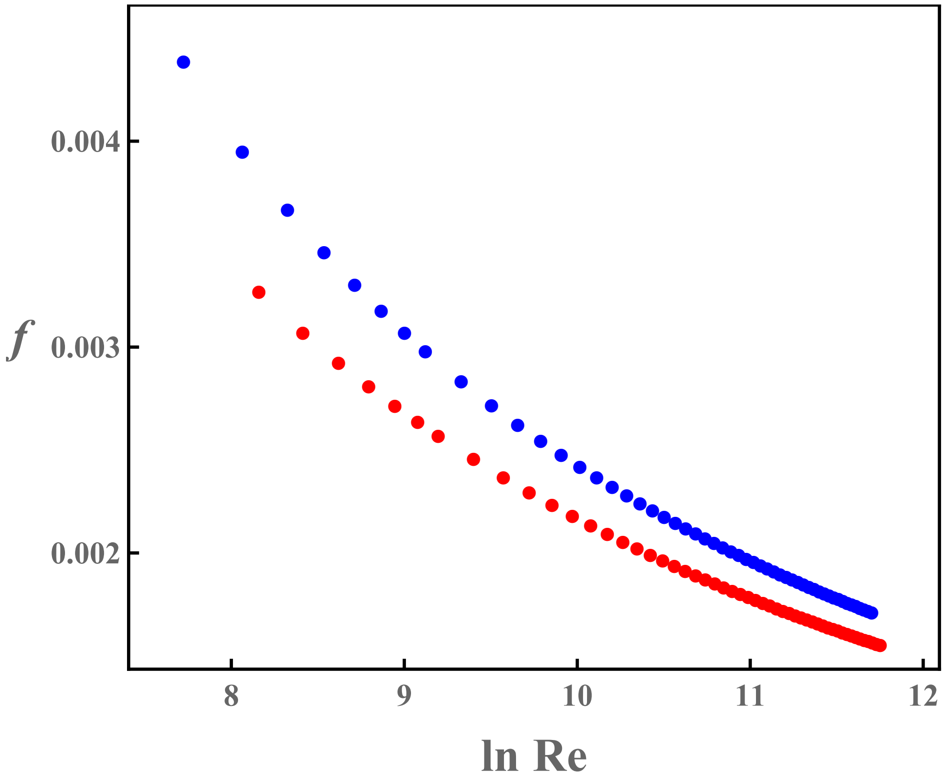

Fig. 2.9: Log-linear plots of the friction factor of pipe flow (blue) and channel flow (red) as a function of Re computed from the spectral theory with $\kappa = 0.4$, $\beta_d = 7$; and $\beta_e = 9$ for pipe flow, $\beta_e = 7$ for channel flow.

Now the question is how significant the difference of the values of β_e between pipe flow and channel flow can be. For each flow, the higher value of β_e means a higher wake, which will result in a lower value of friction factor and vice versa. In other words, if the difference of the values of β_e is large enough, the theoretically computed value of the friction factor of channel flow could exceed that of pipe flow , a result that would be inconsistent with the DNS data. In Fig. 2.10, given a lower value of $\beta_e = 2$ for channel flow, the computed values of the friction factor are higher than those of pipe flow. Thus the difference of the values of β_e should be slight. This conclusion is also supported by the DNS data of shear production. In spite of the significant difference of the MVPs in the wakes and the attendant difference of friction factor between pipe flow and channel flow, the DNS data of shear production overlap nicely in Fig. 2.11. The shear production P reads $P = \tau_{t12}\frac{du(y)}{dy}/\rho$ (see Appendix B). If we substitute Equation 2.13 and reorganize the result using $\tilde{u}$ and $\tilde{y}$, we obtain

$$\tilde{P} = \kappa^2 \rho I^{3/4} \tilde{y}^2 (\frac{d\tilde{u}}{d\tilde{y}})^3, \tag{2.22}$$

where $\tilde{P} = P\nu/u_\tau^4$. Now we can compute the shear production using the spectral theory. As shown in Fig. 2.12, the theoretical results of shear production of pipe flow and channel flow overlap like the DNS data. The difference of the shear production between pipe flow and channel flow cannot be discerned. However, there must be some

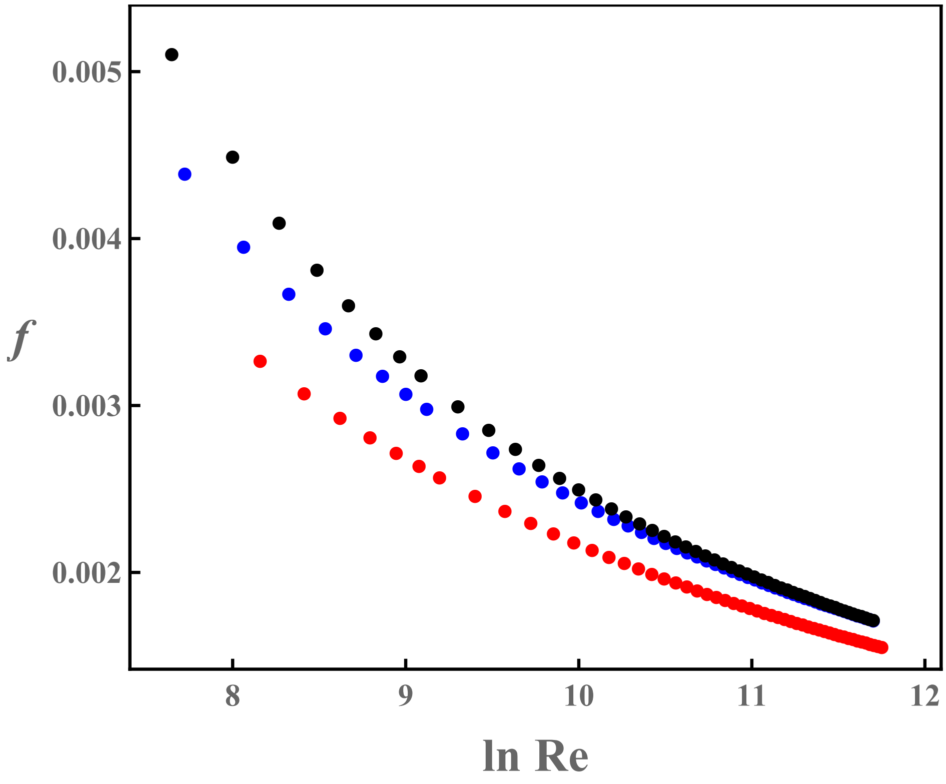

Fig. 2.10: Log-linear plots of the friction factor of pipe flow (blue) and channel flow as a function of Re computed from the spectral theory with $\kappa = 0.4$, $\beta_d = 7$; and $\beta_e = 9$ for pipe flow, $\beta_e = 7$ (red) and $\beta_e = 2$ (black) for channel flow. For $\beta_e = 2$, the values of the friction factor of channel flow exceed those of pipe flow.

difference resulting from the MVP of the shear production as it is calculated from the MVP, which displays significant discrepancy between pipe flow and channel flow in the wakes. To magnify the difference, we plot the premultiplied shear production $\tilde{P}\tilde{y}$ from DNS data, in Fig. 2.13, and as computed from the spectral theory, in Fig. 2.14. The theoretical results of shear production are in good qualitative accord with the DNS data. The difference of the shear productions at large scales is consistent with that of the wakes and also results from the disparity of the energetic-range correction to the spectrum.

2.7 Discussion and summary

We have used the spectral theory of the MVPs to account for the discrepancy of the MVP in the wakes between pipe flow and channel flow, with the following conclusions.

1. The physical origin of the discrepancy of the MVPs in the wakes between pipe flow and channel flow is a manifestation of a slight disparity in the energetic-range corrections to the spectrum. These in turn are due to the geometrical difference between pipe flow and channel flow, whereby the largest eddies in the flow, which are the eddies that dominate momentum transfer in the wake region, are affected

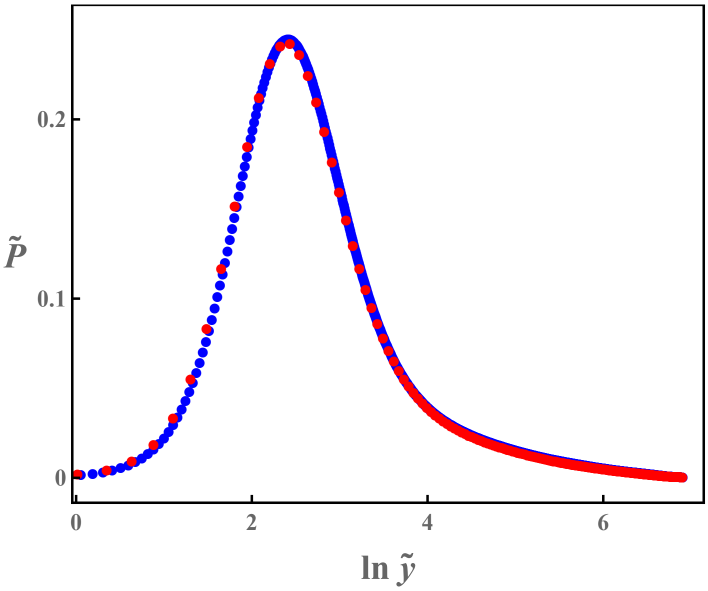

Fig. 2.11: Log-linear plots of the shear production of pipe flow (blue) and channel flow (red) at the same value of $\text{Re}_\tau = 1000$. The data are from DNS: El Khoury *et al.* (2013) (pipe flow), Bernardini *et al.* (2014) (channel flow).

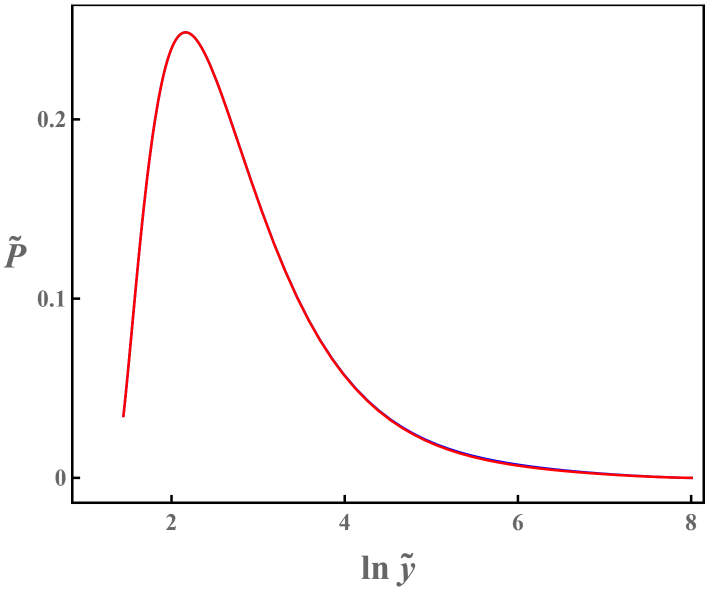

Fig. 2.12: Log-linear plots of the shear production of pipe flow (blue) and channel flow (red) at the same value of $\text{Re}_\tau = 3000$ computed from the spectral theory with $\kappa = 0.4, \beta_d = 7$; and $\beta_e = 9$ for pipe flow, $\beta_e = 7$ for channel flow. Note that the blue line for pipe flow is covered by the red line for channel flow.

by the boundaries of the flow in a way that changes from flow to flow. Thus, the spectrum of turbulent kinetic energy differs in the energetic range depending on the type of flow. Via the spectral link, these differences in the energetic range result in MVPs that differ only in the wakes, consistent with empirical data.

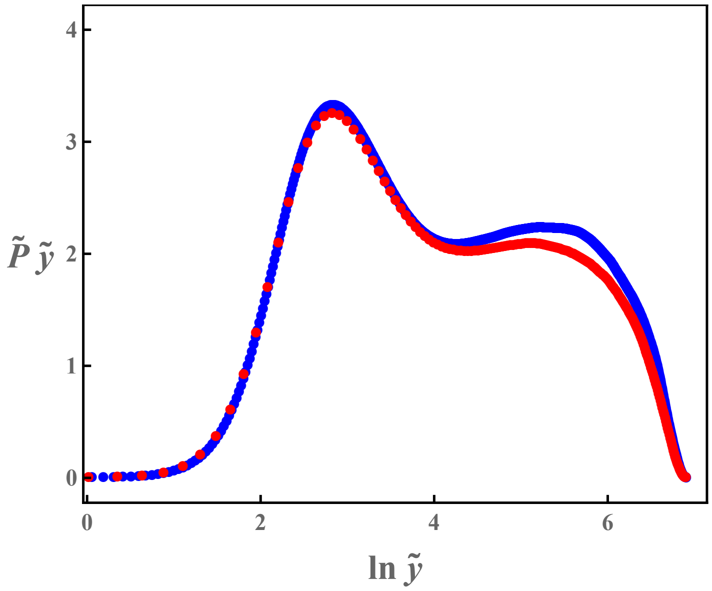

Fig. 2.13: Log-linear plots of the premultiplied shear production of pipe flow (blue) and channel flow (red) at the same value of $\mathrm{Re}_\tau = 1000$. The data are from DNS: El Khoury *et al.* (2013) (pipe flow), Bernardini *et al.* (2014) (channel flow).

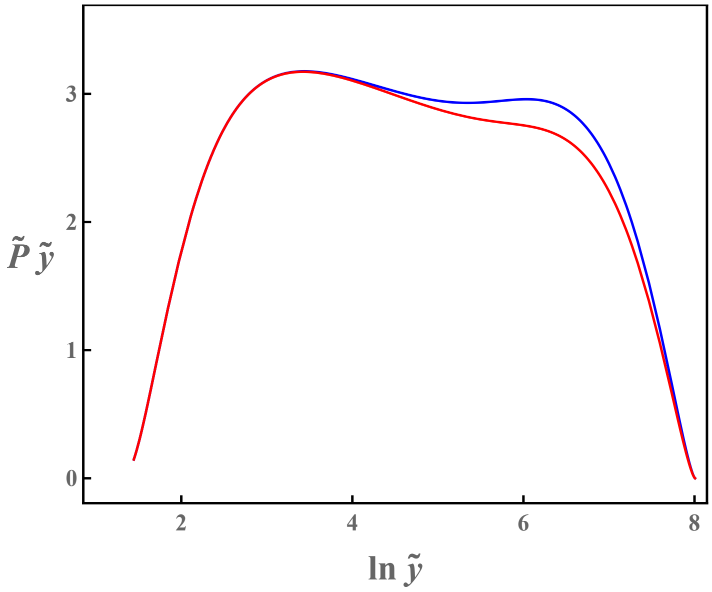

Fig. 2.14: Log-linear plots of the premultiplied shear production of pipe flow (blue) and channel flow (red) at the same value of $\mathrm{Re}_\tau = 3000$ computed from the spectral theory with $\kappa = 0.4, \beta_d = 7$; and $\beta_e = 9$ for pipe flow, $\beta_e = 7$ for channel flow.

2. At smaller lengthscales, comprising the inertial and viscous ranges of the spectrum, the spectrum is universal regardless of the type of flow (pipe or channel). Via the spectral link, small-scale universality of the spectrum translates into MVPs for pipe flow and for channel flow that are identical in the viscous layer, the buffer layer, and the log layer, again consistent with empirical data.

3. The predictions of the spectral theory can be verified by computing the friction factor for pipe flow and channel flow. With the same, slight disparity of energetic-range correction (parameter β_e) that accounts well for the disparities of MVPs, the theory gives a good account of the disparities of friction factor, with the friction factor for pipe flow overshooting that for channel flow. This conclusion cannot be taken for granted. In fact, the values of β_e must differ only slightly: if they differed more, the value of the friction factor of channel flow would overshoot that of pipe flow, which would be at odds with empirical data.

4. The predictions of the spectral theory can be verified by computing the shear production for pipe flow and channel flow. With the same, slight disparity in the value of β_e that accounts well for the disparities of MVPs, the theory gives a good account for the disparities of shear production, which are only apparent, in both the empirical data and the theoretical predictions, when plotted as the premultiplied shear production. In this case, the disparities are seen to be circumscribed to the region far from the wall, coextensive with the wake, in accord with our conclusions regarding the MVPs.

Chapter 3

Spectral theory of plane Couette flow

3.1 Introduction

In plane Couette flow the fluid is confined between two mutually parallel plates separated by a gap of thickness $2b$. The upper plate moves relative to the lower one and parallel to it, at a constant velocity. In the discussion that follows we will work in a frame of reference in which the lower plate is stationary. No pressure gradient is imposed on the fluid; thus the total shear stress is uniform across the thickness of plane Couette flow.

The classical experiments on turbulent plane Couette flow date back to the 1950s, to the independent experiments by Reichardt (1956, 1959) and by Robertson (1959). These classical experiments focused on the friction factor f, which is defined as $f \equiv \tau_0/\rho u_c^2$, where $u_c \equiv u(y = b)$ is the mean velocity at the centerline of the flow (that is, the maximum velocity of the lower half part of plane Couette flow or half the velocity of the moving plate) and the Reynolds number is defined as $\mathrm{Re} \equiv u_c b/\nu$.

From the onset, the experiments revealed a noticeable disparity in the relation between f and Re (Fig. 3.1). In consultation with Reichardt, Robertson repeated his experiments but the disparity prevailed and has never been resolved (Robertson & Johnson, 1970). Later, more experiments on turbulent plane Couette flow became available, including the experiments by Telbany & Reynolds (1982), whose measurements of friction factor are in good accord with Reichardt's, and the experiments by Kitoh *et al.* (2005), whose measurments of friction factor agree well with Robertson's. In the meantime, direct numerical simulations (DNS) of turbulent plane Couette flow became possible. Remarkably, the computational f–Re relation turns out to be quite distinct from either of the experimental f–Re relations (Fig. 3.1). At the same value of Reynolds number Re, the friction factors f of Robertson (1959) and Kitoh *et al.* (2005) are consistently higher than those of Reichardt (1959) and Telbany & Reynolds (1982), and consistently lower than those of DNS.

The Reichardt–Robertson disparity has always been thought of as an anomaly, the inadvertent product of a systematic error that would sooner or later be identified and factored in. The implicit notion has been that to each value of Re there should correspond to a unique turbulent state and, therefore, a unique value of f (Massey & Ward-Smith, 1998).

In view of Fig. 3.1, we argue that this notion should be abandoned. Thus, in what

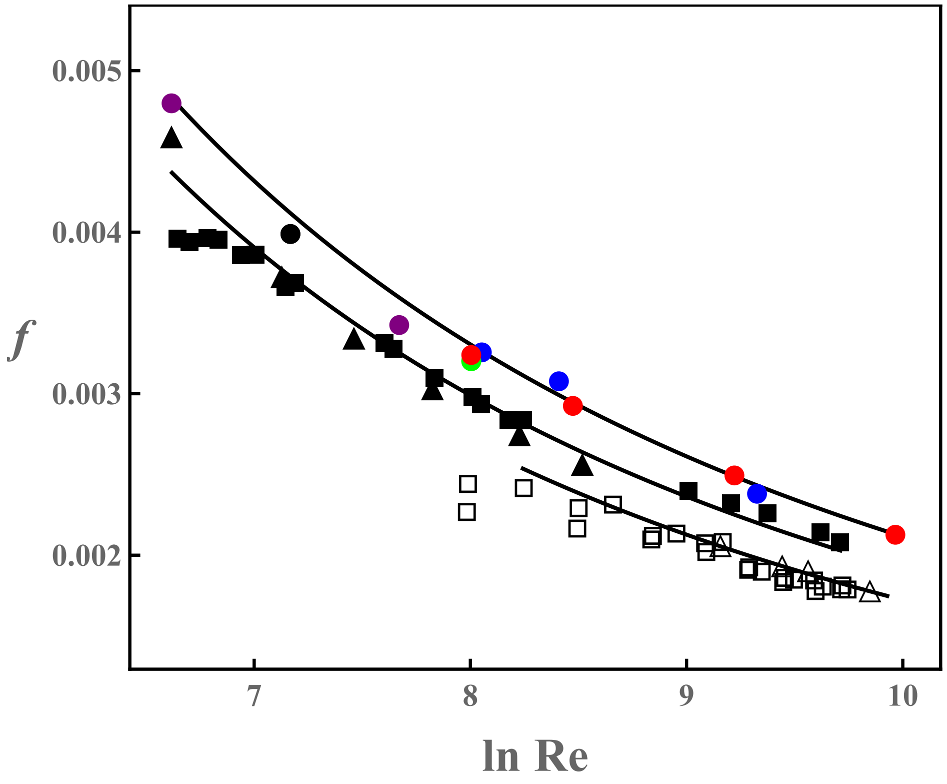

Fig. 3.1: Log-linear plots of experimental and computational data on the relation between the friction factor f and the Reynolds number Re of plane Couette flow. □ Reichardt (1959). △ Telbany & Reynolds (1982). ■ Robertson (1959). ▲ Kitoh *et al.* (2005). ○ DNS from Lee & Kim (1991) (Green), Bech *et al.* (1995) (black), Tsukahara *et al.* (2006) (Purple), Avsarkisov *et al.* (2014) (Blue), and Pirozzoli *et al.* (2014) (Red), respectively. Solid lines are the empirical formulas from Telbany & Reynolds (1982): $0.0331/(\log \mathrm{Re})^2$, Robertson (1959): $0.0361/(\log \mathrm{Re})^2$, and Pirozzoli *et al.* (2014): $0.0399/(\log \mathrm{Re})^2$, respectively.

follows, we shall accept as a fact the experimental and computational evidence that to each value of Re there might actually correspond to multiple values of f. Furthermore, we shall assume that each one of these values of f signals a specific, alternative turbulent state.

We are ready now to set specific objectives for this chapter. It is not our intention here to seek an explanation for the existence of multiple alternative turbulent states in plane Couette flow. Rather, we seek to address three basic questions: How are we to characterize a turbulent state? In what ways do the various turbulent states differ among themselves? Can the existence of multiple turbulent states be reconciled with the phenomenological theory of turbulence? To start answering these questions, we turn our attention to the mean-velocity profiles (MVPs). The MVPs have been largely ignored in discussions of the Reichardt–Robertson disparity, yet they may, via the spectral theory, facilitate a characterization of the various turbulent states that observed in plane Couette flow.

In Fig. 3.2, we plot the proper data of MVPs of the highest Re available in various

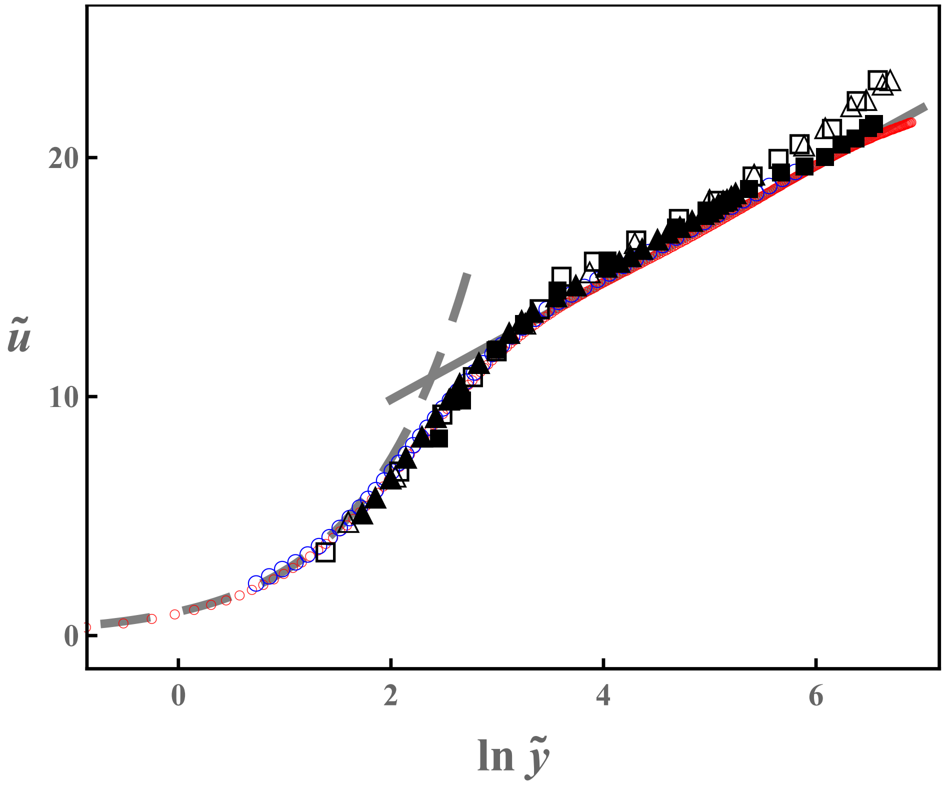

Fig. 3.2: Log-linear plots of experimental and computational data on the MVPs of plane Couette flow. □ Reichardt (1959) at $\mathrm{Re}_\tau = 723$. △ Telbany & Reynolds (1982) at $\mathrm{Re}_\tau = 805$. ■ Robertson (1959) at $\mathrm{Re}_\tau = 700$. ▲ Kitoh *et al.* (2005) at $\mathrm{Re}_\tau = 192$. ○ DNS from Avsarkisov *et al.* (2014) (Blue) at $\mathrm{Re}_\tau = 550$, and Pirozzoli *et al.* (2014) (Red) at $\mathrm{Re}_\tau = 986$, respectively. The grey line denotes the log law, $\tilde{u}(\tilde{y}) = \frac{1}{\kappa} \ln \tilde{y} + B$ with $\kappa = 0.41$ and $B = 5$. The dashed grey line denotes the laminar solution of the viscous layer, $\tilde{u}(\tilde{y}) = \tilde{y}$. Each MVP extends from the wall to $\tilde{y} = \mathrm{Re}_\tau$.The MVPs collapse onto a single curve close to the wall in the viscous layer, the buffer layer, and the log layer while there are significant discrepancies displaying in the wakes.

experiments and DNS for plane Couette flow. From that figure we can verify that at comparable values of Re_τ, the various MVPs are indistinguishable everywhere in the domain of the flow *except for the wake*. Indeed, disparities in the f–Re relation are reflected in the wakes of the MVPs, and only there, in the form of varying degrees of overshooting of the log layer.

Even though some of the values of Re_τ that appear in Fig. 3.2 are not entirely comparable with the others (especially for the experiment of Kitoh *et al.* (2005) and the DNS of Avsarkisov *et al.* (2014), where the highest available values of Re_τ are rather small), it can be clearly seen that the overshooting is largest for the experiments of Reichardt (1959) and Telbany & Reynolds (1982), second largest for the experiments of Robertson (1959), and smallest for the DNS of Pirozzoli *et al.* (2014) (Fig. 3.2). That is to say, a higher friction factor consistently corresponds to a smaller overshooting in the wakes of the MVPs. Indeed, the overshooting can be quantified by the value of the non-dimensional velocity slope at the flow centerline, which is defined as

$$R_s \equiv \frac{b}{u_\tau}\frac{du}{dy}|_{y=b} \equiv \frac{d\tilde{u}}{d\ln\tilde{y}}|_{\tilde{y}=\mathrm{Re}_\tau}. \tag{3.1}$$

A higher value of R_s indicates a larger overshooting in the wakes of the MVPs. In Fig. 3.3 it is possible to confirm the conclusion from Fig. 3.2, namely that a higher friction factor consistently corresponds to a smaller overshooting in the wakes of the MVPs (if we exclude as an outlier, likely due to scatter, the only reverse case, which occurs at a very small Re).

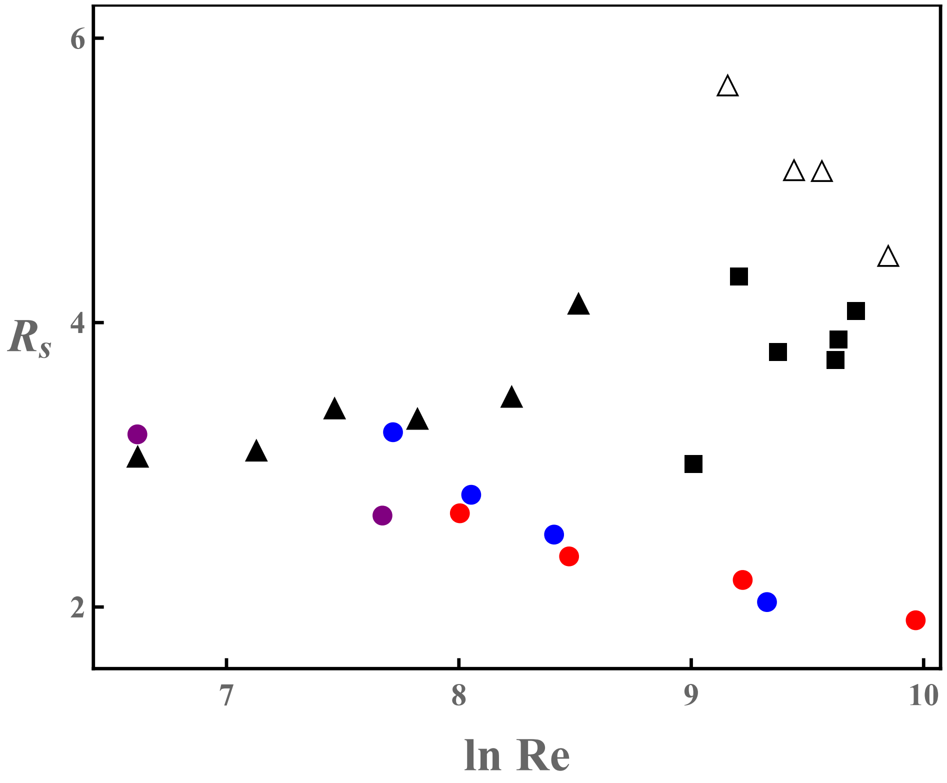

Fig. 3.3: Log-linear plots of experimental and computational data on the relation between the non-dimensional velocity slope at the flow centerline, R_s, and the Reynolds number Re of plane Couette flow. △ Telbany & Reynolds (1982). ■ Robertson (1959). ▲ Kitoh *et al.* (2005). ○ DNS from Tsukahara *et al.* (2006) (Purple), Avsarkisov *et al.* (2014) (Blue), and Pirozzoli *et al.* (2014) (Red), respectively.

3.2 Spectral theory

At this point we use the spectral theory of the MVPs of plane Couette flow (formulated in Chapter 3) to make the theoretical predictions shown in Figs. 3.4 and 3.5. The theory can reproduce all of the salient trends in the experimental and computational data (also shown in Figs. 3.1 and 3.2). Furthermore, the disparities in friction factor and the attendant disparities in the wakes are accounted for by a single parameter of the theory: the dimensionless parameter β_e of the energetic-range correction.

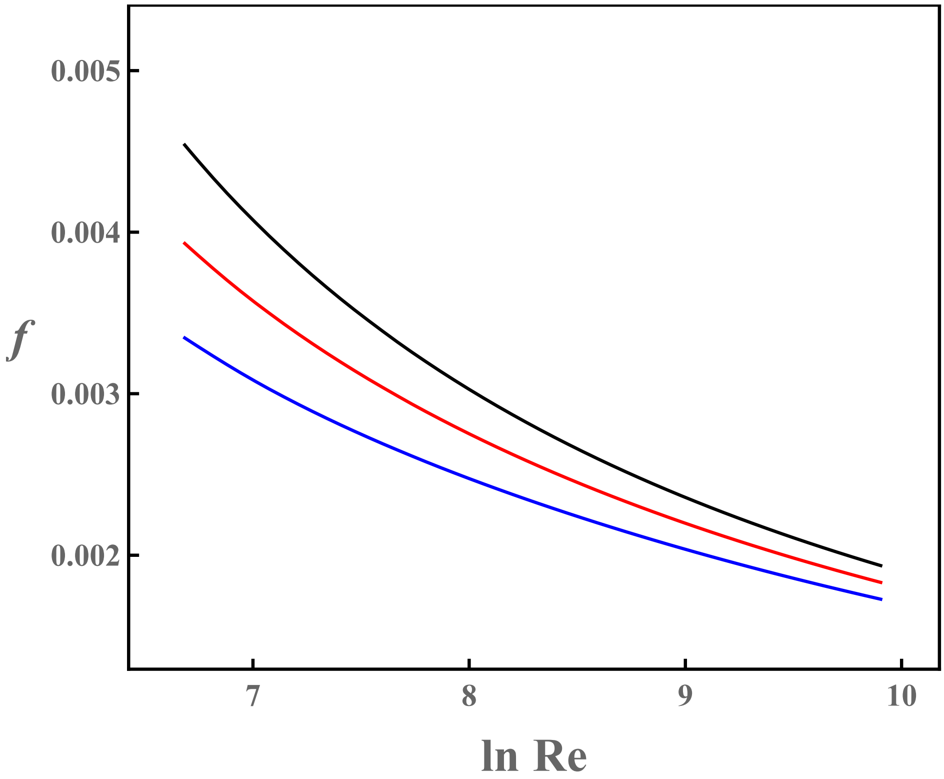

Fig. 3.4: Log-linear plots of the friction factor of plane Couette flow as a function of Re computed from the spectral theory with $\kappa = 0.41$, $\beta_d = 7$, and three different values of β_e: $\beta_e = 1$ (black line), $\beta_e = 2$ (red line), $\beta_e = 3$ (blue line).

We conclude that feasible turbulent states can only differ at the lengthscales of the energetic-range correction (that is, the largest lengthscales of the spectrum, and the only ones affected by finite-domain effects). Thus, contrary to the view that multiple turbulent states might be somewhat at odds with the phenomenological theory of turbulence (this view was put forward in a discussion of multiple turbulent states in Taylor-Couette flow (Huisman *et al.*, 2014; van der Veen *et al.*, 2016), but is applicable to plane Couette flow as well), the difference between any one such state and another is totally circumscribed to the largest lengthscales in the flow, with the implication that, at any given Reynolds number, all turbulent states are indistinguishable at inertial and viscous lengthscales, and that small-scale universality (Kolmogórov, 1941*b*; Schumacher *et al.*, 2014) holds regardless of state, in accord with the phenomenological theory.

3.2.1 Attendant disparities in macroscopic properties other than the MVPs

As per the spectral theory, a higher value of β_e indicates stronger finite-domain effects and results in a lower friction factor and a larger overshooting in the wakes of the MVPs (Figs. 3.4 and 3.5). From this conclusion we expect that a change in a turbulent state (and the attendant change in the f–Re relation) should have a marked

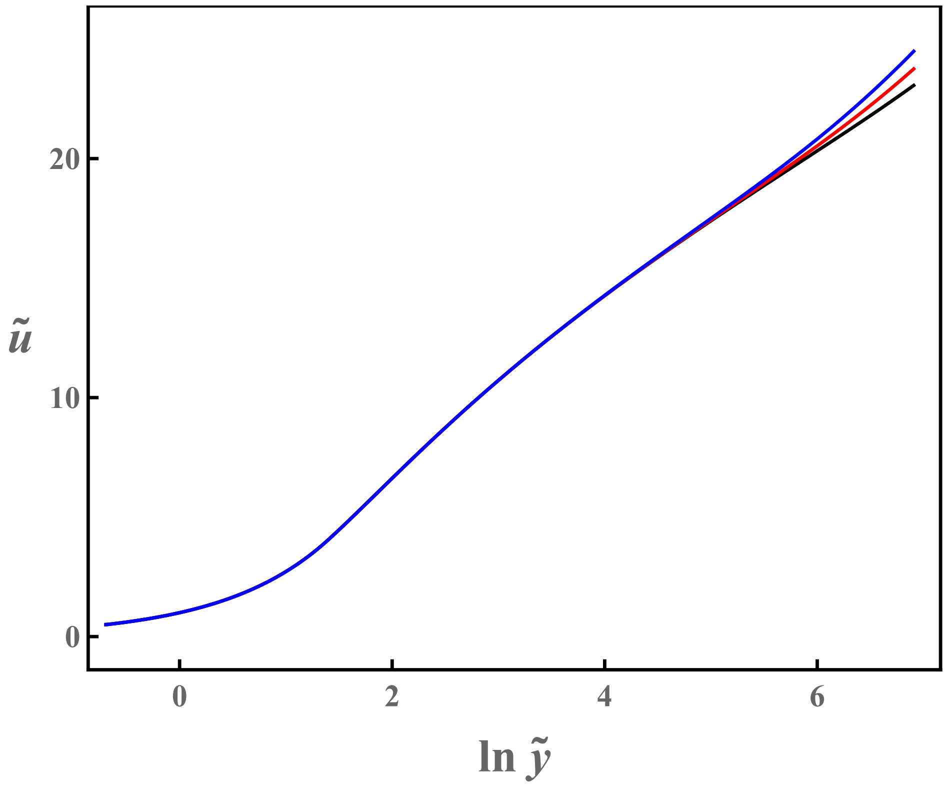

Fig. 3.5: Log-linear plots of the MVPs of plane Couette flow at the same value of $\mathrm{Re}_\tau = 1000$ computed from the spectral theory with $\kappa = 0.41, \beta_d = 7$, and three different values of β_e: $\beta_e = 1$ (black line), $\beta_e = 2$ (red line), $\beta_e = 3$ (blue line).

effect on the turbulent velocity fluctuation profile $V(y) \equiv \overline{u_i' u_i'}$ (because most of the turbulent kinetic energy is carried by the largest turbulent eddies in the flow). Indeed, we can predict that a turbulent state with a lower friction factor corresponds to stronger finite-domain effects, which in turn should correspond to higher turbulent velocity fluctuations. This prediction is confirmed in Fig. 3.6, where we plot the most recent DNS and experimental data, for the highest available values of Re, on the $V(y)$ profile (that is, on the relation between $\tilde{V} \equiv V/u_\tau^2$ and $\tilde{y}$).

The spectral theory does not directly give the turbulent velocity fluctuations. However, the turbulent wall-normal velocity fluctuation profile $v_{rms}(y)$ may be identified with v_y (the characteristic velocity of the dominant eddy at a distance y from the wall); in Fig. 3.7, we consider that at a distance y from the wall, the turbulent wall-normal velocity fluctuation results mostly from the turbulent eddies centering at the wetted surface W_y. Then, the dominant eddies contributing to the turbulent wall-normal velocity fluctuation $v_{rms}(y)$ must be of size $s = y$ as v_s is a monotonically increasing function of s (see Chapter 2). Thus, we assume that the $v_{rms}(y) = v_y$. From Equations 2.12 and 2.13, v_y (or $v_{rms}(y)$) can be directly computed from the spectral theory as

$$v_y = v_{rms}(y) = (\kappa^2 \kappa_\varepsilon)^{1/3} I^{3/4} y \frac{du(y)}{dy}. \tag{3.2}$$

We now are ready to compare our theoretical results of $v_{rms}(y)$ to the corresponding

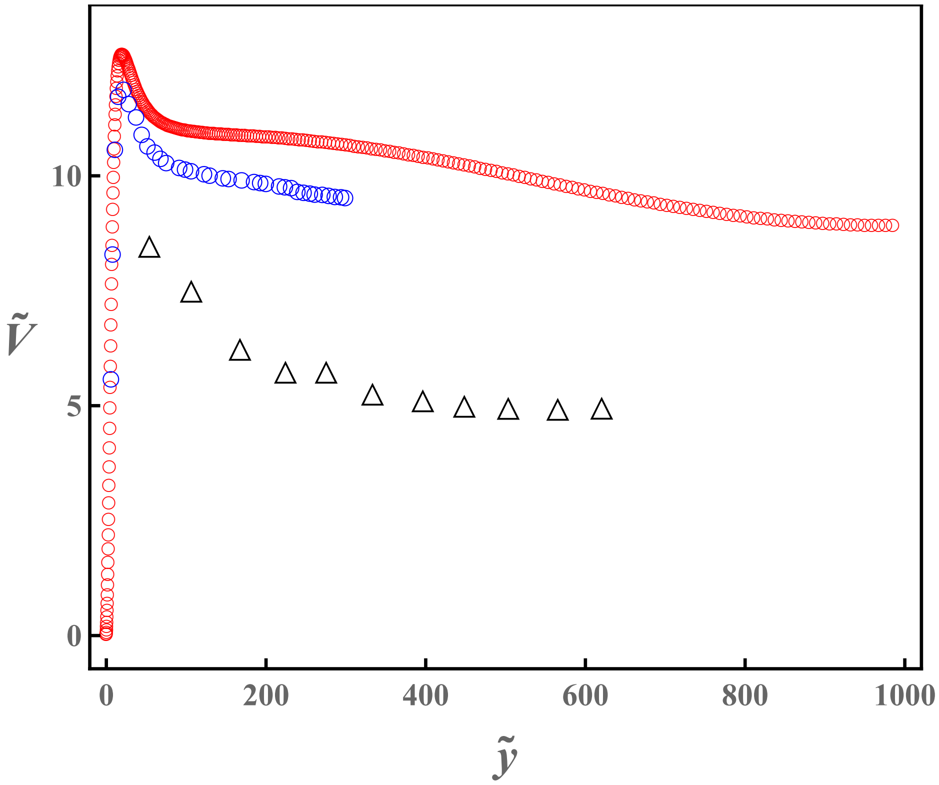

Fig. 3.6: Plots of experimental and computational data on the turbulent velocity fluctuation profiles of plane Couette flow. △ Telbany & Reynolds (1982) at $\mathrm{Re}_\tau = 805$. ○ DNS from Avsarkisov *et al.* (2014) (Blue) at $\mathrm{Re}_\tau = 550$, and Pirozzoli *et al.* (2014) (Red) at $\mathrm{Re}_\tau = 986$, respectively.

experimental and computational data. Similar to the $V(y)$ profile, the $v_{rms}(y)$ profile (that is, the relation between $\tilde{v}_{rms} \equiv v_{rms}/u_\tau$ and $\tilde{y}$) should also differ depending on the turbulent state. What we expect is that because of weaker finite-domain effects, a higher friction factor should also correspond to a higher turbulent wall-normal velocity fluctuation, which is again confirmed by Fig. 3.8 and can be reproduced by the spectral theory by varying the dimensionless parameter β_e of the energetic-range correction (Fig. 3.9).

3.3 A note on the asymptotic value of the velocity slope at the flow centerline

In plane Couette flow, the value of the non-dimensional velocity slope at the flow centerline, R_s (which is zero for pipe flow and channel flow because of the vanished shear stress), has elicited considerable interest since the 1950s when the classical experiments on turbulent plane Couette flow were conducted by Reichardt (1956, 1959). Regarding how R_s varies with Re (Fig. 3.3), while most recent DNS studies report a slow decrease of R_s with increasing Re, different trends have been reported in various experiments. The discrepancies have been attributed to the difficult measurements of small velocity

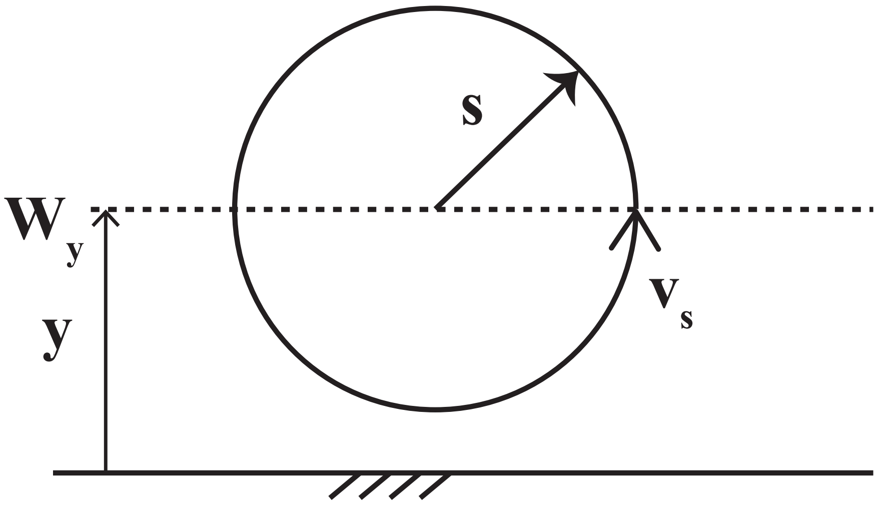

Fig. 3.7: Schematic used to derive the expression for the turbulent wall-normal velocity fluctuation $v_{rms}(y)$.

differences in experiments (Pirozzoli *et al.*, 2014). Regarding whether the value of R_s will approach a constant in the limit of infinite Re, a convincing conclusion has never been reached because of the limitation to achieve very high Reynolds number in both experiments and simulations. Thus, the value of the non-dimensional velocity slope at the flow centerline remains an open question till now (Avsarkisov *et al.*, 2014). An alternative definition of the non-dimensional velocity slope at the flow centerline is

$$S_0 \equiv \frac{b}{u_c}\frac{du}{dy}|_{y=b} \equiv \frac{d\tilde{u}}{d\ln\tilde{y}}|_{\tilde{y}=\mathrm{Re}_\tau}\sqrt{f} = R_s\sqrt{f}. \tag{3.3}$$

Here, the spectral theory will be employed to address the open question on the value of the non-dimensional velocity slope at the flow centerline of plane Couette flow. R_s and S_0 are readily to be calculated from the theoretically computed MVP and friction factor. At the flow centerline where the viscous shear stress is negligible, Equation 2.15 gives that $R_s = I_s^{-3/8}/\kappa$, where $I_s \equiv I(\eta/b, 1)$, which depends on Re via η/b. For a high enough Reynolds number, η/b reduces to zero. Thus $I_s = I(0,1)$ is not dependent on Re any more and R_s becomes a constant value, which is determined by the energetic-range correction to the spectrum via $I(0,1)$. Note that the conclusion that R_s becomes a constant value at high Reynolds numbers is valid regardless of the from of the function $I(\eta/s, s/b)$, thus regardless of the form of the energetic-range correction to the spectrum, as long as the energetic-range correction to the spectrum is a function of s/b. In the standard model of the spectrum we are using here, the dimensionless parameter β_e of the energetic-range correction sets the constant value of R_s at high Reynolds numbers (Fig. 3.10) as I_s becomes

$$I(0,1) \equiv \frac{2}{3}\int_1^\infty \xi^{-5/3}(1+\beta_e^2/\xi^2)^{-17/6}d\xi, \tag{3.4}$$

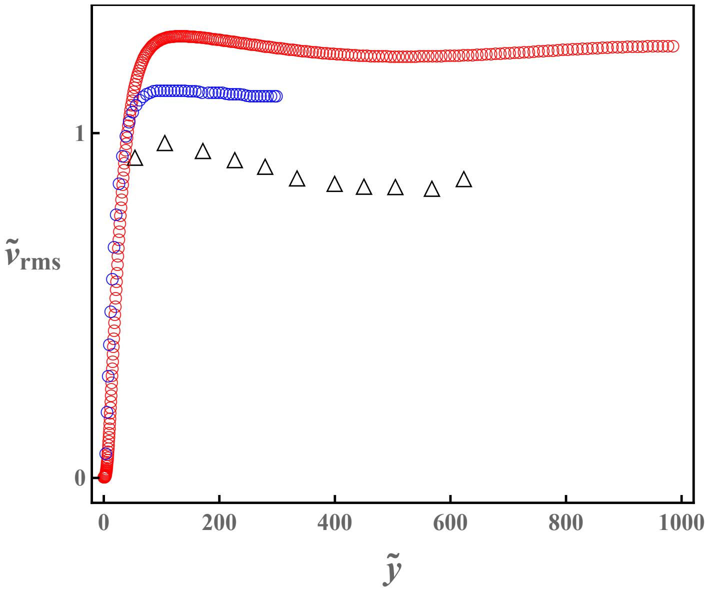

Fig. 3.8: Plots of experimental and computational data on the turbulent wall-normal velocity fluctuation profiles of plane Couette flow. △ Telbany & Reynolds (1982) at $\mathrm{Re}_\tau = 805$. ○ DNS from Avsarkisov *et al.* (2014) (Blue) at $\mathrm{Re}_\tau = 550$, and Pirozzoli *et al.* (2014) (Red) at $\mathrm{Re}_\tau = 986$, respectively.

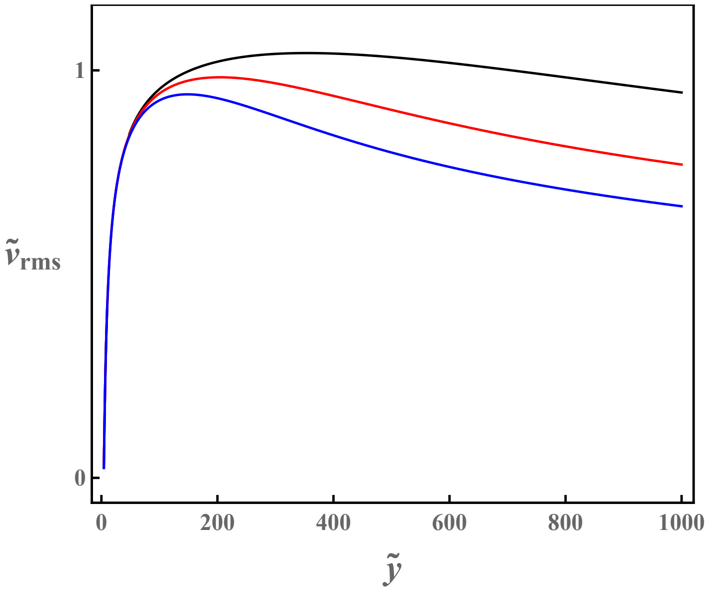

Fig. 3.9: Plots of the turbulent wall-normal velocity fluctuation profiles of plane Couette flow at the same value of $\mathrm{Re}_\tau = 1000$ computed from the spectral theory with $\kappa = 0.41, \beta_d = 7$, and three different values of β_e: $\beta_e = 1$ (black line), $\beta_e = 2$ (red line), $\beta_e = 3$ (blue line).

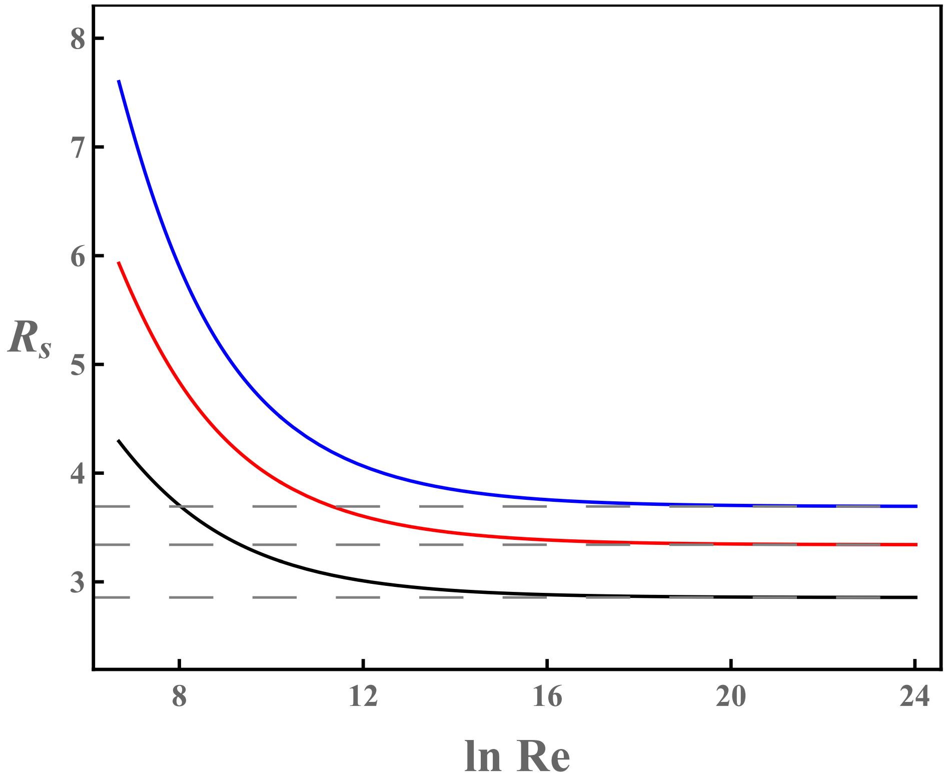

Fig. 3.10: Log-linear plots of the non-dimensional velocity slope at the flow centerline R_s of plane Couette flow as a function of Re computed from the spectral theory with $\kappa = 0.41, \beta_d = 7$, and three different values of β_e: $\beta_e = 1$ (black line), $\beta_e = 2$ (red line), $\beta_e = 3$ (blue line). The dashed grey lines denote that at high Reynolds numbers, the constant values of $R_s = 2.86, 3.34$, and 3.69 for $\beta_e = 1$, $\beta_e = 2$, and $\beta_e = 3$, respectively.

which is a constant value only depending on β_e. We have argued that a certain β_e signifies a specific turbulent state of plane Couette flow in Section 3.2. That is to say, for each turbulent state, there is an asymptotic constant value of R_s in the limit of high Re as shown in Fig. 3.10.

In Fig. 3.11, we also plot $S_0 \equiv R_s\sqrt{f}$ as a function Re. The decreasing rate of S_0 is getting slow in high Reynolds number region as the friction factor f is decreasing slowly. At infinite Reynolds number, if the friction factor becomes zero, then S_0 will be zero.

3.4 Discussion and summary

We have used the spectral theory of the MVPs of turbulent plane Couette flow to revisit the Reichardt–Robertson disparity, with the following conclusions.

1. The Reichardt–Robertson disparity is a manifestation of the existence of multiple turbulent states in plane Couette flow.
2. A turbulent state may differ from any alternative turbulent state only at the lengthscales that are affected by the energetic-range correction—that is, the

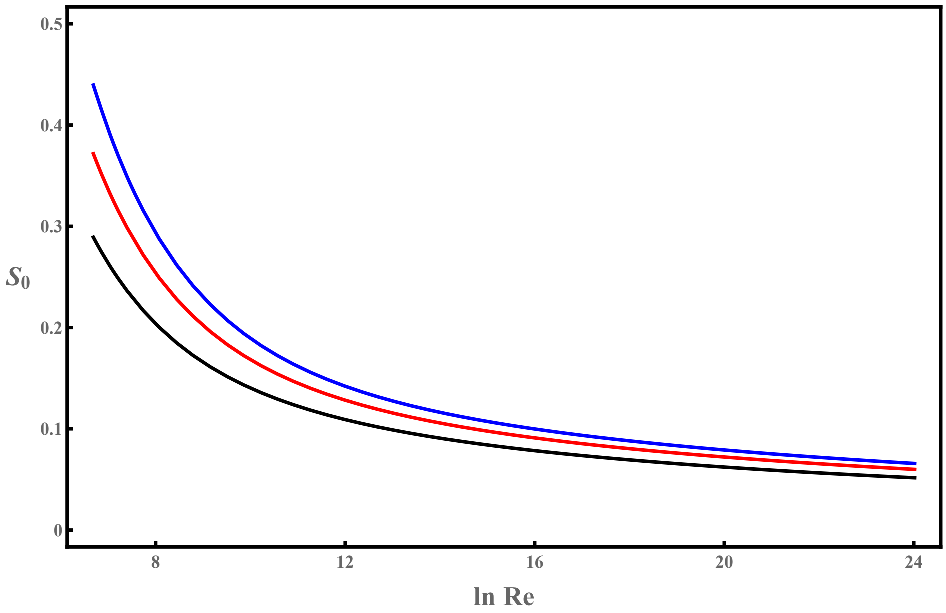

Fig. 3.11: Log-linear plots of the non-dimensional velocity slope at the flow centerline S_0 of plane Couette flow as a function of Re computed from the spectral theory with $\kappa = 0.41, \beta_d = 7$, and three different values of β_e: $\beta_e = 1$ (black line), $\beta_e = 2$ (red line), $\beta_e = 3$ (blue line).

largest lengthscales in a flow, which are proportional to the thickness of the flow.

3. Corollary: a change in turbulent state can only alter the wake of the attendant MVP (which is the part of the MVP dominated by the eddies of the energetic range).
4. At smaller lengthscales, comprising the inertial and viscous portions of the spectrum of turbulent kinetic energy, the spectrum is one and the same regardless of the turbulent state, consistent with the phenomenological theory of turbulence.
5. Thus, the existence of multiple turbulent states does not contradict the universality of the spectrum of turbulent kinetic energy (such as this universality is understood in the phenomenological theory).
6. Conversely, spectral universality does not rule out the existence of multiple turbulent states.

Our analysis might extend beyond plane Couette flow to a general class of flows driven by moving boundaries. Consider, for instance, the recent papers, Huisman *et al.* (2014) and van der Veen *et al.* (2016), on multiple states in highly turbulent Taylor-Couette flows, these studies report two branches of global torque (which is analogous to the friction factor f). These branches correspond to differences in the wake of the MVPs of azimuthal velocity and in the size of large-scale Taylor vortices (which correspond to differences in the energetic-range correction to the spectrum). The spectral theory might help shed light on these issues. What is more, by singling out the most likely, and quite possibly the sole, agents of the occurrence of multiple alternative turbulent states in plane Couette flow, our analysis provides patent pointers in the search for a mechanistic explanation of the Reichardt–Robetson disparity and analogous manifestations of a lack of uniqueness in plane Couette flow and other turbulent flows driven by moving boundaries. Those agents are, as we have demonstrated, the largest turbulent eddies in a flow. We submit, on the basis of the analysis of this chapter, that it is in their interactions with the boundaries of the turbulent domain that the origin of multiple alternative turbulent states should be sought.

Chapter 4

Spectral theory of thermally-stratified plane Couette flow

4.1 Introduction

In previous chapters, we have considered turbulent flows of constant-density fluids. Here we shift focus to study turbulent flows of fluids with temperature-dependent density, i.e., we consider thermally-stratified turbulent flows (Turner, 1973; Stull, 1988). We are surrounded by such flows. Take, for example, the flow of air in the atmospheric boundary layer, the approximately 1 km thick region enveloping the surface of the Earth. Interaction with the Earth's surface renders the air flow turbulent via two concurrent effects:

1. frictional drag with the surface shears the flow;

2. heat transfer with the surface (which is subjected to the diurnal cycle of heating and cooling) makes the flow thermally stratified (Wallace & Hobbs, 2006), which, via the dependence of density on temperature, induces buoyancy in the flow.

This shear and buoyancy generate turbulence; and the turbulent flow dictates the environment for all terrestrial life (Garratt, 1992, 1994). Consequently, there is considerable interest in studying thermally-stratified, turbulent flows in the atmospheric boundary layer.

We consider a simpler case of such flows. Assuming zero mean pressure gradient in the flow direction and constant total shear stress normal to the flow direction, and ignoring the roughness of the surface, we study fully-developed, thermally-stratified plane Couette flow. In a plane Couette flow, the fluid is confined between two parallel smooth walls, where the lower wall is stationary and the flow is driven by the upper wall moving at a constant velocity. At the walls, we have no-slip and no-penetration boundary conditions (Davidson, 2004). For the thermally-stratified case, we also invoke an additional boundary condition: at the walls, the heat flux is constant. To model thermally-stratified flows, we invoke the widely used Boussinesq approximation (Turner, 1973; Kundu & Cohen, 2002). Under this approximation, the governing equations are as follows.

The equation of state for the fluid, which links the density variation $\delta\rho$ (with respect to the reference density ρ_0) with the temperature variation δT, reads:

$$\frac{\delta\rho}{\rho} = -\alpha\delta T, \tag{4.1}$$

where α is the coefficient of thermal expansion. The kinematic viscosity of the fluid, ν, is assumed to be independent of T. Under the Boussinesq approximation, attention is restricted to small temperature variations, and the equation for the conservation of mass remains the same as that for incompressible flows (see Appendix A), namely:

$$\boldsymbol{\nabla}\cdot\boldsymbol{u} = 0, \tag{4.2}$$

where $\boldsymbol{u}$ is the velocity. The equation for the conservation of momentum reads (cf. Appendix A):

$$\frac{D\boldsymbol{u}}{Dt} = -\frac{1}{\rho}\boldsymbol{\nabla}p + \nu\nabla^2\boldsymbol{u} + \frac{\rho}{\rho_0}\boldsymbol{g}, \tag{4.3}$$

where D/Dt is the material derivative, p is the pressure,and $\boldsymbol{g}$ is the gravitational acceleration. The effect of density variation is restricted to the last term of the right-hand side—the buoyant term. Last, the equation for the conservation of energy (i.e., the heat equation) reads:

$$\frac{DT}{Dt} = k_d\nabla^2 T, \tag{4.4}$$

where k_d is the thermal diffusivity.

4.2 The Monin-Obukhov similarity theory

Although turbulent flows of wall-bounded, thermally-stratified fluids are well described by Equations 4.1–4.4, these equations, despite the simplifying approximations, cannot yet be solved analytically. Instead of attempting to solve the equations, the theoretical framework for such flows builds on the tools of dimensional analysis (Barenblatt, 1996). The most well-known case of such a framework is the Monin-Obukhov similarity theory (MOST) (Obukhov, 1946; Monin & Obukhov, 1954). Proposed about 70 years ago for flows in the atmospheric boundary layer, this seminal theory continues to guide our understanding of thermally-stratified flows in general.

As an application of MOST, we consider the thermally-stratified plane Couette flow. When the lower wall is heated, the flow becomes unstably stratified. Conversely, when the lower wall is cooled, the flow becomes stably stratified. At a distance y from the lower wall, the local mean velocity, u, can be obtained by averaging the instantaneous velocity over a long period of time. The resultant profile $u(y)$ is known as the mean-velocity profile (MVP), the scaling and shape of which is the focus of this chapter.

In MOST, attention is restricted to an intermediate region of the MVP—not too close to a wall where viscosity affects the flow and not too far from a wall where external confinement affects the flow. In this region, for the vertical gradient of the MVP, $\frac{du}{dy}$, MOST posits:

$$\frac{du}{dy} = G(y, \tau_0, \rho, g, \alpha, H_0), \tag{4.5}$$

where G is an unspecified function, τ_0 is the wall shear stress, and H_0 is the wall heat flux. Note that because the region near the wall is not included, the effects of molecular diffusion of momentum (via ν) and of molecular diffusion of heat (via k_d) are not considered. Similarly, the distance between the two walls, which brings in the effects of external confinement, is not considered. (We will return to these considerations in Section 4.5.)

Using the Buckingham–Pi theorem (Barenblatt, 1996), the functional relation between seven dimensional variables of Equation 4.5 can be expressed as an equivalent functional relationship between two dimensionless variables:

$$\frac{du}{dy}\frac{\kappa y}{u_\tau} = \phi_u\left(y/L_0\right), \tag{4.6}$$

where κ is a dimensionless constant (which we will discuss shortly), $u_\tau \equiv \sqrt{\tau_0/\rho}$ is the friction velocity, and ϕ_u is a dimensionless function that depends only on the stability parameter, y/L_0 (where $L_0 \equiv -u_\tau^3/(\kappa g \alpha H_0)$, known as the Obukhov length, is the characteristic height at which turbulence effected by shear and buoyancy are comparable). Since the functional form of ϕ_u cannot be determined by MOST, to proceed, one seeks guidance from empirical data, which shows that for small $|y/L_0|$, ϕ_u is a constant ≈ 1 (Businger *et al.*, 1971; Kader & Yaglom, 1990). In this limit, integrating Equation 4.6 yields the well-known "log law" for canonical wall-bounded turbulent flows:

$$\tilde{u} = \frac{1}{\kappa}\ln\tilde{y} + B, \tag{4.7}$$

where, following standard convention, we express the log law in the "wall variables" ($\tilde{u} \equiv u/u_\tau$ and $\tilde{y} \equiv u_\tau y/\nu$, where ν is the fluid kinematic viscosity); κ (the Kármán constant) and B are dimensionless constants of the log law, whose values are determined from empirical data. The deviation of ϕ_u from 1 quantifies the deviation of the MVP from the log law. From empirical data it is known that as the stratification becomes stronger (i.e., the absolute value of heat flux H_0 increases and thus the absolute value of Obukhov length L_0 decreases), the log layer becomes thinner, and finally, for strong stratification the log law disappears. We discuss this feature in more detail in the next section.

4.3 Mean-velocity profile: empirical data

We begin our considerations by stepping beyond the domain of MOST, which focuses on the intermediate region of the MVP, and discuss the salient features of the MVP over its whole extent, from the lower wall to the centerline. Note that, by symmetry, the upper half of the MVP mirrors the shape of the lower half, to which we restrict attention.

Before discussing the MVP, it is useful to list the various dimensionless parameters that characterize the flow. Three independent dimensionless parameters are needed to characterize the flow; for example, the bulk Reynolds number, $\mathrm{Re} \equiv u_b h/\nu$, which measures the ratio of inertial forces to viscous forces, the Rayleigh number, $Ra \equiv \alpha g \Delta T (2h)^3/(k_d \nu)$, which measures the ratio of buoyant forces to viscous forces, and the Prandtl number, $Pr \equiv \nu/k_d$, which measures the ratio of momentum diffusivity and thermal diffusivity. Here, u_b is the bulk (average) velocity, i.e., the flow flux divided by the cross-sectional area (note that for a plane Couette flow, u_b equals the flow centerline velocity, u_c); $2h$ is the distance between the two walls; ΔT is the temperature difference between the two walls. Instead of the bulk Reynolds number, sometimes the friction Reynolds number, $\mathrm{Re}_\tau \equiv u_\tau h/\nu$, is used and instead of the Rayleigh number, sometimes the friction Richardson number, $Ri_\tau \equiv \alpha g \Delta T h/u_\tau^2$, or the bulk Richardson number, $Ri_b \equiv \alpha g \Delta T h/(2u_b^2)$, is used. (The Richardson number measures the ratio of buoyant production to shear production.) In addition, a dimensionless parameter known as Nusselt number, $Nu \equiv 2hH_0/(k_d \Delta T)$, which measures the ratio of convective to conductive heat flux, is also customarily used in the study of thermally-stratified turbulent flows. We can also consider a different dimensionless parameter, h/L_0, which is the ratio of the domain size to the Obukhov length. h/L_0 can be expressed in terms of the above-mentioned dimensionless parameters as $h/L_0 = \kappa Ra Nu/(16\mathrm{Re}_\tau^3 Pr^2) = \kappa Ri_b \mathrm{Re}_b^2 Nu/(\mathrm{Re}_\tau^3 Pr) = \kappa Ri_\tau Nu/(2\mathrm{Re}_\tau Pr)$. To characterize the flow, we consider the dimensionless parameters: Re_τ, h/L_0, and Pr.

We collate MVPs from several recent direct numerical simulations (DNS) of thermally-stratified plane Couette flows and thermally-stratified channel flows (García-Villalba & del Álamo, 2011; García-Villalba *et al.*, 2011; Deusebio *et al.*, 2015; Pirozzoli *et al.*, 2017). In Fig. 4.1, we plot these MVPs in wall variables, $\tilde{u}$ vs. $\tilde{y}$. First, we consider the intermediate region analyzed in MOST. Here, for wall-bounded turbulent flows of constant-density fluids, $(h/L_0 = 0)$, the MVP follows the log law. The MVPs deviate downward from the log law for unstable stratification $(h/L_0 < 0)$; and the MVPs deviate upward from the log law for stable stratification $(h/L_0 > 0)$. Such deviations have long been known and are noted in textbook discussions of this topic (see, e.g., Fig. 4.2).

From the DNS data of Fig. 4.1, we get a more detailed picture of the deviations from the log law. We note that stronger stratification (larger values of $|h/L_0|$) corresponds to larger deviation from the log law. Further, the deviated MVPs are qualitatively different for unstable and stable stratification—for unstable stratification, the MVPs flatten with increase in $\tilde{y}$, while for stable stratification, the MVPs steepen with increase in $\tilde{y}$. These trends continue as we move past the intermediate region and get closer to the centerline. Moving closer to the wall from the intermediate region, we note that the MVPs for flows whose stratification is not very strong collapse onto the MVP for wall-bounded turbulent flows of constant-density fluids—with a viscous layer next to the wall (with $\tilde{u} = \tilde{y}$) that is topped with a buffer layer (Fig. 4.1). That is, the near-wall flow obeys the "law of the wall" for wall-bounded turbulent flows of constant-density fluids (Tennekes & Lumley, 1972; Pope, 2000). When the stratification becomes strong, the MVPs begin to deviate from the collapsed curve in the buffer layer.

Above we have outlined the salient qualitative features of MVPs in thermally-stratified turbulent flows. There exists no theory that sheds light on the origin of these features. Next, using the framework of the spectral theory discussed in Chapter 2, we seek to understand these features.

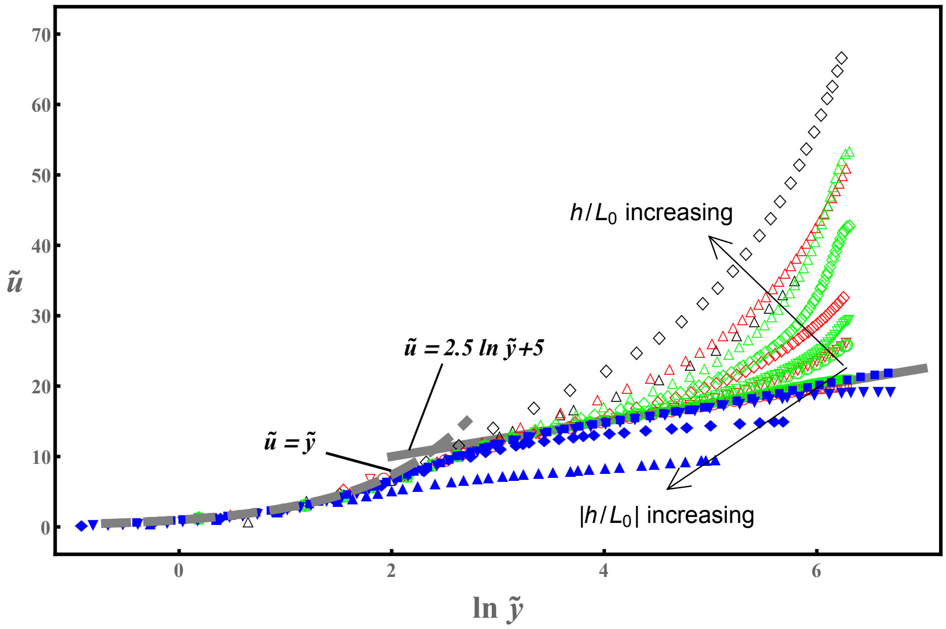

Fig. 4.1: Log-linear plot of the MVPs in the "wall variables", $\tilde{u}$ vs. $\tilde{y}$. Filled symbols are DNS data for unstably-stratified channel flows from Pirozzoli *et al.* (2017) with $Pr = 1$: upward-pointing triangles denote $h/L_0 = -12.04, \mathrm{Re}_\tau = 179$, diamonds denote $h/L_0 = -1.47, \mathrm{Re}_\tau = 351$, downward-pointing triangles denote $h/L_0 = -0.18, \mathrm{Re}_\tau = 864$, and squares denote $h/L_0 = 0, \mathrm{Re}_\tau = 816$. Empty symbols are DNS data for stably-stratified flows. Green data are for stably-stratified channel flows from García-Villalba & del Álamo (2011) with $Pr = 0.7, \mathrm{Re}_\tau = 550$: squares denote $h/L_0 = 0$, circles denote $h/L_0 = 0.22$, downward-pointing triangles denote $h/L_0 = 0.34$, diamonds denote $h/L_0 = 0.84$, and upward-pointing triangles denote $h/L_0 = 1.36$. Red data are for stably-stratified plane Couette flow from García-Villalba *et al.* (2011) (in this case h/L_0 can not be computed from the data provided in this paper) with $Pr = 0.7, \mathrm{Re}_\tau = 540$: circles denote $Ri_b = 0$, downward-pointing triangles denote $Ri_b = 0.03$, diamonds denote $Ri_b = 0.06$, and upward-pointing triangles denote $Ri_b = 0.1$. Black data are for stably-stratified plane Couette flow from Deusebio *et al.* (2015) with $Pr = 0.7$: upward-pointing triangles denote $h/L_0 = 1.37, \mathrm{Re}_\tau = 349$, diamonds denote $h/L_0 = 3.78, \mathrm{Re}_\tau = 520$.

4.4 Mean-velocity profile: spectral theory

4.4.1 Mean-flow equations

To guide the theory of MVP, we first list the governing equations for the mean flow. Invoking Reynolds's decomposition, we split the instantaneous flow as:

$$\begin{aligned} \boldsymbol{u} &= \overline{\boldsymbol{u}} + \boldsymbol{u'}; \\ p &= \overline{p} + p'; \\ T &= \overline{T} + T'; \\ \rho &= \overline{\rho} + \rho', \end{aligned}$$

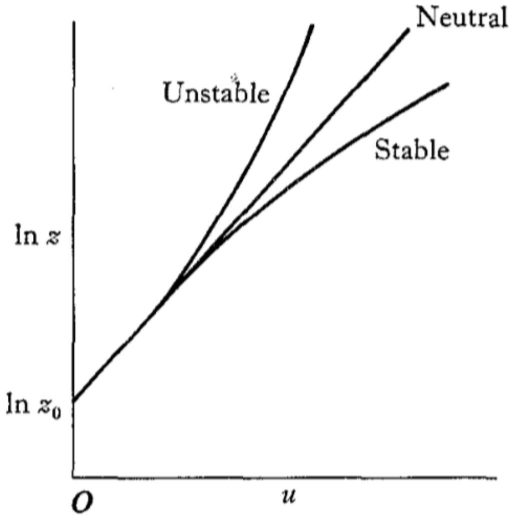

Fig. 5.2. The effect of a stable or unstable environment on turbulent velocity profiles.

Fig. 4.2: Deviation from the log law due to unstable and stable stratification. Figure from the classic textbook Turner (1973). Note that compared with Fig. 4.1, the axes are flipped. Also note that here the distance from the wall is denoted by z.

where the first term on the right-hand side is the time-averaged mean component and the second term is the fluctuating component (and is marked with a prime). For a fully-developed, plane Couette flow, we note that the mean flow is steady ($\partial()/\partial t = 0$), the mean velocity is unidirectional ($\boldsymbol{u} = (u, 0, 0)$), the mean pressure gradient is absent ($\boldsymbol{\nabla}\bar{p} = \boldsymbol{0}$), and the streamwise and the spanwise gradients are absent ($\partial()/\partial x = 0$ and $\partial()/\partial z = 0$, respectively). Under these simplifications and by substituting Reynolds's decomposition in the governing equations for Boussinesq approximation (see Equations 4.2–4.4), we arrive at the following governing equations for the mean flow (see Kundu & Cohen (2002)).

The equation for the conservation of mass for incompressible fluid reads:

$$\boldsymbol{\nabla} \cdot \boldsymbol{u} = 0, \tag{4.8}$$

which is automatically satisfied for a plane Couette flow since $\boldsymbol{\nabla} \cdot \boldsymbol{u} = \partial u/\partial x = 0$.

The equation for the conservation of mean momentum (streamwise component) reads:

$$0 = \nu \frac{\partial^2 u}{\partial y^2} + \frac{\partial \tau_t}{\partial y}, \tag{4.9}$$

where τ_t is the turbulent shear stress; $\tau_t \equiv -\rho\langle u'v'\rangle$, where the angle brackets denote an ensemble average, u' is the fluctuating velocity in the streamwise direction and v' is the fluctuating velocity in the wall-normal direction. Note that the buoyant term acts in the wall-normal direction and thus does not appear in the streamwise momentum equation. That is, the equation for the streamwise mean momentum is the same as that in wall-bounded turbulent flows of constant-density fluids. Integrating in y, we obtain the equation for momentum balance (which is the same as discussed in Appendix A for unstratified plane Couette flow):

$$\tau_0 = \rho\nu\frac{du}{dy} + \tau_t. \tag{4.10}$$

From conservation of momentum, we can also derive an equation for the mean kinetic energy (Kundu & Cohen, 2002), from which equation of energy balance reads:

$$\varepsilon = \tau_t\frac{du}{dy}/\rho + g\alpha H_s, \tag{4.11}$$

where ε is the turbulent power per unit mass, which is balanced by $\tau_t\frac{du}{dy}/\rho$ (the shear production of turbulent kinetic energy) and $g\alpha H_s$ (the buoyant production of turbulent kinetic energy; H_s is the turbulent heat flux; $H_s \equiv \langle v'T'\rangle$). Here, as discussed in Appendix B, we neglect the transport terms in deriving the equation for energy balance. Note that unlike the equation for streamwise mean momentum (Equation 4.9), which is unaffected by buoyancy, the energy balance includes contributions from wall-normal mean momentum and thus is affected by buoyancy.

Finally, the heat equation reads:

$$H_0 = -k_d\frac{dT}{dy} + H_s. \tag{4.12}$$

In the following analysis, we shall invoke Equations 4.10–4.12. Specifically, the heat equation provides a constraint for H_s, which, in turn, determines the buoyant production in the energy balance. The MVP is determined by solving the equations of momentum balance and energy balance. Since the momentum balance is unaffected by stratification, the effect of stratification is only determined by the buoyant production term in the energy balance. For later reference we note that in the region where the shear production dominates over the buoyant production, the equation of energy balance is the same as that for wall-bounded turbulent flows of constant-density fluids. Thus, in this region, the MVP will remain unaffected by the stratification.

4.4.2 Spectral link

The nub of the theoretical framework of the spectral theory (Gioia *et al.*, 2010) is the expression for the turbulent shear stress τ_t at a distance y from the wall:

$$\tau_t = \kappa_\tau\rho y v_y\frac{du}{dy}, \tag{4.13}$$

where κ_τ is a dimensionless proportionality constant and v_y is the characteristic velocity of a turbulent eddy of the size y. This expression (spectral link) links τ_t to the turbulent kinetic energy spectrum, $E(k)$, via v_y—recall that the characteristic velocity v_s of a turbulent eddy of size s can be determined from $E(k)$ using $v_s = \sqrt{\int_{1/s}^{\infty} E(k)dk}$. By substituting the standard model of the spectrum (Pope, 2000):

$$E(k) \equiv \frac{2}{3}((\kappa_\varepsilon\varepsilon)^{2/3}k^{-5/3}\exp(-\beta_d\eta k)(1+(\beta_e/kh)^2)^{-17/6},$$

and introducing the dimensionless variable $\xi \equiv sk$, we can write:

$$v_s = (\kappa_\varepsilon \varepsilon s)^{1/3}\sqrt{I},$$

where $I \equiv I(\eta/s, s/h) \equiv \frac{2}{3}\int_1^\infty \xi^{-5/3}\exp(-\xi\beta_d\eta/s)(1+(\beta_e s/h)^2/\xi^2)^{-17/6}d\xi$. Here, κ_ε is a dimensionless constant of order 1, ε is the turbulent power per unit mass, η is the viscous lengthscale (which can be computed as $\eta = \nu^{3/4}(\kappa_\varepsilon\varepsilon)^{-1/4}$), $\exp(-\xi\beta_d\eta/s)$ is the dissipative-range correction, β_d is the non-negative dimensionless parameter of the dissipative-range correction), $(1+(\beta_e s/h)^2/\xi^2)^{-17/6}$ is the Kármán form of the energetic-range correction, and β_e is the non-negative dimensionless parameter of the energetic-range correction. In general, for an eddy of size s in the inertial range ($\eta \ll s \ll h$), $I = 1$ and $v_s = (\kappa_\varepsilon\varepsilon s)^{1/3}$. For an eddy of size s in the dissipative range ($s \sim \eta$) or the energetic range ($s \sim h$), $I < 1$ and $v_s < (\kappa_\varepsilon\varepsilon s)^{1/3}$. If we set $\beta_d = \beta_e = 0$—that is, if there is no dissipative-range correction and no energetic-range correction (an unphysical proposition)—$v_s = (\kappa_\varepsilon\varepsilon s)^{1/3}$ for all s, and all eddies are inertial. Previous studies of adapting the spectral theory for thermally-stratified flows in the atmosphere restricted attention to such inertial eddies and to the intermediate region of the MVP, see, e.g., (Katul *et al.*, 2011). Here we consider the whole structure of $E(k)$ as well as the whole extent of the MVP.

As in Chapter 2, we seek to obtain the MVP by solving the equation of momentum balance (Equation 4.10), where τ_t is given by Equation 4.13. In Equation 4.13, v_y is related to $E(k)$, which varies with y through the dependence of ε with y, which, in turn, is governed by the energy equation (Equation 4.11). With the additional contribution from buoyant production, this energy equation is the main difference from our analysis in Chapter 2.

To proceed, we first obtain a simpler form of the energy equation. To that end, consider the heat equation (Equation 4.12): $H_0 = -k_d\frac{dT}{dy} + H_s$. The term $-k_d\frac{dT}{dy}$ represents molecular diffusion of heat and the term H_s represents turbulent diffusion of heat. Due to the no-penetration boundary condition at the wall, we have $v' = 0$ and therefore $H_s = 0$. Thus, at the wall, molecular diffusion of heat dominates the heat flux. Away from the near-wall region, the heat flux is dominated by H_s. These considerations are analogous to molecular and turbulent diffusion of momentum flux, as can be seen by comparing the heat equation (Equation 4.12) with the equation of momentum balance (Equation 4.10). From the perspective of energy balance, however, considerations of heat flux and momentum flux in the near-wall region are distinct. In this region, shear production dominates over buoyant production (Equation 4.11). (Recall that in the near-wall region, y is much smaller than L_0, the Obukhov length, which characterizes the distance from the wall at which turbulence effected by shear and buoyancy are comparable.) Thus, if we neglect the molecular diffusion of heat in the heat equation, the energy balance remains largely unaltered. We therefore simplify the heat equation as $H_0 = H_s$, which leads to the following simplified equation for the energy balance:

$$\varepsilon = \tau_t\frac{du}{dy}/\rho + g\alpha H_0. \tag{4.14}$$

Before proceeding with the analysis we note that because we have neglected molecular diffusion of heat from our analysis, our predictions for MVPs do not depend on the Prandtl number, Pr. (By contrast, the mean-temperature profile depends on Pr.) Neglecting the molecular diffusion of heat near the wall is valid as long as the thermal boundary layer is smaller than or of comparable size as the momentum boundary layer. In other words, we focus attention to flows where $Pr \sim O(1)$ (such as flows in the atmospheric boundary layer) or larger and do not consider flows where $Pr \ll 1$. For such flows ($Pr \gtrsim O(1)$), we predict that the MVPs only depend on two dimensionless parameters, Re_τ and h/L_0, independent of Pr.

Returning to the analysis, we combine Equations 4.13 to 4.14 and express the results in the wall variables to obtain:

$$\tilde{u}'\kappa^{4/3}\tilde{y}^{4/3}(\tilde{u}' - \tilde{u}'^2 - h/(\mathrm{Re}_\tau \kappa L_0))^{1/3}\sqrt{I} + \tilde{u}' = 1, \tag{4.15}$$

where $\tilde{u}' \equiv d\tilde{u}/d\tilde{y}$. Solving this equation will yield the MVP.

To obtain the MVP, following the analysis of Chapter 2, we first determine the thickness of the viscous layer, $\tilde{y}_v$. To that end, from Equations 4.14 and 4.15 and the relation $\eta = \nu^{3/4}\varepsilon^{-1/4}$, we obtain:

$$\eta/y = (\tilde{u}' - \tilde{u}'^2 - h/(\mathrm{Re}_\tau \kappa L_0))^{-1/4}\tilde{y}^{-1}. \tag{4.16}$$

Next we introduce further simplification. In the region adjacent to the wall, we neglect the buoyant production in comparison with shear production, in accord with the discussion above. (We shall return to this assumption later in this section.) That is, for $y \ll h$, we assume $-h/(\mathrm{Re}_\tau \kappa L_0) \ll \tilde{u}' - \tilde{u}'^2$. Under this simplification, we can eliminate $\tilde{u}'$ from Equations 4.15 and 4.16 to obtain:

$$\tilde{y} = \left(\frac{(\eta/y)^{4/3} + \kappa^{4/3}I^{1/2}(\eta/y, 0)}{\kappa^{2/3}(\eta/y)^{8/3}I^{1/4}(\eta/y, 0)}\right)^{1/2}, \tag{4.17}$$

which allows us to determine $\tilde{y}_v$, the thickness of the viscous layer, in the same way as discussed in Chapter 2.

We are now ready to compute the MVP. For $\tilde{y} \leq \tilde{y}_v$, the flow is purely viscous and $\tilde{u}(\tilde{y}) = \tilde{y}$. For $\tilde{y} > \tilde{y}_v$, we integrate Equation 4.15, where we use the boundary condition on top of the viscous layer: $\tilde{u}(\tilde{y}_v) = \tilde{y}_v$. Setting $\beta_d = 5.2$ and $\kappa = 0.4$ (which yields $\tilde{y}_v = 3.41$), and $\beta_e = 2$, in Fig. 4.3, we plot the theoretical predictions for the MVPs in wall variables for a fixed Re_τ and for various values of h/L_0 spanning unstable and stable stratification. The predicted MVPs are in excellent qualitative accord with empirical data (Fig. 4.1). Next we discuss the salient features of the predicted MVPs, starting at the wall and moving outward.

Near the wall, the MVPs for unstably-stratified flows, stably-stratified flows, and flows of constant-density fluids collapse onto a single curve, confirming the law of the wall. This collapsed curve spans the viscous layer and part of the buffer layer. First, consider the viscous layer. In computing $\tilde{y}_v$ (see Equation 4.17), we have neglected buoyant production, and thus stratification does not affect the MVP in the viscous layer. In the buffer layer, however, effects of both buoyant production and shear production are taken into account. As the stratification becomes strong, which corresponds to larger values of $|h/L_0|$, the region where the buoyant production can be neglected moves closer to the wall. Thus, the extent of the collapsed MVPs becomes smaller,

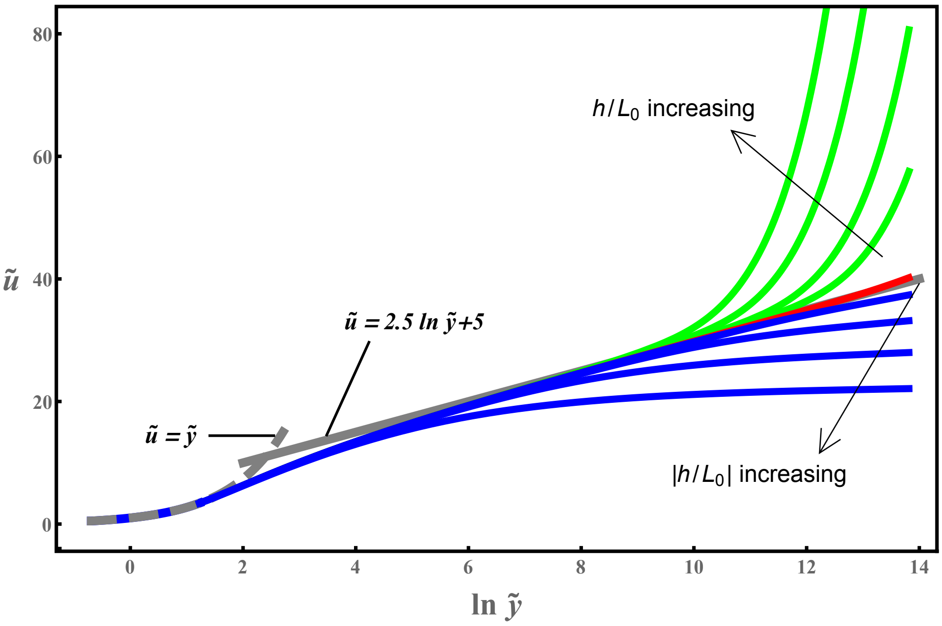

Fig. 4.3: Log-linear plots of theoretically-predicted MVPs in wall variables. The MVPs correspond to a fixed $\mathrm{Re}_\tau = 10^6$ and various values of h/L_0. The red line corresponds to the flow of constant-density fluids with $h/L_0 = 0$; the blue lines correspond to unstably-stratified flows with $h/L_0 = -10, -100, -1000, -10000$; and the green lines correspond to stably-stratified flows with $h/L_0 = 10, 20, 50, 100$. As the absolute value of h/L_0 increases, the MVPs deviate more from the flow of constant-density fluids. For computing the curves using the spectral theory, we set $\kappa = 0.4$, $\beta_e = 2$, and $\beta_d = 5.2$.

creeping closer to the top of the viscous layer. Note, however, that even for the very strong unstably stratified flow with $h/L_0 = -10000$, there is still a small region of collapsed MVP in the buffer layer. That is, for all the cases we have considered, the effect of stratification starts at some distance away from the viscous layer, thereby providing an *a posteriori* justification for neglecting buoyant production in computing the thickness of the viscous layer.

When the stratification is not very strong, we see a clear log layer topping the buffer layer. The log layer becomes thinner and thinner as the stratification becomes stronger and stronger. Finally, for very strong stratification, the log layer disappears.

Beyond the log layer, unstable stratification flattens the MVPs whilst stable stratification steepens the MVPs. By contrast, the MVP for the flow of constant-density fluids continues to inhabit the log layer. These signature features of unstable stratification and stable stratification can be understood through the spectral theory. When the flow is unstably stratified, the buoyant production term is positive and ε is larger compared with its counterpart for the flow of constant-density fluids. As such, unstable stratification accelerates the turbulent eddies (v_s becomes larger), which makes them more effective at transferring momentum and producing turbulent shear stress. Thus, the turbulent shear stress heightens according to Equation 4.13 and, consequently, the mean velocity decreases. This decrease in mean velocity manifests as a flattening of the MVP compared with the log law. By contrast, when the flow is stably stratified, the buoyant production term is negative and thus ε is smaller compared with its counterpart for the flow of constant-density fluids. As such, stable stratification slows down the turbulent eddies (v_s becomes smaller), which makes them less effective at transferring momentum and producing turbulent shear stress. Thus, the turbulent shear stress lessens according to Equation 4.13 and, consequently, the mean velocity increases. This increase in mean velocity manifests as a steepening of the MVP compared with log law.

4.4.3 The effect of the energetic-range correction

Here we consider how the energetic-range correction, which we parameterize using β_e, affects the MVPs. Similar to Fig. 4.3, in Fig. 4.4 we plot the theoretical predictions for the MVPs in wall variables for a fixed Re_τ and for various values of h/L_0 spanning unstable and stable stratification. Unlike Fig. 4.3, however, here we compute the MVPs using two values of β_e: $\beta_e = 1$ and $\beta_e = 7$, which we plot using solid and dashed curves, respectively. Comparing the solid and dashed curves we note that the energetic-range correction has only a minor effect on the MVPs. In fact, for stable stratification, the energetic-range correction has no effect on the MVPs when the stratification is strong. For example, for $h/L_0 = 20$, the solid and dashed curves overlap with each other, as can be seen in Fig. 4.4. This behavior can be understood by considering Equations 4.10 and 4.15.

In the region far from the wall, the viscous shear stress in Equation 4.10 can be ignored compared with the turbulent shear stress. Therefore, Equation 4.15 can be written as:

$$\tilde{u}'\kappa^{4/3}\tilde{y}^{4/3}(\tilde{u}' - h/(\mathrm{Re}_\tau\kappa L_0))^{1/3}\sqrt{I} = 1. \tag{4.18}$$

We can rewrite Equation 4.18 as:

$$\tilde{u}' - h/(\mathrm{Re}_\tau\kappa L_0) = \frac{I^{-3/2}}{\tilde{u}'^3\kappa^4\tilde{y}^4}. \tag{4.19}$$

For strong stable stratification, we can expect that the right-hand side of Equation 4.19 will be negligibly small as the values of both $\tilde{u}'$ and $\tilde{y}$ are large in the region far from the wall. Thus Equation 4.19 reduces to $\tilde{u}' = h/(\mathrm{Re}_\tau\kappa L_0)$, which is independent of the energetic-range correction.

4.5 Generalized Monin-Obukhov similarity theory

Having discussed empirical data and spectral theory for the whole extent of the MVP, next we seek to generalize the framework of MOST to extend it beyond the intermediate region for which it was originally formulated and encompass the whole MVP (see Section 4.2).

Shifting attention from MVP in wall variables, $\tilde{u}$ vs. $\tilde{y}$, we return to the dimensionless function that is the main concern of MOST, ϕ_u. (We discuss scaling of the MVP in Section 4.5.3.) From Equation 4.6, ϕ_u can be expressed as a dimensionless measure of the gradient of MVP:

$$\phi_u = \kappa\tilde{y}\frac{d\tilde{u}}{d\tilde{y}}. \tag{4.20}$$

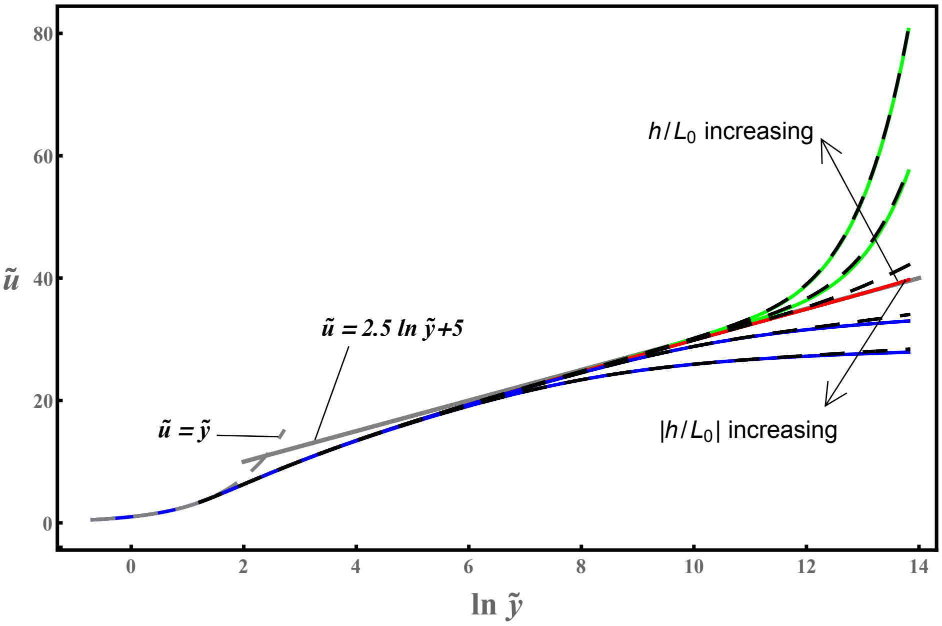

Fig. 4.4: Log-linear plots of theoretically-predicted MVPs in wall variables. The MVPs correspond to a fixed $\mathrm{Re}_\tau = 10^6$ and various values of h/L_0. The red line corresponds to the flow of constant-density fluids with $h/L_0 = 0$; the blue lines correspond to unstably-stratified flows with $h/L_0 = -100, -1000,$; and the green lines correspond to stably-stratified flows with $h/L_0 = 10, 20$. As the absolute value of h/L_0 increases, the MVPs deviate more from the flow of constant-density fluids. For computing the curves using the spectral theory, we set $\kappa = 0.4, \beta_d = 5.2,$and $\beta_e = 1$. To see the effect of the energetic-range correction, the dashed black curves are computed with the same values of κ and β_d, but with $\beta_e = 7$.

Note that the prediction of MOST that ϕ_u is only a function of y/L_0 (see Equation 4.6) is only valid for the intermediate region of y/L_0. In general, ϕ_u not only depends on y/L_0 but also on Re_τ and h/L_0. This can be seen using the framework of the spectral theory—in Fig. 4.5, we plot predicted ϕ_u vs. y/L_0 for a fixed Re_τ and for various values of h/L_0 spanning unstable and stable stratification. For the intermediate region of y/L_0, the different MVPs collapse onto one curve, in accord with the prediction of MOST. (Note that MOST does not predict the shape of this collapsed curve.) Outside of this region, however, the functional dependence predicted by MOST breaks down.

The reasons for this break down can be understood by considering the assumptions that guide MOST. Specifically, as we have noted in Section 4.2, in MOST attention is restricted to an intermediate region that is not too close to the wall where viscosity affects the flow and not too far from the wall where external confinement affects the flow. This allows one to neglect the effects of ν (which encapsulates molecular diffusion of momentum near the wall), k_d (which encapsulates molecular diffusion of heat near the wall), and h (which encapsulates external confinement). To generalize MOST, we account for these effects. To that end, we seek guidance from the classic scaling laws of the MVP in wall-bounded turbulent flows of constant-density fluids.

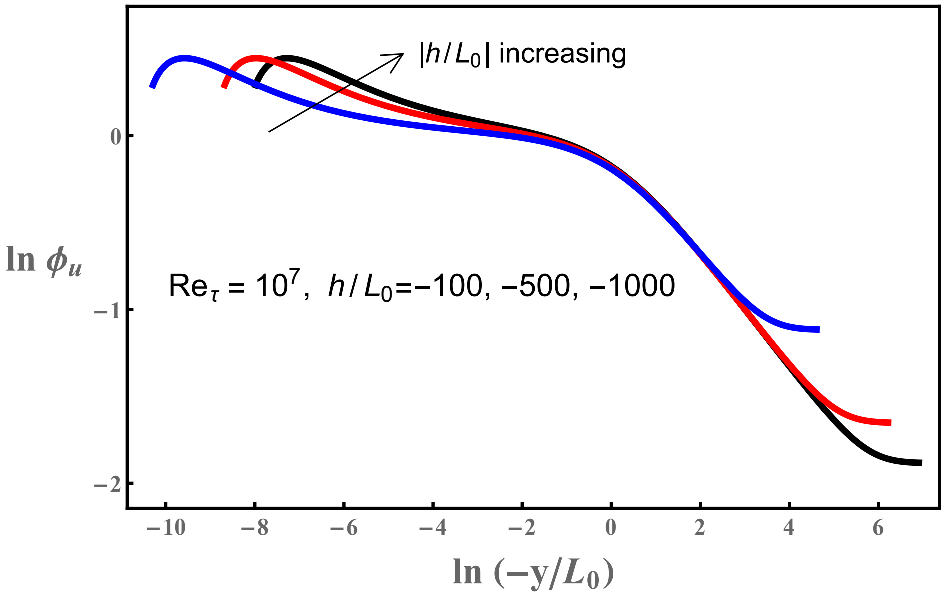

(a)

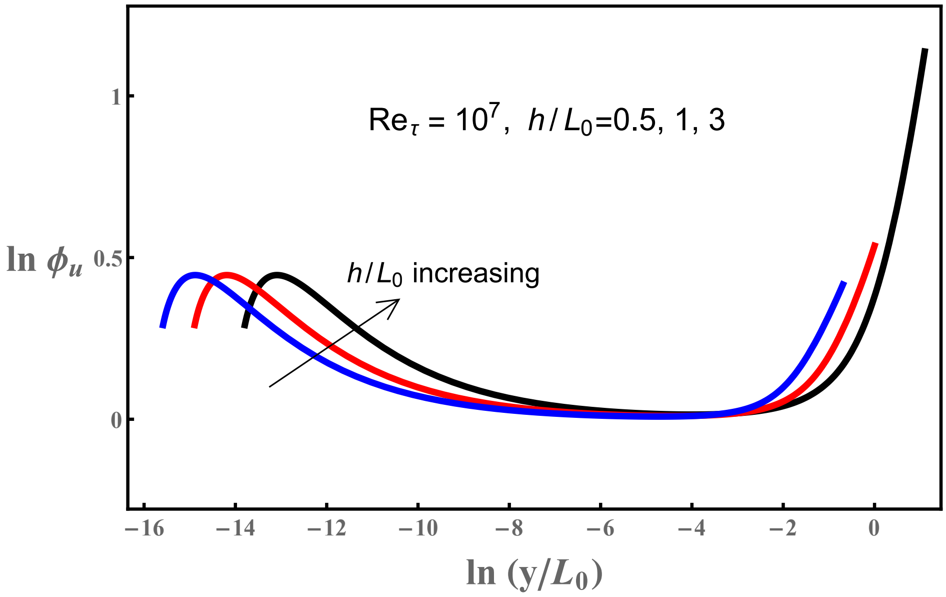

(b)

Fig. 4.5: Log-log plots of ϕ_u vs y/L_0 for: (a) unstable stratification, and (b) stable stratification. For computing the curves using the spectral theory, we set $\kappa = 0.4, \beta_e = 2$, and $\beta_d = 5.2$.

4.5.1 Classic scaling laws for MVP

For reference, next we outline the key elements of deriving the classic scaling laws, in wall-bounded turbulent flows of constant-density fluids, for the MVP: the law of the wall, the log law, and the defect law. We consider the case of a fully developed, plane Couette flow of constant-density fluids. Our discussion closely follows the approach of Zuniga Zamalloa *et al.* (2014).

The starting point for deriving the classic scaling laws is dimensional analysis, wherein the vertical gradient of the MVP, $\frac{du}{dy}$, is posited to depend on:

$$\frac{du}{dy} = G_1(y, h, \tau_0, \rho, \nu), \tag{4.21}$$

where G_1 is an unspecified function. Using the Buckingham–Pi theorem, the functional relation between these six dimensional variables can be expressed as an equivalent functional relationship between three dimensionless variables:

$$\frac{du}{dy}\frac{y}{u_\tau} = \phi\left(\tilde{y}, \frac{y}{h}\right), \tag{4.22}$$

where ϕ is a dimensionless function whose functional form is unspecified. Hereafter, for brevity, we do not explicitly mention that the ϕ-like functions are dimensionless functions with unspecified functional forms. Equation 4.22 can be expressed in an equivalent form as:

$$\frac{du}{dy}\frac{y}{u_\tau} = \tilde{\phi}\left(\tilde{y}, Re_\tau\right), \tag{4.23}$$

or as:

$$\frac{du}{dy}\frac{y}{u_\tau} = \tilde{\tilde{\phi}}\left(\frac{y}{h}, Re_\tau\right). \tag{4.24}$$

In writing these equations, we are invoking the notion that any combinations of the dimensionless variables yield equivalent expressions of the functional dependence. Thus, for example, Re_τ can be written as $\tilde{y}/(y/h)$, which leads to Equation 4.23 or 4.24 from Equation 4.22. Equations 4.23 and 4.24 imply that the dimensionless du/dy depends on two independent variables: $\tilde{y}$ and Re_τ, or y/h and Re_τ. Thus, for example, if we plot the dimensionless du/dy vs. $\tilde{y}$, the curves for different values of Re_τ will be distinct. In what follows, we seek to collapse these distinct curves onto one curve. It turns out that it is not possible to have a single collapsed curve that spans the whole domain of the flow. Instead, we will have collapsed curves that correspond to different regions of $\tilde{y}$ and y/h. To that end, we need to go beyond dimensional analysis and invoke complete similarity for asymptotic limits of $\tilde{y}$ and y/h. Next, we define complete similarity (Barenblatt, 1996).

For a dimensionless function $A(a_1, ..., a_N)$, where A depends on N dimensionless variables a_1 to a_N, if A obeys complete similarity with respect to a dimensionless variable a_i, then for an asymptotic limit of that variable, $a_i \to 0$ (or $a_i \to \infty$), we can write:

$$\lim_{a_i \to 0 \text{ (or } a_i \to \infty)} A(a_1, ..., a_N) = A_1(a_1, ..., a_{i-1}, a_{i+1}, ...a_N).$$

That is, in the asymptotic limit of a_i, A no longer depends on the value of a_i.

We first consider the region near the wall: $y/h \to 0$ (the "inner layer"). Assuming that ϕ obeys complete similarity in y/h for this limit, Equation 4.22 can be written as

$$\frac{du}{dy}\frac{y}{u_\tau} = \phi_1\left(\tilde{y}\right). \tag{4.25}$$

That is, the curves of the dimensionless du/dy vs. $\tilde{y}$ for various values of Re_τ should collapse onto one curve in the inner layer. Integrating Equation 4.25 in $\tilde{y}$, yields the law of the wall:

$$\tilde{u} = I_0(\tilde{y}), \tag{4.26}$$

where $I_0(x) \equiv \int_0^x \xi^{-1}\phi_1(\xi)d\xi$ and we have used the no-slip boundary condition $\tilde{u}(\tilde{y} = 0) = 0$. Per the law of the wall, the curves of $\tilde{u}$ vs. $\tilde{y}$ for various values of Re_τ should collapse onto one curve in the inner layer. Note that although the law of the wall is derived for the asymptotic limit of $y/h \to 0$, in practice this law holds over a finite layer $y/h \lesssim 0.1$ (Pope, 2000).

Next, for flows at large Re_τ, consider the region far from the wall, closer to the centerline: $\tilde{y} \to \infty$ (the "outer layer"). (Here we need to consider large Re_τ because the largest value of $\tilde{y}$, which is at the centerline, is Re_τ.) Assuming that ϕ obeys complete similarity in $\tilde{y}$ for this limit, Equation 4.22 can be written as

$$\frac{du}{dy}\frac{y}{u_\tau} = \phi_2\left(\frac{y}{h}\right), \tag{4.27}$$

which, after integration in y/h, yields the defect law:

$$\tilde{u}(y = h) - \tilde{u} = O\left(\frac{y}{h}\right), \tag{4.28}$$

where $O(x) \equiv \int_x^1 \xi^{-1}\phi_2(\xi)d\xi$. Note that although the defect law is derived for the asymptotic limit of $\tilde{y} \to \infty$, in practice this law holds over a finite region $\tilde{y} \gtrsim 50$ (Pope, 2000).

Last, for flows at large Re_τ, consider the region at intermediate distance from the wall: $y/h \to 0$ and $\tilde{y} \to \infty$ (the "log layer"). Assuming that ϕ obeys complete similarity in y/h and $\tilde{y}$ for these limits, Equation 4.22 can be written as:

$$\frac{du}{dy}\frac{y}{u_\tau} = \frac{1}{\kappa}, \tag{4.29}$$

where the "Kármán constant" κ obeys:

$$\frac{1}{\kappa} = \lim_{\tilde{y}\to\infty \text{ and } y/h\to 0} \phi\left(\tilde{y}, \frac{y}{h}\right).$$

Integrating Equation 4.29 in $\tilde{y}$ yields the log law (Equation 4.7), which, in practice, holds for $\tilde{y} \gtrsim 30$ and $y/h \lesssim 0.3$ (Pope, 2000).

In deriving the classic scaling laws, we first derived scaling laws for du/dy, which we integrated to derive scaling laws for the MVP. These laws allow us to collapse the MVPs for different values of Re_τ onto one curve for different regions of $\tilde{y}$ and y/h. Next, for thermally-stratified flows, we first derive scaling laws for du/dy and then, in Section 4.5.3, we derive scaling laws for the MVP.

4.5.2 Scaling laws for ϕ_u

We now turn to deriving generalized scaling laws for du/dy in thermally-stratified plane Couette flows. Like MOST and the classic scaling laws discussed above, our starting point is dimensional analysis. We posit that $\frac{du}{dy}$ depends on:

$$\frac{du}{dy} = G_2(y, \tau_0, \rho, g, \alpha, H_0, \nu, h), \tag{4.30}$$

where G_2 is an unspecified function. Compared with the analysis of MOST (see Equation 4.5), here we have two additional variables: ν and h. Analogous to deriving the classic scaling laws (see Equation 4.21), these variables allow us to go beyond the intermediate region of interest in MOST, and cover the whole MVP. We now follow the same steps as we did starting with Equation 4.21.

Using the Buckingham–Pi theorem, the functional relation between these nine dimensional variables of Equation 4.30 can be expressed as an equivalent functional relationship between four dimensionless variables:

$$\phi_u = \frac{du}{dy}\frac{\kappa y}{u_\tau} = \phi_{u1}\left(\frac{y}{L_0}, \tilde{y}, \frac{y}{h}\right). \tag{4.31}$$

Compared with Equation 4.6, we have two additional dimensionless variables, $\tilde{y}$ and y/h, which show the direct analogy with Equation 4.22. Next we invoke complete similarity in these variables.

In the region near the wall, assuming that ϕ_{u1} obeys complete similarity for $y/h \to 0$, Equation 4.31 can be written as:

$$\phi_u = \phi_{u2}\left(\frac{y}{L_0}, \tilde{y}\right), \tag{4.32}$$

which can be expressed in an equivalent form as:

$$\phi_u = \phi_{u3}\left(\frac{y}{L_0}, \mathrm{Re}_{L_0}\right), \tag{4.33}$$

where $\mathrm{Re}_{L_0} \equiv u_\tau L_0/\nu$. We call Equation 4.33 "generalized MOST for the inner layer". To test the validity of this equation, using the spectral theory, in Fig. 4.6, we plot ϕ_u vs. y/L_0 for a *fixed* Re_{L_0} and for various values of h/L_0. Per Equation 4.33, in the inner layer and for a fixed Re_{L_0}, ϕ_u only depends on y/L_0, and thus the curves corresponding to different h/L_0 should collapse onto one curve. This prediction is in excellent accord with the results from the spectral theory for both unstably-stratified flows and stably-stratified flows (see Fig. 4.6).

At first glance, the trends in Fig. 4.6 for increasing values of $|h/L_0|$ might appear puzzling. In previous figures, the region of collapse has systematically lessened with increase in $|h/L_0|$. Here, by contrast, the region of collapse increases with increase in $|h/L_0|$. To understand why that is the case, consider the extent of the inner layer. As noted earlier in discussing the law of the wall, although the law is derived for the asymptotic limit of $y/h \to 0$, in practice it holds over a finite region $y/h \lesssim 0.1$. Here, let us denote this finite region by $y/h \lesssim \epsilon_i$, where $0 < \epsilon_i \ll 1$. Now, $y/h \lesssim \epsilon_i$ can be written as:

$$\frac{y}{L_0} \lesssim \epsilon_i \left|\frac{h}{L_0}\right|. \tag{4.34}$$

That is, the extent of the inner layer increases with increase in $|h/L_0|$.

For a complementary perspective on why the region of collapse increases with increase in $|h/L_0|$, we draw attention to a well-known feature of wall-bounded turbulent flows of constant-density fluids. For such flows, the region of collapsed MVPs (that is, the region where the MVPs follow the classic scaling laws discussed earlier) increases

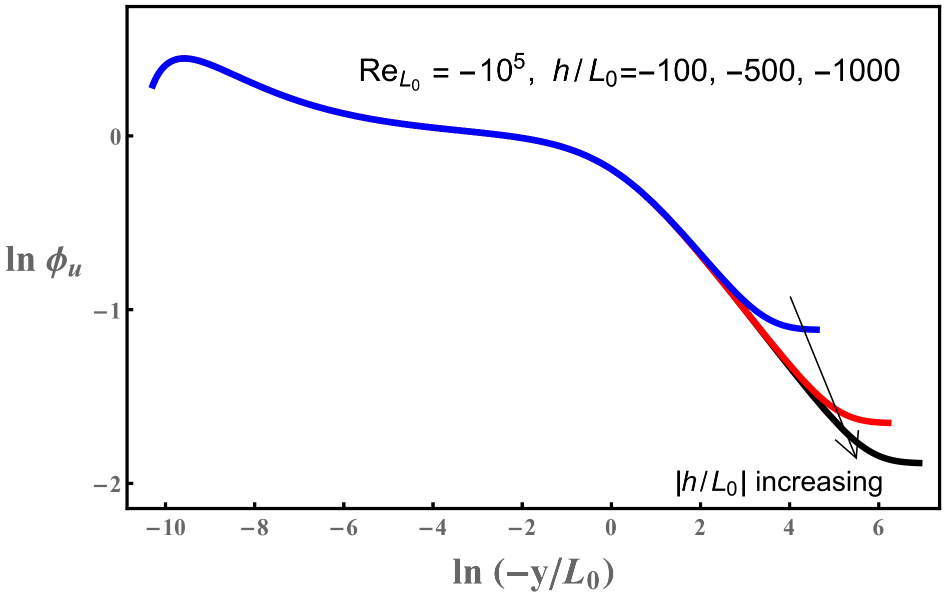

(a)

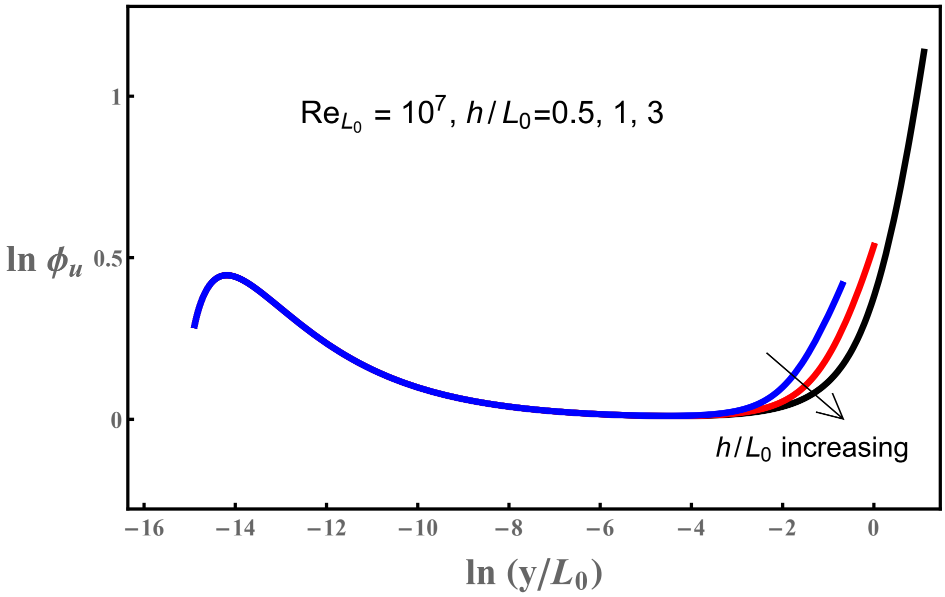

(b)

Fig. 4.6: Testing the generalized MOST for the inner layer. Log-log plots of ϕ_u vs. y/L_0 for: (a) unstable stratification, (b) stable stratification. Note the collapsed curves near the wall. For computing the curves using the spectral theory, we set $\kappa = 0.4, \beta_e = 2$, and $\beta_d = 5.2$.

with increase in Re_τ. Now, consider the ratio of Re_τ and Re_{L_0}. From their respective definitions:

$$\frac{\mathrm{Re}_\tau}{|\mathrm{Re}_{L_0}|} = |\frac{h}{L_0}|. \tag{4.35}$$

For a fixed Re_{L_0}, as is needed for the generalized MOST for the inner layer, an increase in $|h/L_0|$ corresponds to an attendant increase in Re_τ. That is, the curves in Fig. 4.6 that correspond increasing values of $|h/L_0|$ also correspond to increasing values of Re_τ.

In the region far from the wall and for flows at large Re_τ, assuming that ϕ_{u1} obeys complete similarity for $\tilde{y} \to \infty$, Equation 4.31 can be written as:

$$\phi_u = \phi_{u4}\left(\frac{y}{L_0}, \frac{y}{h}\right), \tag{4.36}$$

which can be expressed in an equivalent form as:

$$\phi_u = \phi_{u5}\left(\frac{y}{L_0}, \frac{h}{L_0}\right). \tag{4.37}$$

We call Equation 4.37 "generalized MOST for the outer layer". To test the validity of this equation, using the spectral theory, in Fig. 4.7, we plot ϕ_u vs. y/L_0 for a *fixed* h/L_0 and for various values of Re_{L_0}. Per Equation 4.37, in the outer layer and for a fixed h/L_0, ϕ_u only depends on y/L_0, and thus the curves corresponding to different Re_{L_0} should collapse onto one curve. This prediction is in excellent accord with the results from the spectral theory for both unstably-stratified flows and stably-stratified flows (see Fig. 4.7).

A note on the trends in Fig. 4.7 with increasing values of $|\mathrm{Re}_{L_0}|$ is in order. The region of collapse increases with increase in $|\mathrm{Re}_{L_0}|$. To understand why, consider the extent of the outer layer. As noted earlier in discussing the defect law, although the law is derived for the asymptotic limit of $\tilde{y} \to \infty$, in practice it holds over a finite region $\tilde{y} \gtrsim 50$. Here, let us denote this finite region by $\tilde{y} \gtrsim \Delta_o$, where $\Delta_o \gg 1$. Now, $\tilde{y} \gtrsim \Delta_o$ can be written as:

$$\frac{y}{L_0} \gtrsim \frac{\Delta_o}{|\mathrm{Re}_{L_0}|}. \tag{4.38}$$

That is, the extent of the outer layer increases with increase in $|\mathrm{Re}_{L_0}|$. Also note, from Equation 4.35, for a fixed h/L_0, as is needed for the generalized MOST for the outer layer, an increase in $|\mathrm{Re}_{L_0}|$ corresponds to an attendant increase in Re_τ.

In the region at intermediate distance from the wall and for flows at large Re_τ, assuming that ϕ_{u1} obeys complete similarity for $y/h \to 0$ and $\tilde{y} \to \infty$, Equation 4.31 can be written as:

$$\phi_u = \phi_{u6}\left(\frac{y}{L_0}\right), \tag{4.39}$$

which is the traditional form of the MOST (Equation 4.6). As discussed earlier, the collapsed curves of Fig. 4.5 for the intermediate region are in excellent accord with this equation.

In this section, we have generalized MOST by adding the scaling laws of Equations 4.33 and 4.37 to the traditional MOST scaling law of Equation 4.39 (or Equation 4.6). In the next section, we study scaling laws of MVP.

4.5.3 Scaling laws for MVP

As noted before, we derived the classical scaling laws for MVP in plane Couette flows of constant-density fluids by integrating the scaling laws for du/dy. Here, building on the discussion above, we integrate the generalized MOST scaling laws to derive scaling laws for MVP in thermally-stratified plane Couette flows.

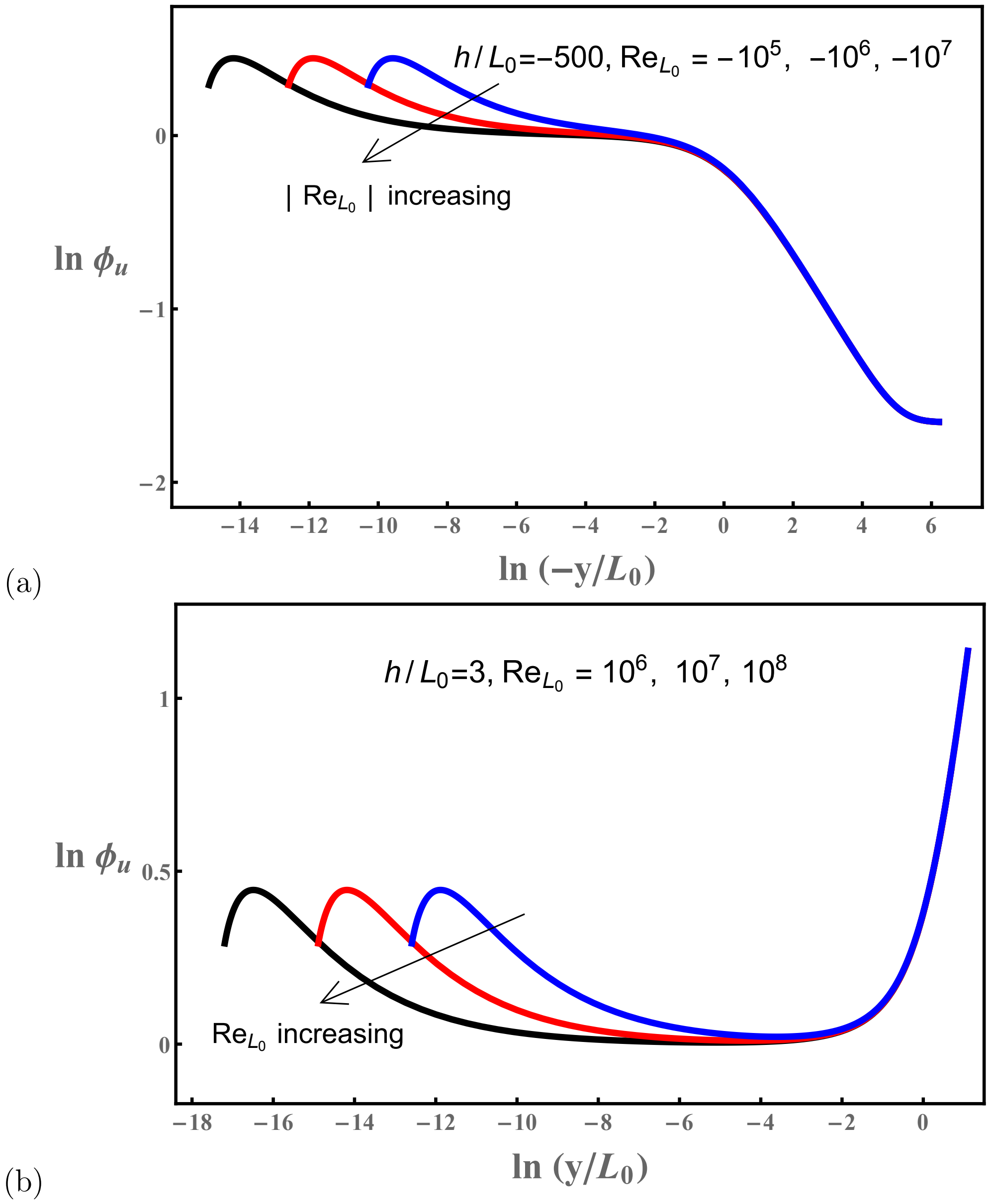

Fig. 4.7: Testing the generalized MOST for the outer layer. Log-log plots of ϕ_u vs. y/L_0 for: (a) unstable stratification, (b) stable stratification. Note the collapsed curves far from the wall. For computing the curves using the spectral theory, we set $\kappa = 0.4, \beta_e = 2$, and $\beta_d = 5.2$.

First, consider the inner layer. Here, the scaling of du/dy is governed by the generalized MOST for the inner layer (Equation 4.33). For a fixed Re_{L_0}, integrating Equation 4.33 in y/L_0 yields:

$$\tilde{u} = I_1(\frac{y}{L_0}), \tag{4.40}$$

where $I_1(x) \equiv \int_0^x \xi^{-1}\phi_{u3}(\xi, \mathrm{Re}_{L_0})d\xi$ and we have used the no-slip boundary condition $\tilde{u}(y/L_0 = 0) = 0$. Noting that $y/L_0 = \tilde{y}/\mathrm{Re}_{L_0}$ and recalling that we have fixed Re_{L_0}, we can write the above equation as:

$$\tilde{u} = I_2(\tilde{y}). \tag{4.41}$$

which, in analogy with classic scaling laws, we call the "law of the wall for thermally-stratified flows". Note that for thermally-stratified flows, we need to keep Re_{L_0} fixed and the functional forms of I_1 and I_2 depend on the value of Re_{L_0}.

To test the validity of the law of the wall for thermally-stratified flows, using the spectral theory, we plot $\tilde{u}$ vs. $\tilde{y}$ for a *fixed* Re_{L_0} and for various values of h/L_0. Per Equation 4.41, in the inner layer and for a fixed Re_{L_0}, $\tilde{u}$ only depends on $\tilde{y}$, and thus the curves corresponding to different h/L_0 should collapse onto one curve. This prediction is in excellent accord with the results from the spectral theory for both unstably-stratified flows and stably-stratified flows (see Fig. 4.8).

As was the case in Fig. 4.6, here, in Fig. 4.8, the region of collapse increases with increase in $|h/L_0|$. The reason again has to do with the extent of the inner layer, $y/h \lesssim \epsilon_i$. This can be written as:

$$\tilde{y} \lesssim \epsilon_i \mathrm{Re}_\tau. \tag{4.42}$$

As we have noted in discussing Equation 4.35, for a fixed $|\mathrm{Re}_{L_0}|$, as is needed for the law of the wall for thermally-stratified flows, an increase in $|h/L_0|$ corresponds to an attendant increase in Re_τ, which, via Equation 4.42, corresponds to an increase in the extent of the inner layer.

In addition to the predictions from the spectral theory, the validity of the law of the wall for thermally-stratified flows is hinted at in the DNS data of Fig. 4.1. In Fig. 4.1, a close look at the DNS data of MVPs for stably-stratified plane Couette flows reveals that, for different values of Re_τ, the curve denoted by red upward-pointing triangles ($\mathrm{Re}_\tau = 540, \mathrm{Re}_{L_0} = 245$) and the curve denoted by black upward-pointing triangles ($\mathrm{Re}_\tau = 349, \mathrm{Re}_{L_0} = 255$) collapse onto each other over the largest extent near the wall. (We replot these curves in Fig. 4.9.) Interestingly, these curves correspond to similar values of Re_{L_0}—in accord with the expectation from the law of the wall for thermally-stratified flows.

A close look at Fig. 4.9 reveals a peculiar feature. In the region far from the wall, the curve denoted by red upward-pointing triangles is slightly higher than the curve denoted by black upward-pointing triangles, but the value of h/L_0 (note $h/L_0 = \mathrm{Re}_\tau/\mathrm{Re}_{L_0}$) is higher for the former curve. This appears to go counter to the trends observed in Fig. 4.8. We can resolve this apparent contradiction by noting that unlike the case in Fig. 4.8, where we have fixed the value of Re_{L_0}, the curves in Fig. 4.9 do not correspond to exactly the same value of Re_{L_0}. To understand why, note that in Fig. 4.3, for a fixed value of Re_τ, as the value of h/L_0 increases (or the value of Re_{L_0} decreases), the MVP in the region far from the wall climbs up. In Fig. 4.9, the value of Re_{L_0} for the curve denoted by red upward-pointing triangles is slightly lower than that of the curve denoted by black upward-pointing triangles. The effect of disparity in the value of Re_{L_0} dominates over the effect of disparity in the value of Re_τ, and therefore the the curve denoted by red upward-pointing triangles is slightly higher than the curve denoted by black upward-pointing triangles.

In the discussion so far we have emphasized that the law of the wall for thermally-stratified flows requires a fixed value of Re_{L_0}. Note, however, that for the MVPs plotted

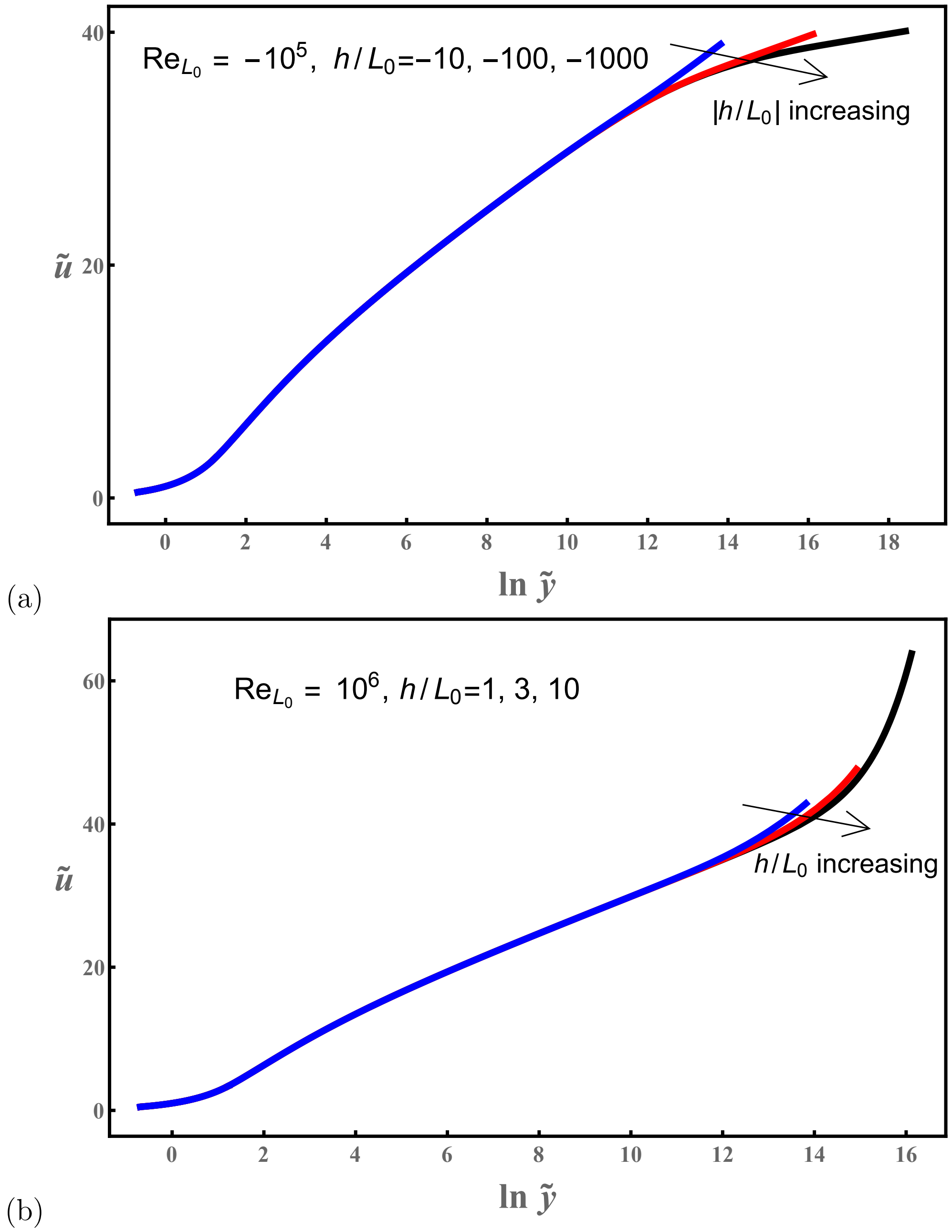

Fig. 4.8: Testing the law of the wall for thermally-stratified flows. Log-linear plots of $\tilde{u}$ vs. $\tilde{y}$ for: (a) unstable stratification, (b) stable stratification. Note the collapsed curves near the wall. For computing the curves using the spectral theory, we set $\kappa = 0.4, \beta_e = 7$, and $\beta_d = 5.2$.

in Fig. 4.3, the different curves correspond to a fixed Re_τ but *varying* Re_{L_0}. And yet, near the wall, the different curves collapse. To explain this observation, we invoke an additional argument of complete similarity, to which we turn next.

Consider Equation 4.32, an equivalent form of the generalized MOST for the inner layer. Integrating in $\tilde{y}$ yields:

$$\tilde{u} = I_3(\frac{y}{L_0}, \tilde{y}), \tag{4.43}$$

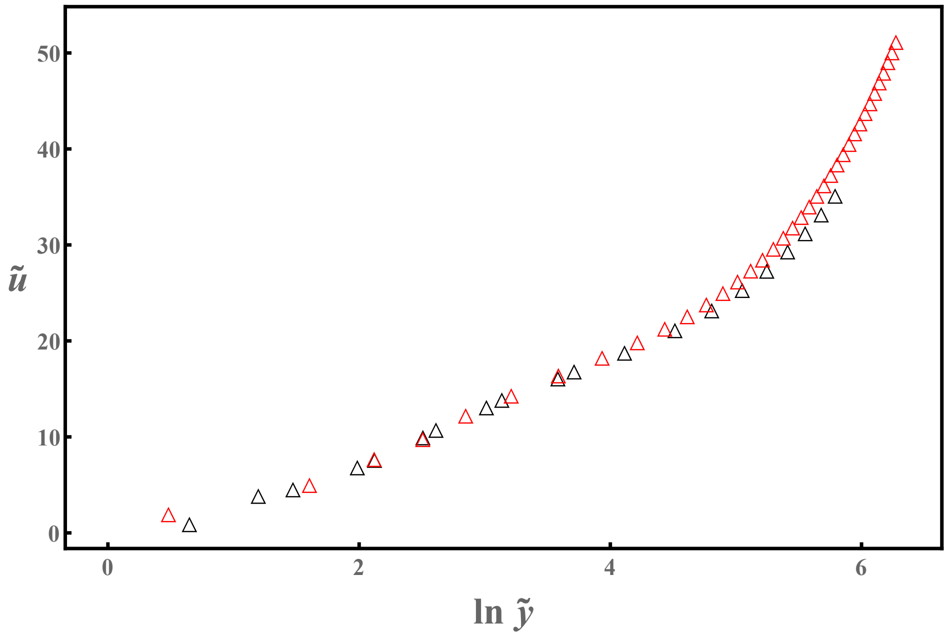

Fig. 4.9: Testing the law of the wall for thermally-stratified flows using DNS data of stably-stratified plane Couette flows from García-Villalba *et al.* (2011) and Deusebio *et al.* (2015). Log-linear plots of $\tilde{u}$ vs. $\tilde{y}$. The curve denoted by red upward-pointing triangles corresponds to $\mathrm{Re}_\tau = 540, \mathrm{Re}_{L_0} = 245$, and the curve denoted by black upward-pointing triangles corresponds to $\mathrm{Re}_\tau = 349, \mathrm{Re}_{L_0} = 255$. Note that these curves collapse onto each other over the largest extent near the wall. Actually, we can not calculate the value of Re_{L_0} directly for the curve denoted by red upward-pointing triangles because not enough details are provided in García-Villalba *et al.* (2011). However, we found a very similar simulation (see also "Run 21" in Zhou *et al.* (2017)) in Deusebio *et al.* (2015), from which we estimate the value of $\mathrm{Re}_{L_0} = 245$, which is very similar to the value of $\mathrm{Re}_{L_0} = 255$ for the curve denoted by black upward-pointing triangles.

where $I_3(x/\mathrm{Re}_{L_0}, x) \equiv \int_0^x \xi^{-1}\phi_{u2}(\xi/\mathrm{Re}_{L_0}, \xi)d\xi$ and we have used the no-slip boundary condition $\tilde{u}(\tilde{y} = 0) = 0$. Note that in deriving Equation 4.32, the starting point for the present analysis, we have invoked complete similarity for $y/h \to 0$. Now, consider similarity of I_3 as $y/L_0 \to 0$. This limit corresponds to the region near the wall (just like the case for $y/h \to 0$) and to the region where the effect of shear dominates over that of buoyancy. Thus, in this region, we might expect the MVP to become independent of stratification. To that end, we assume I_3 obeys complete similarity for $y/L_0 \to 0$ and write Equation 4.43 as:

$$\tilde{u} = I_4(\tilde{y}), \tag{4.44}$$

which is the same as the classical law of the wall.

Note that in deriving Equation 4.44 we did not fix Re_{L_0}, as we did for deriving Equation 4.41. But, whereas Equation 4.41 only considers the limit $y/h \to 0$, Equation 4.44 considers both $y/h \to 0$ and $y/L_0 \to 0$. Based of Equation 4.44, we note that near the wall, when both $y/h \to 0$ and $y/L_0 \to 0$ are satisfied, the MVP obeys the law of the wall, even for varying Re_{L_0}. This explains the observations of Fig. 4.3. We further note that in Fig. 4.1, where we plot MVPs from DNS data with varying Re_τ and varying Re_{L_0}, we still see that the MVPs obey the law of the wall, as indeed is expected from Equation 4.44.

We can also predict how the extent of the region over which Equation 4.44 holds depends on the value of Re_{L_0}. In analogy with the finite extent of the inner layer, we posit that the complete similarity for the asymptotic limit $y/L_0 \to 0$ holds over a finite region $y/L_0 \lesssim \tilde{\epsilon}_i$, where $0 < \tilde{\epsilon}_i \ll 1$. The region $y/L_0 \lesssim \tilde{\epsilon}_i$ can be written as:

$$\tilde{y} \lesssim \tilde{\epsilon}_i |\mathrm{Re}_{L_0}|. \tag{4.45}$$

That is, the extent of this region increases with increase in $|\mathrm{Re}_{L_0}|$. Noting that $|\mathrm{Re}_{L_0}| = \mathrm{Re}_\tau / |h/L_0|$, we infer that the extent of the collapsed region in Fig. 4.3 decreases with increase in $|h/L_0|$, in accord with the prediction from Equation 4.45. As an additional check, in Fig. 4.10, using the spectral theory, we plot $\tilde{u}$ vs. $\tilde{y}$ for a fixed h/L_0 and for various values of Re_{L_0}. In accord with Equation 4.45, the extent of the law of the wall grows with increase in the value of $|\mathrm{Re}_{L_0}|$.

Next, consider the outer layer. Here, the scaling of du/dy is governed by the generalized MOST for the outer layer (Equation 4.37). For a fixed h/L_0, integrating Equation 4.37 in y/L_0 yields:

$$\tilde{u}_c - \tilde{u} = O_1\left(\frac{y}{L_0}\right), \tag{4.46}$$

where $\tilde{u}_c \equiv \tilde{u}(y = h)$ and $O_1(x) \equiv \int_x^{h/L_0} \xi^{-1} \phi_{u5}(\xi, h/L_0) d\xi$. Noting that $y/L_0 = y/h \times h/L_0$ and recalling that we have fixed h/L_0, we can write the above equation as:

$$\tilde{u}_c - \tilde{u} = O_2(\frac{y}{h}). \tag{4.47}$$

which, in analogy with classic scaling laws, we call the "defect law for thermally-stratified flows". Note that for thermally-stratified flows, we need to keep h/L_0 fixed and the functional forms of O_1 and O_2 depend on the value of h/L_0.

To test the validity of the defect law for thermally-stratified flows, using the spectral theory, we plot $\tilde{u}_c - \tilde{u}$ vs. y/h for a *fixed* h/L_0 and for various values of Re_{L_0}. Per Equation 4.47, in the outer layer and for a fixed h/L_0, $\tilde{u}_c - \tilde{u}$ only depends on y/h, and thus the curves corresponding to different Re_{L_0} should collapse onto one curve. This prediction is in excellent accord with the results from the spectral theory for both unstably-stratified flows and stably-stratified flows (see Fig. 4.11).

As was the case in Fig. 4.7, here, in Fig. 4.11, the region of collapse increases with increase in $|\mathrm{Re}_{L_0}|$. The reason again has to do with the extent of the outer layer, $\tilde{y} \gtrsim \Delta_o$. This can be written as:

$$\frac{y}{h} \gtrsim \frac{\Delta_o}{\mathrm{Re}_\tau}. \tag{4.48}$$

As we have noted in discussing Equation 4.35, for a fixed $|h/L_0|$, as is needed for the defect law for thermally-stratified flows, an increase in $|\mathrm{Re}_{L_0}|$ corresponds to an attendant increase in Re_τ, which, via Equation 4.48, corresponds to an increase in the extent of the outer layer.

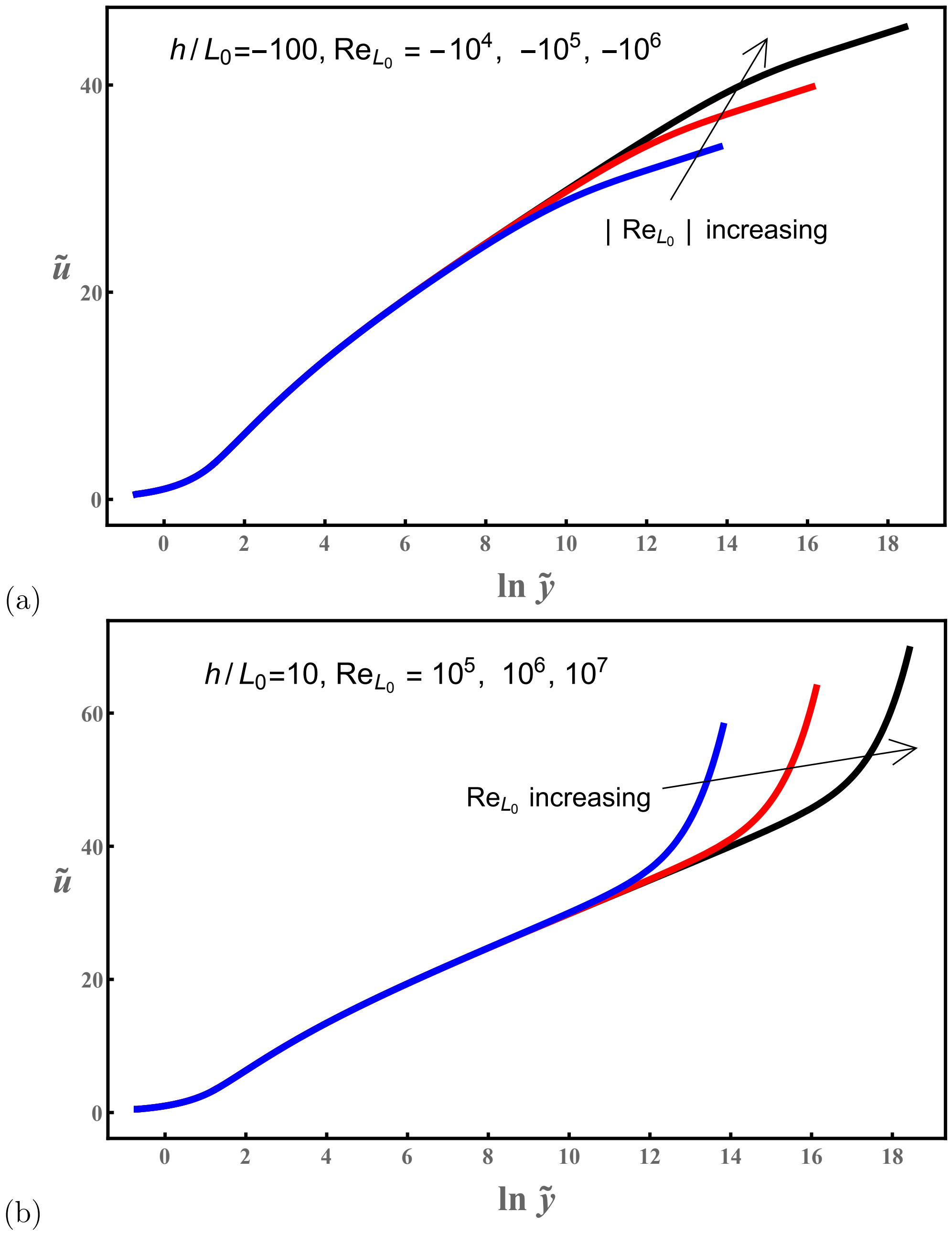

Fig. 4.10: Testing the extent of the law of the wall, Equation 4.44. Log-linear plots of $\tilde{u}$ vs. $\tilde{y}$ for: (a) unstable stratification, (b) stable stratification. We fix h/L_0 and vary Re_{L_0}. Note the collapsed curves near the wall. For computing the curves using the spectral theory, we set $\kappa = 0.4, \beta_e = 7$, and $\beta_d = 5.2$.

Unlike the law of the wall for thermally-stratified flows, we cannot use the available DNS data to test the the validity of the defect law for thermally-stratified flows. This is because testing the defect law requires high Reynolds numbers, as is well known for the case of the defect law for constant-density fluids (Wu & Moin, 2008).

In discussing the law of the wall for thermally-stratified flows, which entails fixing the value of Re_{L_0}, we noted that even when Re_{L_0} varies, in the region near the wall, the

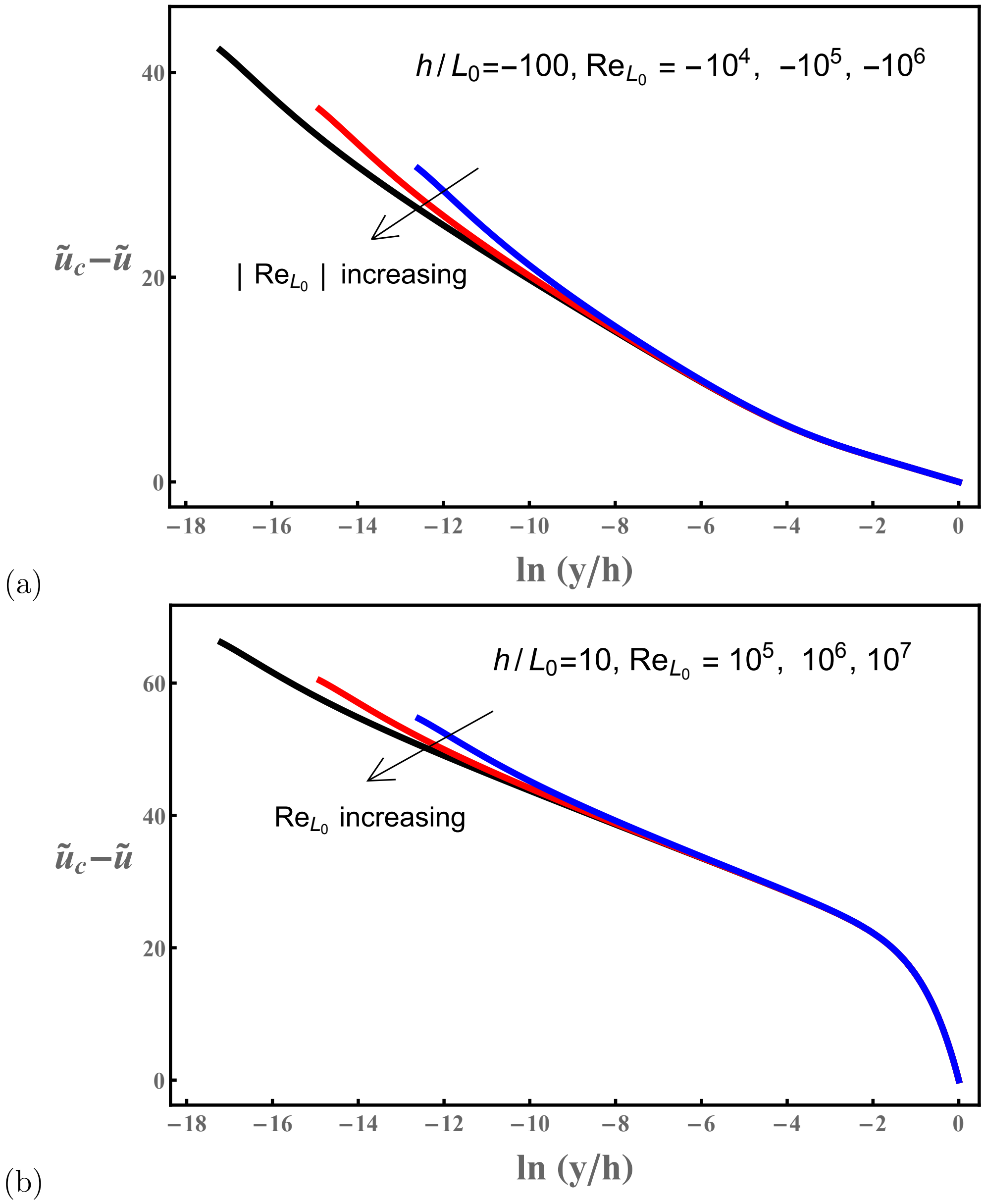

Fig. 4.11: Testing the defect law for thermally-stratified flows. Log-linear plots of $\tilde{u}_c - \tilde{u}$ vs. y/h for: (a) unstable stratification, (b) stable stratification. Note the collapsed curves far from the wall. For computing the curves using the spectral theory, we set $\kappa = 0.4, \beta_e = 7$, and $\beta_d = 5.2$.

MVPs collapse, analogous to the classical law of the wall. We explained this observation by noting that if we go very close to the wall (corresponding to $y \ll L_0$), the effect of stratification becomes negligible. In the case of the defect law for thermally-stratified flows, however, we cannot invoke a similar argument. Unless we restrict attention to flows with $|L_0| \gg h$, i.e., flows of constant-density fluids, we cannot neglect the effect of stratification in the outer layer. Thus, the defect law for thermally-stratified flows is predicated on fixing h/L_0. Indeed, by comparing the shapes of the collapsed curves far from the wall in panels (a) and (b) of Fig. 4.11, which panels correspond to different values of h/L_0, we note that these curves have different profiles.

Last, consider the intermediate region. Here, the scaling of du/dy is governed by the traditional form of the MOST (Equation 4.6), which, after integration in y/L_0, shows how the MVP deviates from the log law (see Section 4.2). These considerations are well known (Turner, 1973) and we do not discuss them further.

4.6 Discussion and summary

We studied the MVP in thermally-stratified plane Couette flows. Empirical data on the MVPs show distinctive shapes, which change with the stratification of the flow. While previous theoretical studies of the MVP have exclusively focused on its intermediate region—this is the region of interest for the well-known framework of MOST—the region near the wall and the region far from the wall have remained unexplored. Here we studied the whole extent of the MVP using two approaches: the spectral theory and scaling analysis.

We adapted the spectral theory (Gioia *et al.*, 2010), which was originally proposed for constant-density flows, to study thermally-stratified flows. In our analysis, we considered the whole structure of $E(k)$—inertial range plus the energetic-range and dissipative-range corrections—as well as the whole extent of the MVP—from the wall to the centerline. Noting that very close to the wall (for $y \ll L_0$) shear dominates over buoyancy, we simplified the heat equation. This leads to a simplified energy balance, which we solved together with the momentum balance to obtain the MVP. The predicted MVP from the spectral theory captures all the salient qualitative features of the empirical MVP over its whole extent. The distinctive shape of the MVP can be understood in terms of the energetics of the turbulent eddies.

Except for flows where $Pr \ll 1$, which flows we do not consider, the MVPs computed using the spectral theory do not depend on the value of Pr. A test of this prediction would be to plot the MVPs for different flows where the Pr is varied and the other parameters $(\mathrm{Re}_{L_0}, h/L_0)$ are fixed. We are not aware of any empirical data with which we can perform such a test.

By varying the values of the dimensionless parameters Re_{L_0} and h/L_0 (or, equivalently, Re_τ and h/L_0), using the spectral theory, we computed the MVPs. We studied the scaling of the MVP and its derivative (ϕ_u) using scaling laws. To that end, we invoked the tools of dimensional analysis and complete similarity, and derived the scaling laws by adapting the framework of the classical scaling laws for constant-density flows. Our analysis yielded a generalized MOST. For the intermediate region, we recovered MOST; for the inner layer and the outer layer, we derived new scaling laws.

In the inner layer $(y/h \to 0)$, for the scaling of ϕ_u, we derived the generalized MOST for the inner layer (Equation 4.33):

$$\phi_u = \phi_{u3}\left(\frac{y}{L_0}, \mathrm{Re}_{L_0}\right),$$

and for the scaling of MVP, we derived the law of the wall for thermally-stratified flows (Equation 4.41):

$$\tilde{u} = I_2(\tilde{y}),$$

where the functional form of I_2 depends on the value of Re_{L_0}. Testing the scaling laws for ϕ_u and MVP in the inner layer requires us to fix the value of Re_{L_0}. Guided by the results of the spectral theory and physical considerations, for the subset of the inner layer where $y/h \to 0$ and $y/L_0 \to 0$, we argued that the above scaling laws become independent of the value of Re_{L_0}. This prediction is in accord with empirical data.

In the outer layer ($\tilde{y} \to \infty$), for the scaling of ϕ_u, we derived the generalized MOST for the outer layer (Equation 4.37):

$$\phi_u = \phi_{u5}\left(\frac{y}{L_0}, \frac{h}{L_0}\right),$$

and for the scaling of MVP, we derived the defect law for thermally-stratified flows (Equation 4.47):

$$\tilde{u}_c - \tilde{u} = O_2(\frac{y}{h}),$$

where the functional form of O_2 depends on the value of h/L_0. Testing the scaling laws for ϕ_u and MVP in the outer layer requires us to fix the value of h/L_0.

Finally, we hope that our analysis would motivate future experimental and numerical studies. Studies targeted at measuring the MVPs for a fixed Re_{L_0} and varying h/L_0 and the MVPs for a fixed h/L_0 and varying Re_{L_0} would provide valuable tests for the scalings in the inner layer and the outer layer, respectively, thereby greatly expanding the scope of the analysis for thermally-stratified flows, which have hitherto been restricted to the intermediate region.

Chapter 5

Conclusion

In this thesis, we have been concerned with what is perhaps the most fundamental macroscopic property of the canonical wall-bounded turbulent flows, the mean-velocity profile (MVP). Our aim has been to shed some new theoretical light on several outstanding problems in the interpretation of the MVPs of such flows in both constant-density and stratified media. The aim of this brief chapter is to recapitulate our findings, discuss the import and implications of the most salient theoretical concepts we have developed and built upon, especially in connection with the spectral link, and offer a few general conclusions.

The spectral theory formulated in this thesis has been grounded on the "spectral link" that relates the MVPs to the eddy velocity distribution of the phenomenological theory of turbulence. A crucial fact associated with the spectral link is that the turbulent eddies that dominate momentum transfer at a distance y from the wall—the *dominant eddies* at a distance y from the wall—are the eddies of size y. This crucial fact we have been able to justify without having recourse to any ad-hoc assumptions, on the basis of (1) a straightforward physical argument whereby the turbulent shear stress stems from momentum transfer effected by turbulent eddies and (2) the core premise underlying the spectral link, namely, that the characteristic velocity of a turbulent eddy of any given size y, v_y, is fully determined by y via the eddy velocity distribution of the phenomenological theory, $v_y(y)$.

Thus, the turbulent shear stress at a distance y from the wall (and, therefore, the attendant slope of the MVP at that distance from the wall) is inextricably linked to the eddy velocity distribution $v_y(y)$. This is the spectral link whereby successive layers of the MVP (associated with increasing distance to the wall) are put in relation with the successive ranges of the eddy velocity distribution (associated with increasing size of the dominant eddy). From these considerations there follows a notable property of the spectral link: that there is a one-to-one, or bijective, relation between the successive layers of a MVP and the successive ranges of the eddy velocity distribution, in such a way that the buffer layer relates to, and only to, the dissipative range; the log layer relates to, and only to, the inertial range; and the wake relates to, and only to, the energetic range.

Now, from the phenomenological theory, we know that the dissipative range, the inertial range, and the energetic range correspond to specific physical regimes in the energetics of turbulence (so that the eddies of the inertial range are dominated by inertial forces and remain unaffected by either viscous or finite-domain effects, whereas the eddies of the dissipative range and the eddies of the energetic range are affected by viscous effects and finite-domain effects, respectively). By virtue of the bijective property of the spectral link, we have been able to ascribe a specific physical regime to each layer of the MVP, and to conclude that the log layer corresponds to a regime of dynamic equilibrium in which the dominant eddies partake in the energy cascade, unaffected by either viscous or finite-domain effects, whereas the buffer layer and the wake are but local steepenings of the MVP due to the lessened capacity for momentum transfer of dominant eddies that are slowed down by viscous effects and finite-domain effects, respectively.

Furthermore, we have argued that the bijective property of the spectral link can be put to use to ascertain the way in which two states of turbulence differ from one another based solely on the observed differences in the associated MVPs. This comes about because, by virtue of the bijective property of the spectral link, each layer of a MVP displays information about a specific range of the eddy velocity distribution, and it is possible to infer the internal structure of a turbulent state, as one would by parsing through each of the successive ranges of the eddy velocity distribution, by parsing through the successive layers of the attendant MVP.

Thus, in Chapter 2, we have invoked the bijective property of the spectral link to explain the significant disparities between the turbulent MVPs of pipe flow and channel flow. These disparities are circumscribed to the wakes, and we have been able to infer that they are but manifestations of the geometrical differences between pipe flow and channel flow, whereby the largest eddies in the flow, which are the dominant eddies in the wake, are altered by interaction with the boundaries of the flow (finite-domain effects), in a way that changes from flow to flow. On the other hand, small-scale universality prevails at small lengthscales, at which the internal structure of pipe flow and channel flow is one and the same, as can be inferred from the fact that the MVP of pipe flow and the MVP of channel flow collapse onto one another in both the buffer layer and the log layer.

In Chapter 3 we have turned our attention to a number of well-known, and as yet unresolved, disparities in the classical experimental data on friction factor in turbulent plane Couette flow. We have pointed out that those disparities are accompanied by previously unnoticed disparities in the wakes, and only in the wakes, of the attendant MVPs. By assessing the empirical data in light of the spectral theory, we have argued for the existence, in plane Couette flow, of multiple states of turbulence, which may be a generic feature of turbulent flows with moving boundaries. In the literature, the existence of multiple turbulence states has been put forth along with claims that it might be at odds with the principle of small-scale universality, a fundamental result of the phenomenological theory.

To settle the matter, we have been able to invoke the bijective property of the spectral link to ascertain the ways in which these multiple turbulent states differ from one another, namely only at the largest lengthscales in the flow, corresponding to the energetic range of the eddy velocity distribution. Thus, the multiplicity of turbulent states is in fact perfectly consistent with small-scale universality, and the experimental data on plane Couette flow pose no challenge to the phenomenological theory.

In Chapter 4, we have moved on to the MVPs in thermally-stratified plane Couette flows, for which the empirical data show distinctive shapes, depending on the stratification of the flow. Thermal stratification, which amounts to a temperature-dependent distribution of fluid density, necessitates a modification of the energy equation, wherein the expression for the turbulent power per unit mass ε consists of two additive terms, the customary turbulent-production term plus a buoyant-production term. We focus on the influence of this buoyant-production term.

The bijective property of the spectral link prevails in the presence of thermal stratification, but the canonical layers (buffer layer, log layer, and wake) are modified by buoyancy. Thus, for example, the region corresponding to the inertial range does not correspond to a log layer any longer. This region is the intermediate region of interest in the Monin-Obukhov similarity theory (MOST). While much analysis has focused on this intermediate region, the region near the wall and the region far from the wall and beyond the intermediate one had not been theoretically studied before, but we have shown them to be amenable to theoretical interpretation using the spectral link. Across the extent of the flow, we studied how the buoyancy modifies the MVPs for both unstably-stratified flows and stably-stratified flows. Our results are in excellent qualitative accord with the distinctive shapes of the MVPs seen in empirical data.

In addition, using dimensional analysis and similarity arguments, we have derived generalized versions of the classical scaling laws of the MOST applicable in the region near the wall (the inner layer), in the intermediate region (which coincides with MOST), and in the region far from the wall (the outer layer). The generalized version applicable in the inner layer and the generalized version applicable in the outer layer amount to testable predictions. These predictions are in excellent accord with the results from the spectral theory. Our work suggests that concrete experiments and computations may yield suitable empirical data for testing the predictions.

To summarize: in this thesis we have established a spectral link between the MVPs of some of the canonical turbulent flows and the eddy velocity distribution of the phenomenological theory, verified the bijective property of the spectral link, and used it to shed some new theoretical light on several outstanding problems in the interpretation of such MVPs. To establish the spectral link, we have used a specific model of momentum transfer as well as a specific form of the energy equation. Nevertheless, it has been shown that the existence of a bijective spectral link may be proven without having recourse to any specific models of wall turbulence, solely on the basis of dimensional analysis and similarity arguments (Gioia & Chakraborty, 2017), with the implication that a bijective spectral link should be considered as a requisite attribute of *every* model of wall turbulence. However, models of wall turbulence, including the Prandtl model of the MVP, are usually oblivious of the internal structure of turbulence. These models ignore the eddy velocity distribution, on which much knowledge is readily available, supported by a vast corpus of empirical evidence, and thus miss the opportunity to harness that knowledge in an effort to better understand the physics of wall-bounded turbulent flows. We hope that our findings will foster the formulation of better spectral models which might help opening up new prospects of gaining further insight into turbulence, “the most important unsolved problem of classical physics”.

Appendix A

Total shear stress

For an incompressible and isotropic Newtonian fluid, the continuity equation and momentum equation read (Pope, 2000):

$$\frac{\partial u_i}{\partial x_i} = 0, \tag{A.1}$$

and

$$\frac{\partial u_i}{\partial t} + u_j \frac{\partial u_i}{\partial x_j} = -\frac{1}{\rho}\frac{\partial p}{\partial x_i} + \nu \frac{\partial^2 u_i}{\partial x_j \partial x_j}, \tag{A.2}$$

where $\vec{u} \equiv u_i \vec{e_i}$ is the velocity field, which fluctuates randomly in both position $\vec{x} \equiv x_i \vec{e_i}$ and time t when the flow is turbulent, ρ is the fluid density, p is pressure, and ν is the kinematic viscosity. According to Reynolds decomposition (Davidson, 2004), defining the flow variables $u_i = \overline{u_i} + u_i'$, and $p = \overline{p} + p'$, where $\overline{u_i}$ is a local mean velocity in $\vec{e_i}$ direction, $\overline{p}$ is a local mean pressure, both averaged over a long time, u_i' and p' denote the fluctuating velocity component in $\vec{e_i}$ direction and fluctuating pressure component respectively. The time average of the fluctuating components equals zero. Therefore, after averaging and a rearrangement, the mean continuity equation and mean momentum equation (Reynolds equation) are obtained (Pope, 2000),

$$\frac{\partial \overline{u_i}}{\partial x_i} = 0, \tag{A.3}$$

and

$$\frac{\partial \overline{u_i}}{\partial t} + \overline{u_j} \frac{\partial \overline{u_i}}{\partial x_j} = -\frac{1}{\rho}\frac{\partial \overline{p}}{\partial x_i} + \frac{\partial}{\partial x_j}\left(\nu \frac{\partial \overline{u_i}}{\partial x_j} - \overline{u_i' u_j'}\right). \tag{A.4}$$

In the fully developed flow region, the flow becomes statistically one-dimensional (Pope, 2000). Thus, the local mean velocity u, at a distance y from the wall reduces to $u(y) = \overline{u_1}(x_2)$, which depends only on x_2, i.e., y. The function $u(y)$ is called the MVP. The lateral mean momentum equation reduces to

$$0 = -\frac{1}{\rho}\frac{\partial \overline{p}}{\partial y} - \frac{\partial \overline{u_2' u_2'}}{\partial y}, \tag{A.5}$$

which integrates to

$$p_0/\rho = \overline{p}/\rho + \overline{u_2' u_2'}, \tag{A.6}$$

with the boundary condition $\overline{u_2'u_2'}_{(y=0)} = 0, p_0 = \overline{p}_{(y=0)}$. As the flow is statistically one-dimensional, $\partial\overline{u_2'u_2'}/\partial x_1 = 0$. Then the mean axial pressure gradient is uniform across the flow,

$$\frac{\partial\overline{p}}{\partial x_1} = \frac{dp_0}{dx_1}. \tag{A.7}$$

The axial mean momentum equation reads,

$$0 = -\frac{1}{\rho}\frac{\partial\overline{p}}{\partial x_1} + \nu\frac{d^2u}{dy^2} - \frac{d\overline{u_1'u_2'}}{dy}, \tag{A.8}$$

Defining the total shear stress

$$\tau(y) = \rho\nu\frac{du}{dy} - \rho\overline{u_1'u_2'}, \tag{A.9}$$

where $\rho\nu du/dy$ is the viscous shear stress, and $\rho\overline{u_1'u_2'}$ can be regarded as the turbulent shear stress. Then the axial mean momentum equation becomes,

$$\frac{d\tau}{dy} = \frac{dp_0}{dx_1}, \tag{A.10}$$

which is the balance of mean forces per unit volume. Since τ is only a function of y and p_0 only depends on x_1, both $d\tau/dy$ and dp_0/dx_1 should be constant due to Equation A.10.

Assume $\tau(y = 0) = \tau_0$. For pipe flow (radius R) and channel flow (half width h), the velocity field is symmetric about the centerline, so $\tau(y)$ is antisymmetric about the centerline. Thus, $\tau(y = 2R) = -\tau_0$ or $\tau(y = 2h) = -\tau_0$. Integrating Equation A.10 with the boundary conditions at $y = 0$ and $y = 2R$ or $y = 2h$,

$$\tau(y) = \tau_0(1 - y/R), \tag{A.11}$$

or

$$\tau(y) = \tau_0(1 - y/h). \tag{A.12}$$

For plane Couette flow (half width b), there is no axial pressure gradient imposed, so $d\tau/dy = 0$. Then

$$\tau(y) = \tau_0. \tag{A.13}$$

It is widely accepted that for an incompressible and isotropic Newtonian fluid, the viscous stress tensor is linearly related to the symmetric strain rate tensor (Kundu & Cohen, 2002),

$$\vec{\tau_v} = \rho\nu(\vec{\nabla}\vec{u} + \vec{u}\vec{\nabla}). \tag{A.14}$$

In Cartesian coordinates,

$$\vec{\nabla}\vec{u} = \begin{pmatrix} \frac{\partial u_1}{\partial x_1} & \frac{\partial u_2}{\partial x_1} & \frac{\partial u_3}{\partial x_1} \\ \frac{\partial u_1}{\partial x_2} & \frac{\partial u_2}{\partial x_2} & \frac{\partial u_3}{\partial x_2} \\ \frac{\partial u_1}{\partial x_3} & \frac{\partial u_2}{\partial x_3} & \frac{\partial u_3}{\partial x_3} \end{pmatrix}, \tag{A.15}$$

and

$$\vec{\nabla}\vec{u} = (\vec{u}\vec{\nabla})^T. \tag{A.16}$$

Due to the turbulent viscosity hypothesis introduced by Boussinesq in 1877 (Pope, 2000), the turbulent stress tensor

$$\vec{\tau}_t = -\rho \begin{pmatrix} \overline{u_1'^2} & \overline{u_1'u_2'} & \overline{u_1'u_3'} \\ \overline{u_1'u_2'} & \overline{u_2'^2} & \overline{u_2'u_3'} \\ \overline{u_1'u_3'} & \overline{u_2'u_3'} & \overline{u_3'^2} \end{pmatrix} = \rho\nu_t(\vec{\nabla}\vec{u} + \vec{u}\vec{\nabla}) - \frac{2}{3}\rho K \begin{pmatrix} 1 & 0 & 0 \\ 0 & 1 & 0 \\ 0 & 0 & 1 \end{pmatrix}, \tag{A.17}$$

where the positive scalar coefficient ν_t is the turbulent viscosity, and $K = \frac{1}{2}\overline{u_i'u_i'}$ is the turbulent kinetic energy. Thus, the total shear stress

$$\tau(y) = \tau_{v12} + \tau_{t12} = \rho(\nu + \nu_t)\frac{\partial u_1}{\partial x_2} = \rho(\nu + \nu_t)\frac{du}{dy}, \tag{A.18}$$

which is consistent with Equation 2.11.

Appendix B

Turbulent power per unit mass

The turbulent power per unit mass balancing the dissipation of turbulent kinetic energy can be obtained from the turbulent kinetic energy budget. In Cartesian coordinate, $K = \frac{1}{2}\overline{u_i'u_i'}$, and the budget reads (Kundu & Cohen, 2002),

$$\begin{aligned}\underbrace{\frac{\partial \frac{1}{2}\overline{u_i'u_i'}}{\partial t}}_{\text{Local derivative}} = &-\underbrace{\overline{u_j}\frac{\partial \frac{1}{2}\overline{u_i'u_i'}}{\partial x_j}}_{\text{Advection}} - \underbrace{\nu\overline{\frac{\partial u_i'}{\partial x_j}\frac{\partial u_i'}{\partial x_j}}}_{\text{Dissipation } \varepsilon} + \underbrace{g\alpha H_s}_{\text{Buoyant production}} \underbrace{-\overline{u_i'u_j'}\frac{\partial \overline{u_i}}{\partial x_j}}_{\text{Shear production } P} \\ &\underbrace{-\frac{\partial \frac{1}{2}\overline{u_i'u_i'u_j'}}{\partial x_j}}_{\text{Turbulent diffusion}} + \underbrace{\nu\frac{\partial^2 \frac{1}{2}\overline{u_i'u_i'}}{\partial x_j \partial x_j}}_{\text{Viscous diffusion}} \underbrace{-\frac{1}{\rho}\frac{\overline{p'u_j'}}{\partial x_j}}_{\text{Pressure diffusion}}\end{aligned} \tag{B.1}$$

In all cases considered in this thesis, the local rate of change of the turbulent kinetic energy K is assumed to be zero. Thus, the budget gives that the dissipation of turbulent kinetic energy ε is balanced by the sum of all other terms on the right-hand side of Equation B.1, i.e., the turbulent power per unit mass. The dominant terms balancing the dissipation of turbulent kinetic energy in each case are estimated as follows. For pipe flow, channel flow, and plane Couette flow,we assume that the dissipation of turbulent kinetic energy is balanced shear production. For thermally stratified turbulent flows, the sum of the shear production and buoyant production is assumed to balance the dissipation of turbulent kinetic energy.

Bibliography

Adrian, R. J. 2007 Hairpin vortex organization in wall turbulence. *Phys. Fluids* **19** (4), 041301.

Anbarlooei, H., Cruz, D., Ramos, F. & Freire, A. S. 2015 Phenomenological Blasius-type friction equation for turbulent power-law fluid flows. *Phys. Rev. E* **92** (6), 063006.

Anbarlooei, H., Cruz, D., Ramos, F., Santos, C. M. & Freire, A. S. 2017 Phenomenological friction equation for turbulent flow of Bingham fluids. *Phys. Rev. E* **96** (2), 023107.

Avsarkisov, V., Hoyas, S., Oberlack, M. & Garcia-Galache, J. P. 2014 Turbulent plane Couette flow at moderately high Reynolds number. *J. Fluid Mech.* **751**, R1–10.

Barenblatt, G. I. 1996 *Scaling, self-similarity, and intermediate asymptotics: dimensional analysis and intermediate asymptotics*, , vol. 14. Cambridge University Press.

Bech, K. H., Tillmark, N., Alfredsson, P. & Anderson, H. I. 1995 An investigation of turbulent plane Couette flow at low Reynolds numbers. *J. Fluid Mech.* **286**, 291–325.

Bernardini, M., Pirozzoli, S. & Orlandi, P. 2014 Velocity statistics in turbulent channel flow up to Re_τ= 4000. *J. Fluid Mech.* **742**, 171–191.

Blasius, H. 1913 Das ähnlichkeitsgesetz bei reibungsvorgängen in flüssigkeiten. *Forsch. Arb. Ing.* **134**.

Bridge, J. S. 2009 *Rivers and floodplains: forms, processes, and sedimentary record*. John Wiley & Sons.

Burger, E., Chorn, L. & Perkins, T. 1980 Studies of drag reduction conducted over a broad range of pipeline conditions when flowing Prudhoe Bay crude oil. *J. Rheol.* **24** (5), 603–626.

Businger, J. A., Wyngaard, J. C., Izumi, Y. & Bradley, E. F. 1971 Flux-profile relationships in the atmospheric surface layer. *J. Atmos. Sci.* **28** (2), 181–189.

Calzetta, E. 2010 Drag reduction by polymer additives from turbulent spectra. *Phys. Rev. E* **82** (6), 066310.

Calzetta, E. 2012 Extension of the momentum transfer model to time-dependent pipe turbulence. *Phys. Rev. E* **85** (2), 026305.

Cerbus, R. T., Liu, C.-c., Gioia, G. & Chakraborty, P. 2018 Laws of resistance in transitional pipe flows. *Phys. Rev. Lett.* **120**, 054502.

Chézy, A. 1776 Formule pour trouver la vitesse de l'eau conduite dans une rigole donnée. *Dossier 847 (MS 1915) of the manuscript collection of the École National des Ponts et Chaussées, Paris* .

Chin, C., Monty, J. P. & Ooi, A. 2014 Reynolds number effects in DNS of pipe flow and comparison with channels and boundary layers. *Int. J. Heat and Fluid Flow* **45**, 33–40.

Davidson, P. A. 2004 *Turbulence*. Oxford, England: Oxford University Press.

Deusebio, E., Caulfield, C. & Taylor, J. 2015 The intermittency boundary in stratified plane Couette flow. *J. Fluid Mech.* **781**, 298–329.

Doering, C. R. 2009 The 3D Navier-Stokes problem. *Annu. Rev. Fluid Mech.* **41**, 109–128.

Dubief, Y., Terrapon, V. E. & Soria, J. 2013 On the mechanism of elasto-inertial turbulence. *Phys. Fluids* **25** (11), 110817.

Eggels, J. G. M., Unger, F., Weiss, M. H., Westerweel, J., Adrian, R. J., Friedrich, R. & Nieuwstadt, F. T. M. 1994 Fully developed turbulent pipe flow: a comparison between direct numerical simulation and experiment. *J. Fluid Mech.* **268**, 175–209.

El Khoury, G. K., Schlatter, P., Noorani, A., Fischer, P. F., Brethouwer, G. & Johansson, A. V. 2013 Direct numerical simulation of turbulent pipe flow at moderately high Reynolds numbers. *Flow Turbul Combust* **91** (3), 475–495.

Fernando, H. J. 1991 Turbulent mixing in stratified fluids. *Annu. Rev. Fluid Mech.* **23** (1), 455–493.

Feynman, R. P., Leighton, R. B. & Sands, M. L. 1963 *The Feynman lectures on physics*. Reading, MA: Addison-Wesley.

Fouxon, A. & Lebedev, V. 2003 Spectra of turbulence in dilute polymer solutions. *Phys. Fluids* **15** (7), 2060–2072.

Frisch, U. 1995 *Turbulence*. Cambridge, England: Cambridge University Press.

Furuichi, N., Terao, Y., Wada, Y. & Tsuji, Y. 2015 Friction factor and mean velocity profile for pipe flow at high Reynolds numbers. *Phys. Fluids* **27** (9), 095108.

García-Villalba, M. & del Álamo, J. C. 2011 Turbulence modification by stable stratification in channel flow. *Phys. Fluids* **23**, 045104.

García-Villalba, M., Azagra, E. & Uhlmann, M. 2011 A numerical study of turbulent stably-stratified plane Couette flow. In *High Performance Computing in Science and Engineering'10*, pp. 251–261. Springer.

Gargett, A. E. 1989 Ocean turbulence. *Annu. Rev. Fluid Mech.* **21** (1), 419–451.

Garratt, J. R. 1992 *The Atmospheric Boundary Layer*. Cambridge University Press.

Garratt, J. R. 1994 The atmospheric boundary layer. *Earth-Sci. Rev.* **37** (1-2), 89–134.

Gioia, G. & Bombardelli, F. 2001 Scaling and similarity in rough channel flows. *Phys. Rev. Lett.* **88** (1), 014501.

Gioia, G. & Chakraborty, P. 2006 Turbulent friction in rough pipes and the energy spectrum of the phenomenological theory. *Phys. Rev. Lett.* **96**, 044502.

Gioia, G. & Chakraborty, P. 2017 Spectral derivation of the classic laws of wall-bounded turbulent flows. *Proc. R. Soc. A* **473** (2204), 20170354.

Gioia, G., Guttenberg, N., Goldenfeld, N. & Chakraborty, P. 2010 Spectral theory of the turbulent mean-velocity profile. *Phys. Rev. Lett.* **105**, 184501.

Huisman, S. G., Veen, R. C., Sun, C. & Lohse, D. 2014 Multiple states in highly turbulent Taylor-Couette flow. *Nat. Commun.* **5** (3820).

Hultmark, M., Vallikivi, M., Bailey, S. C. C. & Smits, A. J. 2012 Turbulent pipe flow at extreme Reynolds numbers. *Phys. Rev. Lett.* **108** (9), 094501.

Hultmark, M., Vallikivi, M., Bailey, S. C. C. & Smits, A. J. 2013 Logarithmic scaling of turbulence in smooth-and rough-wall pipe flow. *J. Fluid Mech.* **728**, 376–395.

Hussain, A. F. 1983 Coherent structures—reality and myth. *Phys. Fluids* **26** (10), 2816–2850.

Ishihara, T., Gotoh, T. & Kaneda, Y. 2009 Study of high-Reynolds number isotropic turbulence by direct numerical simulation. *Annu. Rev. Fluid Mech.* **41**, 165–180.

Kader, B. A. & Yaglom, A. M. 1990 Mean fields and fluctuation moments in unstably stratified turbulent boundary layers. *J. Fluid Mech.* **212**, 637–662.

Katul, G. G., Konings, A. G. & Porporato, A. 2011 Mean velocity profile in a sheared and thermally stratified atmospheric boundary layer. *Phys. Rev. Lett.* **107**, 268502.

Kelland, M. A. 2014 *Production chemicals for the oil and gas industry*. CRC press.

Kim, J. 2012 Progress in pipe and channel flow turbulence, 1961–2011. *J. Turbul.* (13), N45.

Kim, J., Moin, P. & Moser, R. 1987 Turbulence statistics in fully developed channel flow at low Reynolds number. *J. Fluid Mech.* **177**, 133–166.

Kitoh, O., Nakabyashi, K. & Nishimura, F. 2005 Experimental study on mean velocity and turbulence characteristics of plane Couette flow: low-Reynolds-number effects and large longitudinal vortical structure. *J. Fluid Mech.* **539**, 199–227.

Kolmogórov, A. N. 1941*a* Dissipation of energy in the locally isotropic turbulence. *Dokl. Akad. Nauk SSSR* **32**, 19–21.

Kolmogórov, A. N. 1941*b* The local structure of turbulence in incompressible viscous fluid for very large Reynolds numbers. *Dokl. Akad. Nauk SSSR* **30**, 301–305.

Kundu, P. K. & Cohen, I. M. 2002 *Fluid Mechanics*, 2nd edn. San Diego, CA: Academic Press.

Lee, M. J. & Kim, J. 1991 The structure of turbulence in a simulated plane Couette flow. In *8th Symposium on Turbulent Shear Flows, Munich, Federal Republic of Germany, Sept. 9-11, 1991, Proceedings. Vol. 1*, pp. 531–536. University Park, PA.

Lumley, J. L. 1969 Drag reduction by additives. *Annu. Rev. Fluid Mech.* **1** (1), 367–384.

Lumley, J. L. 1992 Some comments on turbulence. *Phys. Fluids A* **4**, 203–211.

L'vov, V. S., Pomyalov, A., Procaccia, I. & Tiberkevich, V. 2004 Drag reduction by polymers in wall bounded turbulence. *Phys. Rev. Lett.* **92** (24), 244503.

Manning, R. 1890 On the flow of water in open channels and pipes. *Instn of Civil Engineers of Ireland,* .

Marusic, I., McKeon, B., Monkewitz, P., Nagib, H., Smits, A. & Sreenivasan, K. 2010 Wall-bounded turbulent flows at high Reynolds numbers: recent advances and key issues. *Phys. Fluids* **22** (6), 065103.

Massey, B. S. & Ward-Smith, J. 1998 *Mechanics of fluids*, , vol. 1. Crc Press.

Mathur, M., Haller, G., Peacock, T., Ruppert-Felsot, J. E. & Swinney, H. L. 2007 Uncovering the Lagrangian skeleton of turbulence. *Phys. Rev. Lett.* **98** (14), 144502.

McKeon, B., Zagarola, M. & Smits, A. 2005 A new friction factor relationship for fully developed pipe flow. *J. Fluid Mech.* **538**, 429–443.

Mckeon, B. J., Li, J., Jiang, W., Morrison, J. F. & Smits, A. J. 2004 Further observations on the mean velocity distribution in fully developed pipe flow. *J. Fluid Mech.* **501**, 135–147.

Menter, F. R. 1994 Two-equation eddy-viscosity turbulence models for engineering applications. *AIAA J.* **32** (8), 1598–1605.

Moin, P. & Mahesh, K. 1998 Direct numerical simulation: a tool in turbulence research. *Annu. Rev. Fluid Mech.* **30** (1), 539–578.

Monin, A. S. & Obukhov, A. M. 1954 Basic laws of turbulent mixing in the atmospheric mixing layer. *Trudy Geofiz. Inst. Akad. Nauk SSSR* **151** (24), 163–187.

Mouret, G. 1921 Antoine Chézy: histoire d'une formule d'hydraulique. *Annales des Ponts et Chaussées 61, Paris* .

Nikuradse, J. 1950 *National advisory committee for aeronautics technical memorandum 1292*. Washington, D. C., Reprinted in English.

Obukhov, A. M. 1946 Turbulence in thermally inhomogeneous atmosphere. *Trudy Inst. Teor. Geofiz. Akad. Nauk SSSR* (1), 95–115.

Orlandi, P., Bernardini, M. & Pirozzoli, S. 2015 Poiseuille and Couette flows in the transitional and fully turbulent regime. *J. Fluid Mech.* **770**, 424–441.

Perlekar, P., Mitra, D. & Pandit, R. 2006 Manifestations of drag reduction by polymer additives in decaying, homogeneous, isotropic turbulence. *Phys. Rev. Lett.* **97** (26), 264501.

Pirozzoli, S., Bernardini, M. & Orlandi, P. 2014 Turbulence statistics in Couette flow at high Reynolds number. *J. Fluid Mech.* **758**, 327–343.

Pirozzoli, S., Bernardini, M., Verzicco, R. & Orlandi, P. 2017 Mixed convection in turbulent channels with unstable stratification. *J. Fluid Mech.* **821**, 482–516.

Pope, S. B. 2000 *Turbulent Flows*. Cambridge, England: Cambridge University Press.

Prakash, V. N., Mercado, J. M., van Wijngaarden, L., Mancilla, E., Tagawa, Y., Lohse, D. & Sun, C. 2016 Energy spectra in turbulent bubbly flows. *J. Fluid Mech.* **791**, 174–190.

Prandtl, L. 1953 *Essentials of Fluid Dynamics*, 3rd edn. London: Blackie & Son.

Procaccia, I., L'vov, V. S. & Benzi, R. 2008 Colloquium: Theory of drag reduction by polymers in wall-bounded turbulence. *Rev. Mod. Phys.* **80** (1), 225.

Reichardt, H. 1956 Über die geschwindigkeitsverteilung in einer geradlinigen turbulenten Couetteströmung. *Z. Angew. Math. Mech. Sonderheft* **36**, S26–29.

Reichardt, H. 1959 Gesetzmässigkeiten der geradlinigen turbulenten Couetteströmung. Mitt. Max-Planck-Inst. für Strömungsforschung, No. 22, Göttingen.

Rensen, J., Luther, S. & Lohse, D. 2005 The effect of bubbles on developed turbulence. *J. Fluid Mech.* **538**, 153–187.

Reynolds, O. 1883 On the experimental investigation of the circumstances which determine whether the motion of water in parallel channels shall be direct or sinuous and of the law of resistance in parallel channels. *Phil. Trans. R. Soc. London* **174**, 935–982.

RICHARDSON, L. F. 1922 *Weather Prediction by Numerical Process*. Cambridge, England: Cambridge University Press.

RICHTER, D. H. 2015 Turbulence modification by inertial particles and its influence on the spectral energy budget in planar Couette flow. *Phys. Fluids* **27** (6), 063304.

ROBERTSON, J. M. 1959 On turbulent plane-Couette flow. In *Proceedings of the Sixth Midwest Conference on Fluid Mechanics*, pp. 169–182. University of Texas, Austin.

ROBERTSON, J. M. & JOHNSON, H. F. 1970 Turbulence structure in plane Couette flow. *Proc. A.S.C.E., J. Eng. Mech.* **96**, 1171–1182.

ROBINSON, S. K. 1991 Coherent motions in the turbulent boundary layer. *Annu. Rev. Fluid Mech.* **23** (1), 601–639.

RODI, W. 1993 *Turbulence models and their application in hydraulics*. CRC Press.

SCHUMACHER, J., SCHEEL, J. D., KRASNOV, D., DONZIS, D. A., YAKHOT, V. & SREENIVASAN, K. R. 2014 Small-scale universality in fluid turbulence. *Proc. Natl. Acad. Sci. USA* **111** (30), 10961–10965.

SMITH, C. & WALKER, J. 1995 Turbulent wall-layer vortices. In *Fluid vortices*, pp. 235–289. Springer.

SMITS, A. J., MCKEON, B. J. & MARUSIC, I. 2011 High–Reynolds number wall turbulence. *Annu. Rev. Fluid Mech.* **43**.

SREENIVASAN, K. R. 1999 Fluid turbulence. *Rev. Mod. Phys.* **71** (2), S383.

STRICKLER, A. 1923 Beiträge zur frage der geschwindigkeitsformel und der rauhligkeitszahlen für ströme, kanäle und geschlossene leitungen. *Mitt. des Eidgenössischen Amtes für Wasserwirtschaft* **16**.

STULL, R. B. 1988 *An Introduction to Boundary Layer Meteorology*, , vol. 13. Springer Science & Business Media.

TELBANY, M. M. M. E. & REYNOLDS, A. J. 1982 The structure of turbulent plane Couette flow. *Trans. A.S.M.E., J. Fluids Eng.* **104**, 367–372.

TENNEKES, H. & LUMLEY, J. L. 1972 *A First Course in Turbulence*. Cambridge, MA and London: MIT Press.

TOMS, B. A. 1948 Some observations on the flow of linear polymer solutions through straight tubes at large Reynolds numbers. *Proc. 1st Int. Cong. Rheology, Amsterdam* **135**.

TOSCHI, F. & BODENSCHATZ, E. 2009 Lagrangian properties of particles in turbulence. *Annu. Rev. Fluid Mech.* **41** (375–404).

TRAN, T., CHAKRABORTY, P., GUTTENBERG, N., PRESCOTT, A., KELLAY, H., GOLDBURG, W., GOLDENFELD, N. & GIOIA, G. 2010 Macroscopic effects of the spectral structure in turbulent flows. *Nat Phys* **6**, 438–441.

Tsukahara, T., Kawamura, H. & Shigai, K. 2006 DNS of turbulent Couette flow with emphasis on the large-scale structure in the core region. *J. Turbul.* **7** (19).

Turner, J. S. 1973 *Buoyancy effects in fluids*. Cambridge University Press.

van der Veen, R. C., Huisman, S. G., Dung, O.-Y., Tang, H. L., Sun, C. & Lohse, D. 2016 Exploring the phase space of multiple states in highly turbulent Taylor-Couette flow. *Phys. Rev. Fluids* **1** (2).

Vincenti, W. G. 1982 Control-volume analysis: A difference in thinking between engineering and physics. *Technol. Cult.* **23** (2), 145–174.

Virk, P. S., Merrill, E., Mickley, H., Smith, K. & Mollo-Christensen, E. 1967 The Toms phenomenon: turbulent pipe flow of dilute polymer solutions. *J. Fluid Mech.* **30** (2), 305–328.

Wallace, J. M. & Hobbs, P. V. 2006 *Atmospheric science: an introductory survey*. Academic press.

White, C. M. & Mungal, M. G. 2008 Mechanics and prediction of turbulent drag reduction with polymer additives. *Annu. Rev. Fluid Mech.* **40**, 235–256.

Wu, X. & Moin, P. 2008 A direct numerical simulation study on the mean velocity characteristics in turbulent pipe flow. *J. Fluid Mech.* **608**, 81–112.

Wunsch, C. & Ferrari, R. 2004 Vertical mixing, energy, and the general circulation of the oceans. *Annu. Rev. Fluid Mech.* **36**, 281–314.

Yang, S.-Q. 2009 Drag reduction in turbulent flow with polymer additives. *J. Fluids Eng.* **131** (5), 051301.

Zagarola, M. V. & Smits, A. J. 1998 Mean-flow scaling of turbulent pipe flow. *J. Fluid Mech.* **373**, 33–79.

Zhou, Q., Taylor, J. R. & Caulfield, C. P. 2017 Self-similar mixing in stratified plane Couette flow for varying Prandtl number. *J. Fluid Mech.* **820**, 86–120.

Zuniga Zamalloa, C. 2012 Experiments on turbulent flows in rough pipes: spectral scaling laws and the spectral link. PhD thesis, University of Illinois at Urbana-Champaign.

Zuniga Zamalloa, C., Ng, H. C., Chakraborty, P. & Gioia, G. 2014 Spectral analogues of the law of the wall, the defect law and the log law. *J. Fluid Mech.* **757**, 498–513.